POLITECNICO
MILANO 1863

SCUOLA DI INGEGNERIA INDUSTRIALE
E DELL'INFORMAZIONE

Modeling and simulation of ultrasonic backscattering effects as intrabody communication application based on PMUT arrays

TESI DI LAUREA MAGISTRALE IN
MATERIALS ENGINEERING AND NANOTECHNOLOGY -
INGEGNERIA DEI MATERIALI E DELLE NANOTECNOLOGIE

Author: **Kubilay Kaan Bahceci**

Student ID: 10557553
Advisor: Prof. Alberto Corigliano
Co-advisors: Gianluca Massimino, Omer Osman Mohammed Abdalla
Academic Year: 2021-2022

Abstract

Recent developments in biomedical engineering have brought forward an urgent need for effective wireless communication and power delivery technologies. Collectively known as Intrabody Communication (IBC), these technologies utilize various methods to deliver data such as electromagnetic waves, photons, and ultrasound. This study proposes a unidirectional communication system that exploits the scattering properties of ultrasound waves; in order to transfer data from the implanted medical device (IMD) to an external transducer array. The external acoustic wave transmission and reception are done through Microelectromechanical Systems (MEMS) ultrasonic transducers, which are employed as an array of Piezoelectric Micromachined Ultrasonic Transducers (PMUTs). While the IMD is selected to be the neural dust that records peripheral nerve activity, this method of data transfer applies to various implants that adopt ultrasonic IBC. In the peripheral nervous system, the neural messages are transferred through an electrochemical polarization called the action potential. These neural action potential voltages are then approximated and imposed on the simulated neural dust piezoelectric material. This communication scheme aims to transfer this implant voltage data to the external probe as accurately as possible. The proposed model tries to achieve this flow of information by sending an excitation signal to induce an acoustic echo and estimate the input action potential voltages using the ultrasonic backscattering wave collected by the external PMUT array. The total time traveled by the backscattering echo is called the time of flight (TOF). Using the frequency and phase content of the acoustic echo, various TOF values are collected throughout the full span of the neural dust input voltage. Distinct data points collected using this method can then be interpolated to estimate the behavior of the neuron.

Keywords: Acoustic Backscattering, Time of Flight (TOF), Implantable Medical Devices (IMD), Intrabody Communication (IBC), Piezoelectric Micromachined Ultrasonic Transducers (PMUTs), Neural Dust, Ultrasound

Abstract in lingua italiana

I recenti sviluppi dell'ingegneria biomedica hanno creato l'urgente necessità di comunicazioni wireless efficaci e tecnologie per l'erogazione dell'energia. Conosciute come Intrabody Communication (IBC), queste tecnologie utilizzano vari metodi per fornire dati come onde elettromagnetiche, fotoni e ultrasuoni. Questo studio propone un sistema di comunicazione unidirezionale che sfrutta le proprietà di scattering delle onde ultrasoniche; per trasferire i dati tra il dispositivo medico impiantato (IMD) e un array di trasduttori esterni. La trasmissione e la ricezione delle onde acustiche esterne avviene tramite trasduttori ultrasonici MEMS (Microelectromechanical Systems), che sono impiegati come una serie di trasduttori piezoelettrici microfabbricati a ultrasuoni (PMUT). Sebbene l'IMD sia selezionato per essere la polvere neurale, questo metodo di trasferimento dei dati si applica a vari impianti che adottano l'IBC ad ultrasuoni. Nel sistema nervoso periferico, i messaggi neurali vengono trasferiti attraverso una polarizzazione elettrochimica chiamata potenziale d'azione. Queste tensioni del potenziale d'azione neurale vengono quindi approssimate e imposte al materiale piezoelettrico della polvere neurale. Questo schema di comunicazione mira a trasferire questi dati sulla tensione dell'impianto alla sonda esterna nel modo più accurato possibile. Il modello proposto cerca di ottenere questo flusso di informazioni inviando un segnale di eccitazione per incorrere nell'eco acustico e stimare le tensioni del potenziale d'azione in ingresso utilizzando l'onda di retrodiffusione ultrasonica raccolta dall'array PMUT esterno. Il tempo totale percorso dall'eco di retrodiffusione è chiamato tempo di volo (TOF). Utilizzando la frequenza e il contenuto di fase dell'eco acustico, vengono raccolti vari valori TOF per l'intero intervallo della tensione di ingresso della polvere neurale. Punti dati distinti raccolti utilizzando questo metodo possono quindi essere interpolati per stimare il comportamento del neurone.

Parole chiave: Ultrasuoni, Diffusione Acustica, Tempo di Volo (TOF), Dispositivi Medici Impiantabili, Comunicazione Intracorporea, Micro Trasduttori Piezoelettrici ad Ultrasuoni (PMUT), Impianto Neurale

Contents

Introduction

The current landscape of medicine and neuroscience increasingly relies on electronic implants to increase the quality of life for patients. These devices, sometimes called Implantable Medical Devices (IMDs), can be used for continuous monitoring of vital signs (e.g. glucose levels, oxidation levels, heart rhythm, etc.), and/or altering the body in a certain way (e.g. drug pumps, cardiac pacemakers, etc.). There has been a steady increase in interest in IMDs and related Biomedical Engineering topics, to create new therapeutic, diagnostic, and assistive devices. *Brain-Machine Interfaces (BMI)* are a part of this continuing interest in IMD applications. BMI refers to a set of neurotechnologies that attempt to decipher and manipulate brain activity. The latest in-human studies show that devices that provide a direct link between the body and a computer are close to becoming a reality [47]. BMI technologies rely on miniature *neural dust* devices, which have the goal of making Brain-Machine Interface reliable, safe, and low-cost enough to be widely adopted. Neural dust is a *Microelectromechanical System (MEMS)* device attached to a nerve, intending to record a particular neurological activity. Since the neural dust needs to be directly submerged into the body, the invasive nature of the technology demands an implant as minute as possible. This creates an essential size constraint for the whole neural dust module. Recent advances made in MEMS and micromachining techniques provide a gateway for realizing smaller and smaller mechanical structures [57], but miniaturization is not the sole challenge that needs to be resolved. Currently, two main requirements for further development of neural dust technology are:

- *Power requirements and wireless power delivery:* Batteries are the least scalable part of any MEMS device and bring various problems to each system. Battery usage on IMDs, if improperly designed, can be harmful to the patient. When the battery is drained, a new medical procedure is needed to replace it. They can also be miniaturized up to a point, severely constraining the minimum size. All of these reasons are the basis for the demand for a wireless power delivery technology for neural dust applications [48, 54].
- *Wireless Communication:* Implants are naturally submerged in the body, and wired communication is a highly invasive and unhealthy method to be utilized in IMDs.

> This is the reason for the existence of different wireless communication methods, collectively called *intrabody communication (IBC)*. The current state of IBC provides various data transfer technologies, which employ electromagnetic waves, ultrasound, and even photons as the information carriers [24]. An in-depth analysis of the advantages and drawbacks of these different transfer methods is provided in section 2.2.1.

In this thesis, ultrasound is proposed to assist with the wireless communication and power delivery requirements of the neural dust.

0.1. Thesis Objectives

The main objective of this thesis is to provide unidirectional communication from an implant to an external device. The communication method is selected to employ ultrasonic waves provided by an array of MEMS-based transducers, more specifically called Piezoelectric Micromachined Ultrasonic Transducers (PMUTs). The IMD is chosen to be a neural dust mote, which is tasked with recording the activity of a peripheral nerve. Neural dust is expected to be directly connected to a nerve, and the collected neural recordings need wireless technology to transfer this recorded data to an outer collector. This work focuses on using ultrasound to achieve this communication, utilizing the acoustic interaction that occurs between the neural dust and the investigative sound wave. This interaction, called acoustic backscattering, imposes an echo on the external probe, which carries the current status of the implanted device. The wave properties of the aforementioned echo are anticipated to vary with respect to the neural recording input, which conceives a possibility to recreate the neural recording using the scattered ultrasonic wave. This neurological data can then be used and manipulated for diagnostic and therapeutic purposes.

0.2. Organization of the Work

Chapter 1 is an introduction to both *MEMS* and *PMUT*, also containing *micromachining techniques* that can be used for manufacturing both the proposed PMUT array and the neural dust devices. It also discusses the theoretical basis for piezoelectric materials and related *electromechanical coupling* used to generate ultrasound waves in PMUT.

Chapter 2 presents general concepts of *IMDs*, and their data transfer techniques, generally called *Intrabody Communication (IBC)*. The advantages and drawbacks of ultrasound usage in implants are discussed. It also provides an introduction and state-of-the-art for the *Neural Dust* devices. Finally, a brief explanation is given for the electrochemical process that occurs inside an active neuron and the approximate voltage profile used as an input for the neural dust implant.

Chapter 3 contains the mathematical background for the acoustic propagation inside a tissue phantom and the acoustic backscattering phenomenon that occurs when the sound wave interacts with a solid body.

Chapter 4 discusses the parameters that fully define the proposed neural dust implant, the PMUT array, and the complete simulation model.

Chapter 5 is dedicated to the methods used to process the backscattered acoustic echo and provides the final data point and interpolated results.

Chapter 6 concludes the study with a discussion on the obtained results and proposes the future activities that may be needed to improve what is done in this thesis.

1 | Piezoelectric Micromachined Ultrasonic Transducers (PMUTs)

In this chapter, a general introduction to Microelectromechanical Systems (MEMS) and Piezoelectric Micromachined Ultrasonic Transducers (PMUT) is proposed. Possible applications and machining techniques for these devices are summarized. Since one of the main operating principles of PMUT is related to the piezoelectric effect, the mathematical basis of active piezo materials is also covered here.

1.1. Overview of MEMS and PMUT

Microelectromechanical systems (MEMS) are a family of miniature devices that contain mechanical or electro-mechanical structures. Device component sizes for MEMS are generally in micro-scale, which is around 0.1-100 μm, while the packaged device can have dimensions well beyond 1 mm. As a collection of products, MEMS usually refer to a set of processes used to design and manufacture scaled-down structures. Available MEMS devices include various types of microsensors, microactuators, microelectronics, and general mechanical microstructures. The history of MEMS can be traced back to the 1960s when a series of research work was done by Honeywell Research Center and Bell Labs that described the possibility of the first silicon diaphragm pressure sensors and strain gauges. These primitive MEMS devices were then commercialized in the early 1970s thanks to advancements in available silicon manufacturing techniques [8]. These fabrication processes, now collectively called *micromachining*, are an integral part of any MEMS development. Continuous progress made in the field of micromachining unlocks new MEMS application possibilities alongside cheaper, more reliable, and efficient commercial devices. Today, many modern systems are available due to steady research in the fields of MEMS and micromachining, which include PMUT and neural dust employed during this research.

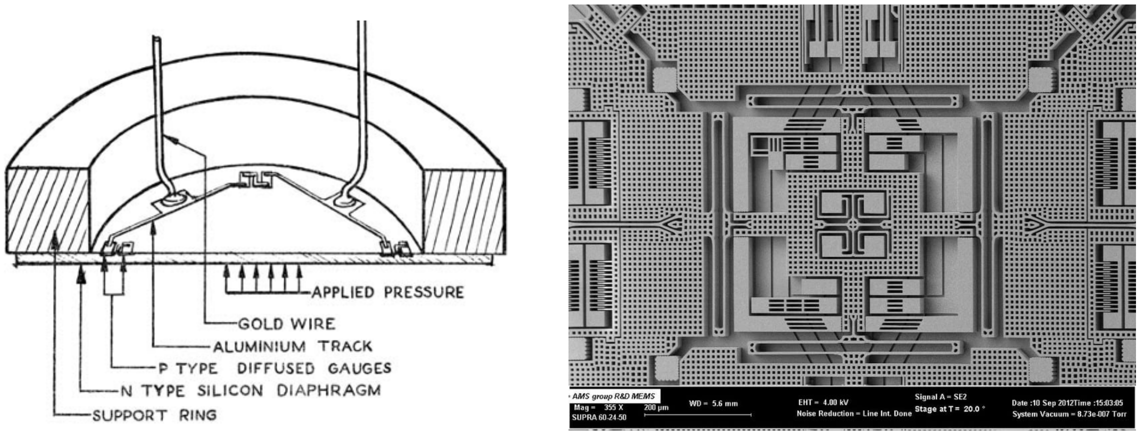

(a)

(b)

Figure 1.1: (a) Schematics for an early microdevice, a pressure sensor. [8] (b) A modern MEMS sensor by STMicroelectronics. [17]

In the last decade, the utilization of ultrasounds in industrial and medical applications has expanded and become common for areas including nondestructive testing (NDT), medical imaging, particle manipulation, communication, and power delivery. The need for an accurate way to generate and collect ultrasonic waves sparked a thriving industry around it. Generally, MEMS-based ultrasonic transducers are a set of miniature technologies that are tasked with aiding this industry field, providing cheap and efficient ultrasound for various types of applications. These transducers can incorporate magnetostriction or a photoacoustic effect, but by far the most common method is the piezoelectric effect. Traditional piezoelectric transducers were first deployed as a SONAR military application in France during WW1 [37]. These conventional devices use different shapes (e.g., cubic and disc type) and bulk piezoelectric ceramics to exploit thickness-mode vibrations occurring on a plate with a fixed boundary. Technological developments have brought a new type of MEMS that employs a thin piezoelectric layer as the cavity membrane to generate ultrasound. These few μm thick microdevices, called *Piezoelectric Micro-machined Ultrasonic Transducers (PMUT)* include a variety of advantages over the conventional methods: more flexible geometries with increased frequency bandwidth that can be stacked side by side to dramatically increase the ultrasound output. This ability to linearly scale the ultrasound magnitude is the basis of the current 3D imaging technologies, where disparate lines of MUT devices scan at different angles. Another advantage of PMUT is a more streamlined manufacturing process that provides higher volume fabrication at a lower cost, which makes PMUT applications more accessible to consumers than ever. This study uses a conventional disc-type bulk piezoelectric transducer for neural dust implant while deploying an array of PMUTs to generate and receive sound for an external computer.

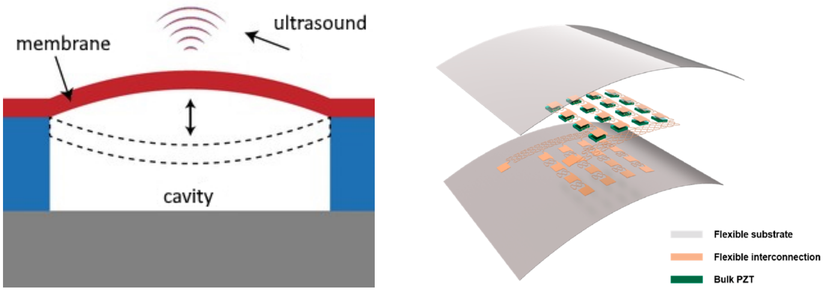

(a) (b)

Figure 1.2: (a) Diagram of a basic PMUT design and needed components. [45] (b) An array of cube-type bulk piezoelectric ultrasonic transducers for a flexible wearable device. [32]

1.1.1. Excitation and Reception Modes of PMUT

A thin layer of piezoelectric material, most commonly Lead Zirconate Titanate (PZT), is deposited on a Si/SiO_2 membrane and sandwiched between two electrodes, creating a multi-layered configuration. The membrane is connected around its periphery to a cavity. This cavity is generally filled with air at atmospheric pressure ($P = 1\ atm$). Due to the significant acoustic impedance mismatch between the membrane and the air, it acts as an acoustic insulator. For geometry and material properties, this study uses a custom PMUT design made by *STMicroelectronics*. A schematic example is given in figure 1.3 to approximate the final structure:

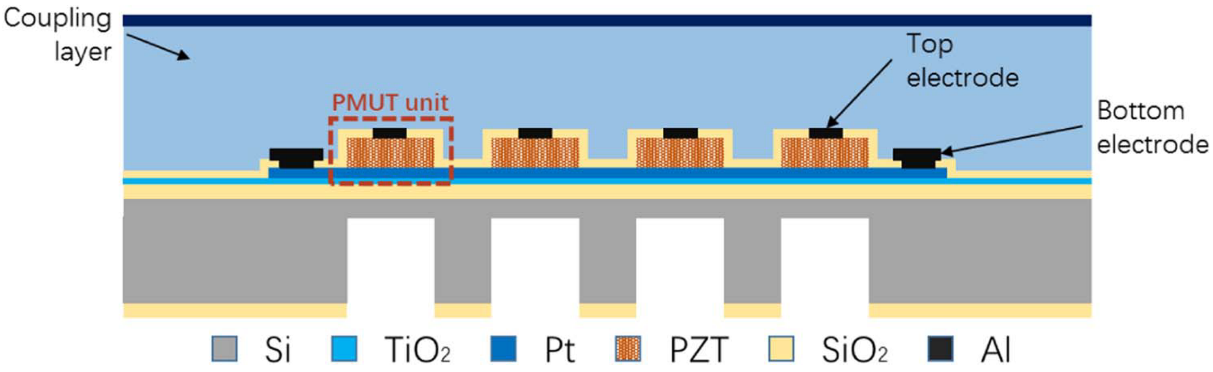

Figure 1.3: Schematics containing all PMUT layers for a custom four element PMUT array design. [12]

In the following work, the coupling layer is called a *matching layer*. The indicated PMUT structure uses electromechanical coupling supplied by the piezoelectric material to induce acoustic pressure. During this excitation/transmission mode, the electric field instigated between the top and bottom boundaries of the PZT creates lateral mechanical strain in the whole membrane. As a result, vibrational bending of the membrane appears. The interaction between the acoustic propagation medium and the PMUT structure ensures local acoustic pressure variance, and the ultrasound is thus generated.

The inverse piezoelectric effect can also be utilized to receive and record the sound waves in a medium. During the reception mode of PMUT, incoming sound waves impose a mechanical deformation on the membrane. The applied stress on piezoelectric material polarizes and develops an electric field. The voltage and current caused by this electric field can then be collected and stored.

Proper depth penetration is only possible if the membrane vibrates at its maximum magnitude. Operating the PMUT at an eigenfrequency is essential to achieve the best viable efficiency. This resonant frequency value is not only related to material parameters, but also to the geometry and residual stresses that may arise during fabrication. A proper characterization procedure is then needed. For the sake of simplicity, this thesis assumes the manufacturing defects as zero and computes a frequency sweep study to find the resonant frequency of the PMUT submerged in tissue.

1.2. Piezolectric Effect

The piezoelectric effect refers to the coupling phenomenon between electric and mechanical responses in some crystal structures. In dielectric solids experiencing an external electric field, the material adapts and changes its nuclei and electron configurations dynamically. This results in a dipole formation in the solid body, and the material is polarized. Piezoelectric materials set themselves apart from other dielectric materials by not only being able to polarize under an electric field $\boldsymbol{E}$ but also under mechanical stress T. The outcome of this event in the real world helps us create devices that respond to mechanical input (bending, compression, etc.) with electrical output (generation of current). This is also known as the *direct piezoelectric effect* and is usually taken advantage of as a sensor. The proposed study also exploits the mechanical deformation that occurs under a specific electric polarization, which is called the *inverse piezoelectric effect*, shown in figure 1.4b. Piezoelectricity was first discovered by Pierre and Jacques Curie. They observed that some materials, like topaz and quartz, produce electric surface charges under mechanical stresses. Piezoelectric materials have rapidly grown into a new field in the material sciences during the last quarter of the nineteenth century [11]. From then on, a plethora of new applications became possible due to the integration of piezoelectric materials, where its usage is especially beneficial for systems with sensor and/or actuator tasks. Today, common piezoelectric MEMS devices include piezoelectric motors, medical sensors, actuators, microphones, micro-robotics applications, and energy harvesters among others. It is also commonly used for micro transducer applications like this study, due to its scalability to various sizes and shapes. Piezoelectric materials are also highly preferable due to their linear response to a given input. The most common piezoelectric materials used in MEMS devices include Lead Zirconate Titanate (PZT), Aluminium Nitride (AlN), and Zinc Oxide (ZnO).

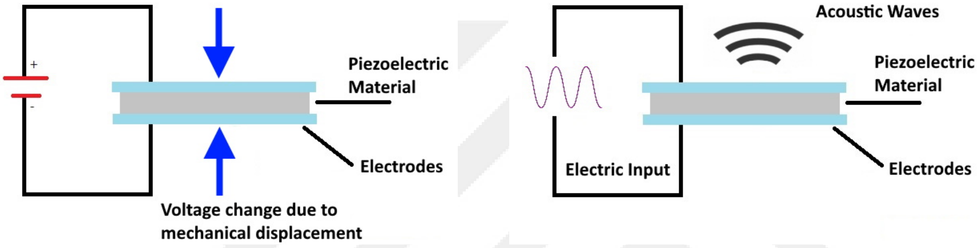

(a) (b)

Figure 1.4: (a) Direct piezoelectric effect. (b) Inverse piezoelectric effect. [1]

In this work, the inverse piezoelectric effect is used on both the neural dust and the external PMUT array where acoustic excitation is needed. Direct effect, on the other hand, is used only for receiving signals in the PMUT array. The complex associations between the elastic and electric phenomena due to piezoelectric coupling are mapped in figure 1.5:

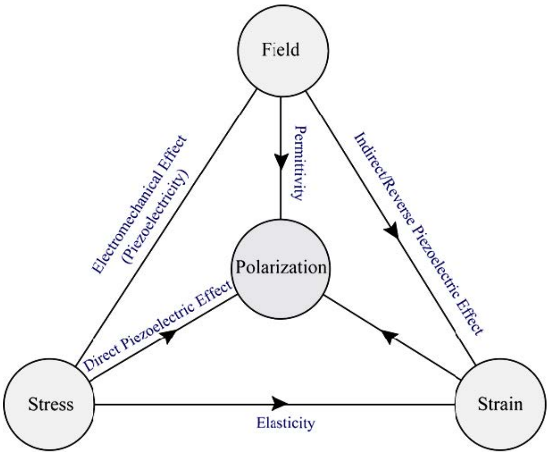

Figure 1.5: A map of relations between the mechanical and electrical properties. [18]

In the next section, the basics of polarization and its association with the electric field are explored. Then, the constitutive relations between the electric field and strain (strain-charge form) and between stress and electric field (stress-charge form) will be explained in section 1.2.2.

1.2.1. Polarization of Dielectric Materials

Dielectric materials are electrically insulating (non-metallic) solid bodies that exhibit electric dipole structure, where on a molecular or atomic level, positively and negatively charged entities exist. This effectively separates positive and negative charges to different ends of the material as shown below:

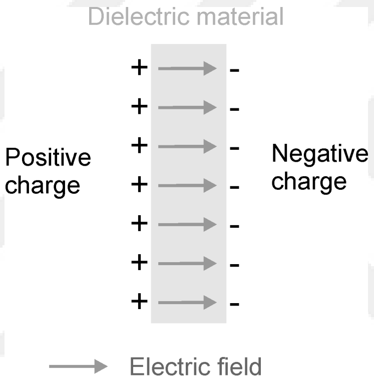

Figure 1.6: Polarization structure of a dielectric material. [4]

Spontaneous polarization occurs when the dielectric structure is polarized without any applied fields. Perovskite structures, such as PZT, are more prone to this type of polarization [4]. Piezoelectric polarization, on the contrary, only develops when mechanical stresses $\boldsymbol{\sigma}$ are applied. These two polarization types contribute to the electric displacement vector $\boldsymbol{D}$ through the equation:

$$\boldsymbol{D} = \varepsilon \boldsymbol{E} + \boldsymbol{P} \tag{1.1}$$

where $\boldsymbol{P}$ is the permanent polarization, ε is the dielectric permittivity, and $\boldsymbol{E}$ is the applied electric field [18]. This equation satisfies Gauss's Law in a dielectric body, where ρ_f signifies free charges per unit volume:

$$\nabla \cdot \boldsymbol{D} = \rho_f. \tag{1.2}$$

The general structure of the piezoelectric material used in the model, Lead Zirconate Titanate (PZT) is as shown in figure 1.7.

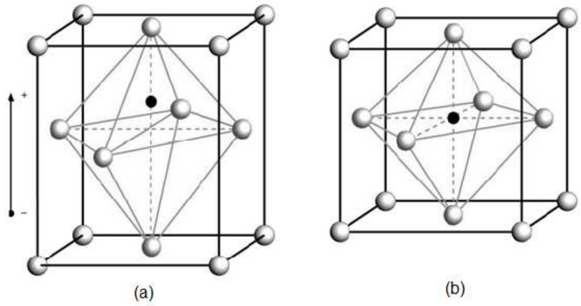

Figure 1.7: (a) PZT under mechanical stress. (b) Undeformed PZT structure. [3]

The structure consists of Pb^{+2},O^{-2} and either Ti^{+4} or Zr^{+4} as the ion in the middle. When PZT is under stress, Ti^{+4}, Zr^{+4} ions relocate as a response and create a change in the dipole moment. This dipole structure, in turn, results in polarization and electrical output. Materials with a perovskite crystal structure are thus very effective for electromechanical coupling, but also prone to spontaneous polarization. Material defects are always present in real-world structures, and point defects (absent or misplaced ions in the crystal structure) can easily create local dipole moments and polarization. This would severely affect the efficiency of the piezoelectric coupling, where already polarized zones cannot react to mechanical input. For this reason, characterization studies are always preferred in advance.

The orientation of polarization is also an important factor for proper piezoelectric material usage. The coupling mechanism between mechanical and electrical domains is inherently anisotropic and dipoles are randomly oriented. To combat unreliable and inefficient piezoelectric output, a complex process called *poling* is utilized after manufacturing. During poling, the material is subjected to a very high-frequency alternating current (AC) that orients all dipoles in a singular direction [19]. After the process, most dipoles stay in the same direction, ensuring better piezoelectric coupling.

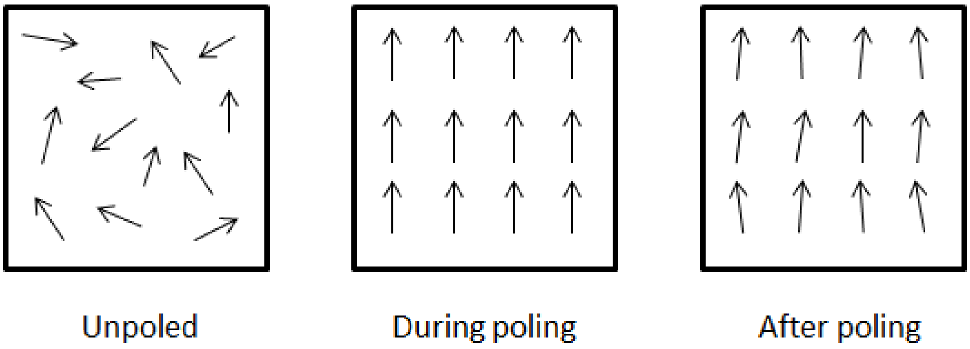

Figure 1.8: Poling process applied to manufactured piezoelectric materials. [19]

The directionality of piezoelectric materials is an important aspect of designing proper MEMS devices. Different material coupling parameters are required for distinct *piezoelectric coupling modes*. Proper material selection for the practiced mode is essential for effective output generation. The most common coupling modes are visualized in figure 1.9.

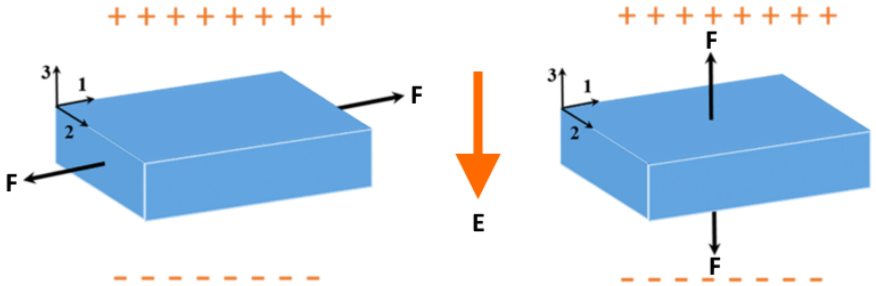

Figure 1.9: Piezoelectric coupling modes d_{31} on the left, and d_{33} on the right. The polarization direction is assumed to be in the z-direction. [30]

In this thesis, both the proposed model and PZT material parameters are assumed and configured to be in d_{33} mode.

1.2.2. Constitutive Relations

Piezoelectricity is defined through two equivalent sets of constitutive equations. *Stress-charge form* relates mechanical stress and electric displacement tensor, and can be expressed in index notation as [56]:

$$\begin{cases} D_i = e_{ij}S_j + \varepsilon^S_{ij}E_j & (1.3a) \\ T_i = c^E_{ij}S_j - e_{ij}E_j & (1.3b) \end{cases}$$

where D_i is the electric displacement, T_i is the mechanical stress, S_i is the mechanical strain and E_i is the electric field. Material parameters used are denoted as follows: c^E_{ij} for the elastic stiffness or elasticity matrix under constant E_i, ε^S_{ij} is the permittivity under constant strain, and e_{ij} refers to the piezoelectric coupling matrix for stress-charge form constitutive equations.

Strain-charge form describes the relationship between the mechanical strain and electrical displacement and can be formulated as:

$$\begin{cases} D_i = d_{ij}T_j + \varepsilon^T_{ij}E_j & (1.4a) \\ S_i = s^E_{ij}T_j + d_{ij}E_j & (1.4b) \end{cases}$$

where s_{ij} connotes the elastic compliance and d_{ij} is the analogous piezoelectric coupling tensor for strain charge form. Please remind that the values of permittivity ε_{ij} also varies under constant mechanical strain or stress values (which implies different forms). Most material sheets provide parameters for this constitutive equation form. These parameters can easily be transformed using the equations supplied in equation (1.5). [26]

$$\begin{cases} c^E_{ij} = (s^E_{ij})^{-1} & (1.5a) \\ e_{ij} = d_{ij} \cdot (s^E_{ij})^{-1} & (1.5b) \\ \varepsilon^S_{ij} = \varepsilon^T_{ij} - d_{ij}(s^E_{ij})^{-1}(d_{ij})^T & (1.5c) \end{cases}$$

where $(d_{ij})^T$ is the transpose of the tensor d_{ij}. This conversion is achieved using the dielectric formula demonstrated in equation (1.1), alongside Hooke's Law for mechanical deformation:

$$\boldsymbol{T} = \boldsymbol{c} : \boldsymbol{S} \tag{1.6}$$

During this research, the stress-charge form was solely used for both the material parameters and the configuration of the proposed model.

1.3. Device Manufacturing Techniques

Manufacturing of PMUT devices is, in general, directly correlated with the surface micromachining method utilizing *sacrificial layers*. The generic process usually has these steps:

- *Substrate Preparation and Doping:* A thin plate of Si, called the wafer, is used as a base. The substrate is doped, and an oxide layer is formed on top of the wafer. This oxide layer has a thickness that is controlled by the doping process penetration depth, and therefore the oxidation rate and total oxidation duration are of utmost importance. Formed SiO_2 acts as an insulator between the wafer and the structure.
- *Material Layer Deposition:* Structural layer is then deposited using various physical or chemical deposition techniques (PVD, CVD). The PMUT layer configuration has distinct material types for each layer (as it is a polymer structure with metal electrodes) and may need different deposition processes to form each layer effectively.

Undesirable material accumulation on the surface, alongside rough surface, may cause improper deposition.

- *Sacrificial Layer Deposition:* A sacrificial layer is an oxide layer added to be removed later on in the manufacturing process. It is used mostly for creating connections between layers (i.e. VIAs in electronic modules). Another important application category is freestanding mechanical structures (cantilever beams, and comb structures in accelerometers, among others). Precaution is needed when machining these layers, as stiction may cause low-quality fabrication output.

- *Patterning and Photolithography:* When the deposition of either the material or the sacrificial layer exists without patterning, the layer has a uniform thickness within tolerances. Patterning and photolithography enable more complex structures. A uniform layer of photoresist material is deposited to start this process. This photoresist is a light-sensitive material that acts as another sacrificial layer. A mask that contains the intended layer pattern is then created. A UV source is used with a mask to transfer the 2D pattern onto the surface. Then, the structure/sacrificial layer is deposited to conform to this pattern. In the end, the remaining photoresist can easily be subtracted, leaving only the necessary structure.

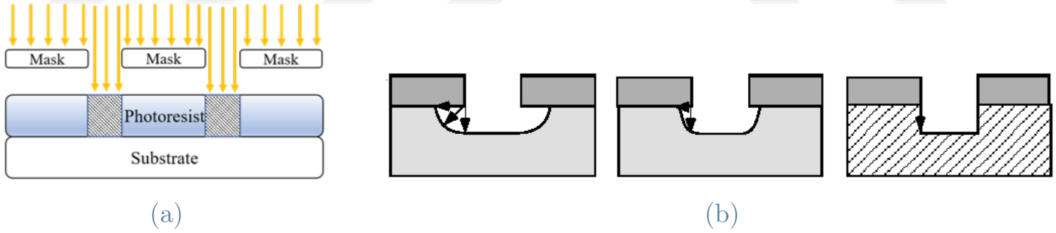

(a) (b)

Figure 1.10: (a) The photolithography step with a mask to imprint the desired pattern onto the surface. (b) Different etch processes and parameters can create various structure layers. [20]

- *Etching:* Etching is the process of removing layers or patterns on a wafer substrate. Etching, like a deposition, can either be chemical and/or physical. The etching rate and the etching technique used are essential parameters for reducing artifacts on the etched surface. Long-duration of chemical etching processes can unexpectedly result in the undercutting of structural layers. A mixture of physical and chemical etching is commonly used for perfect directionality (figure on the right in 1.10b).

2 | Intrabody Communication (IBC)

In this chapter, the basic theories for Implanted Medical Devices (IMDs), Intrabody Communication (IBC), and Neural Dust are explored. Since these concepts are directly related to this study, the state-of-the-art for these technologies is also included. For IBC, the pros and cons of using Ultrasound as a communication and/or power delivery method are scrutinized. Finally, polarization changes occurring inside a neuron during the action phase are briefly explained.

2.1. Implantable Medical Devices (IMDs)

Implantable Medical Devices (IMDs) refer to the family of biomedical devices embedded into the body or onto a patient's skin to support organs or whole systems of the body. These devices can sense vital signs, alter a specific bodily function, or assist the patient with their basic faculties (e.g., hearing and seeing). IMDs need to be attached to the body through a medical procedure, with the intent to remain there. Developing these types of devices often requires an efficient, effective, and safe approach. The first modern implant, a pacemaker, became available in 1958. Since then, the IMD device market has blossomed to a size of \$95.1 billion worldwide. With the ever-aging world population and the new devices enabled by current research and development towards IMDs, the market is expected to reach \$145.6 billion in 2030 [46]. The current landscape, as mentioned earlier, shows efforts focused on creating safe, inexpensive, and effective implants.

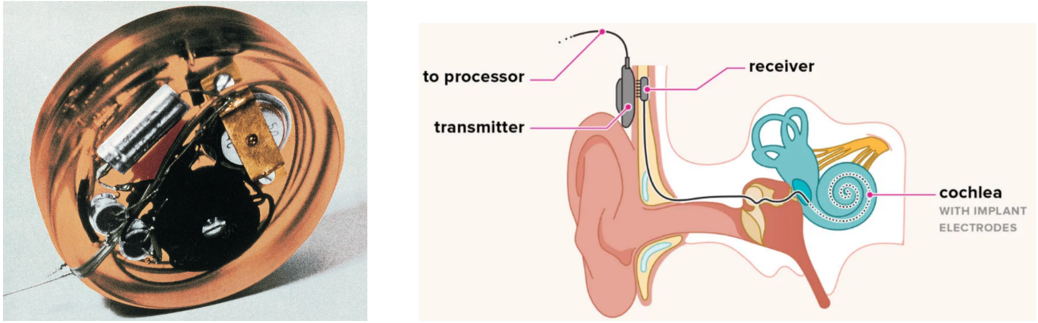

(a) First pacemaker (b) Cochlear implant

Figure 2.1: (a) First fully implantable pacemaker design, in 1958. By Siemens-Elema. [53] (b) A visual diagram of a modern cochlear implant. [40]

The varied nature of each IMD results in a different set of constraints and requirements. There are, however, some fundamental considerations that must be considered for all implants. These are, briefly, [29]

- *Bio-compatibility* Introducing foreign bodies into the system creates a natural response by the body. The abiotic materials in implants can create an adverse effect on the anatomy. Hence, all of the materials must be chosen to be safe for a long duration and to trigger a minimal immune response. Therefore, only bio-compatible piezoelectric materials are considered for this thesis and the following models.

- *Packaging and Hermeticity* Since IMDs often require electrical components, proper packaging is critical. Improper packaging of implants could cause free-flowing electricity in the body, while the implant would begin to corrode in contact with bodily fluids.

- *Structural Design Constraints* The human anatomy is a complex system with fundamentally distinct organs, tissues, and cell structures. Simulating this complex system is needed to ensure the IMD's mechanical and electrical components will work reliably. Thus, the components of the implanted device should uphold various external conditions, such as pressure, temperature, and electric/acoustic interference. Thereby the proper mechanical reinforcements and electrical shielding should be done to have a functional design. This study uses a tissue-like medium to apply these design constraints.

- A few extra points of discussion (Wireless Communication and Power Management) for implants will be analyzed in depth during Section 2.2.

2.1.1. Available Products

The most common implant types currently in use aid patients with cardiac, orthopedic, auditory, and dental problems. The most commonly used implantable medical devices are artificial joints, breast implants, cochlear implants, intraocular lenses, cardiac pacemakers, other cardiac implants, and intrauterine contraceptives. Orthopedic and dental implants are usually passive devices (only mechanical), while others (e.g., pacemakers and cochlear implants shown in figure 2.1b) are active, requiring electromechanical components. All active implants demand power input, and the most common solution today is to include batteries. This further increases the intrusiveness of implant devices and requires consecutive surgeries when the battery is consumed. A more detailed exploration of this problem and possible solutions will be given in the next section.

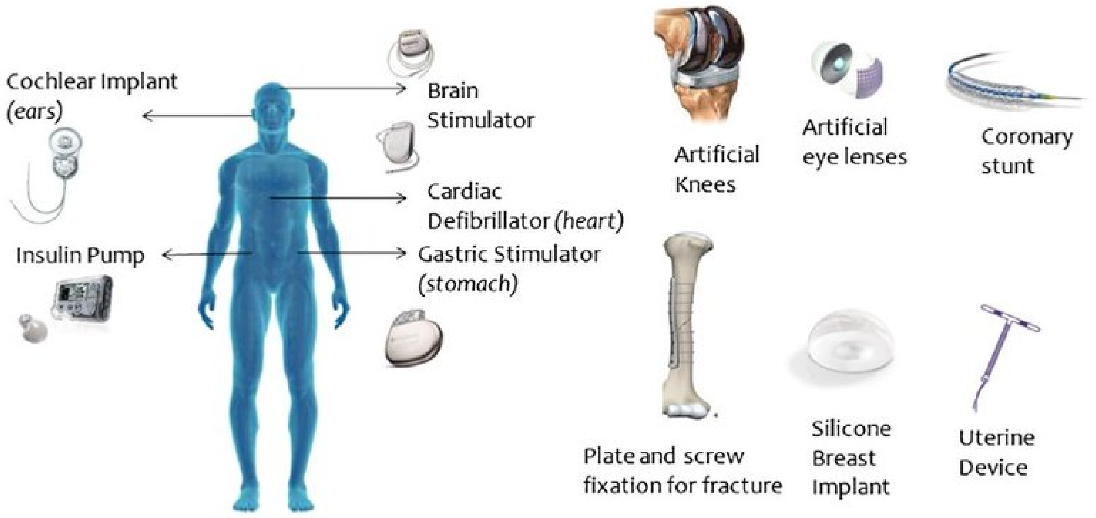

Figure 2.2: Visualisation of some of the IMDs mentioned above. [39]

2.2. Introduction to Intrabody Communication

Intrabody communication (IBC) is a set of promising wireless communication technologies to transfer data from the human body to medical and sports devices used daily. This definition would mean a communication link between either two implanted devices or an implant and an external device. IBC is crucial for any type of IMD that is tasked with sensing or any type of actuation that requires manual input. Due to this dependency, any emerging data transfer technology can theoretically be our gateway to a copious amount of exciting new implant possibilities. A summary of different communication technologies used in the latest academic papers is shown on figure 2.3:

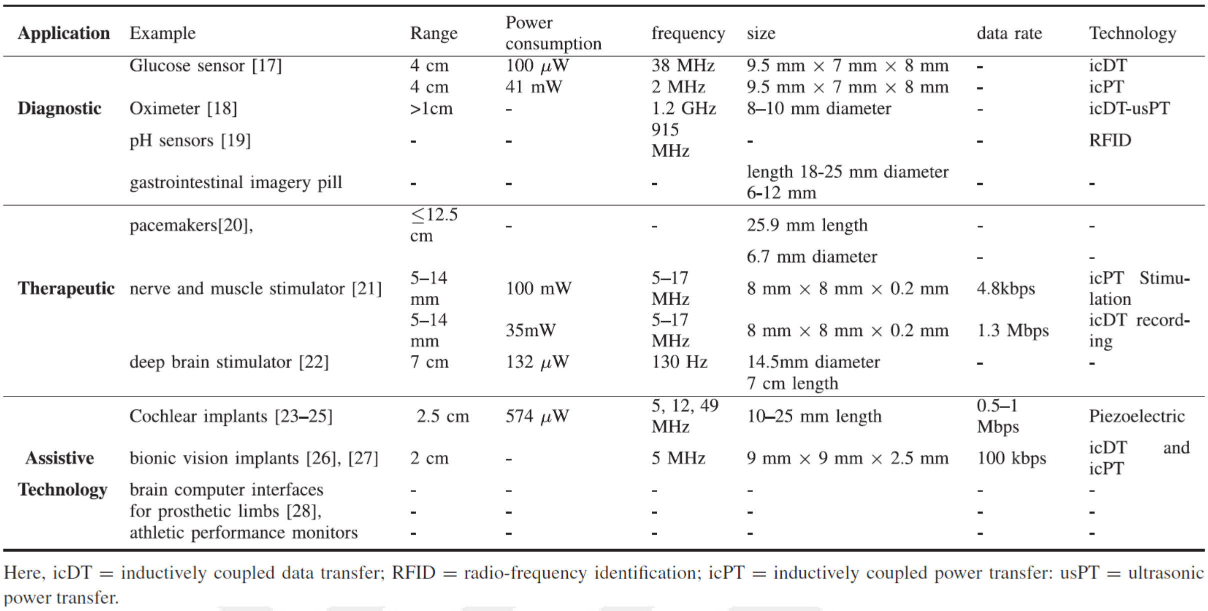

Application	Example	Range	Power consumption	frequency	size	data rate	Technology
Diagnostic	Glucose sensor [17]	4 cm	100 μW	38 MHz	9.5 mm × 7 mm × 8 mm	-	icDT
		4 cm	41 mW	2 MHz	9.5 mm × 7 mm × 8 mm	-	icPT
	Oximeter [18]	>1cm	-	1.2 GHz	8–10 mm diameter	-	icDT-usPT
	pH sensors [19]	-	-	915 MHz	-	-	RFID
	gastrointestinal imagery pill	-	-	-	length 18-25 mm diameter 6-12 mm	-	-
Therapeutic	pacemakers[20],	≤12.5 cm	-	-	25.9 mm length	-	-
					6.7 mm diameter	-	-
	nerve and muscle stimulator [21]	5–14 mm	100 mW	5–17 MHz	8 mm × 8 mm × 0.2 mm	4.8kbps	icPT Stimulation
		5–14 mm	35mW	5–17 MHz	8 mm × 8 mm × 0.2 mm	1.3 Mbps	icDT recording
	deep brain stimulator [22]	7 cm	132 μW	130 Hz	14.5mm diameter 7 cm length	-	-
Assistive Technology	Cochlear implants [23–25]	2.5 cm	574 μW	5, 12, 49 MHz	10–25 mm length	0.5–1 Mbps	Piezoelectric
	bionic vision implants [26], [27]	2 cm	-	5 MHz	9 mm × 9 mm × 2.5 mm	100 kbps	icDT and icPT
	brain computer interfaces	-	-	-	-	-	-
	for prosthetic limbs [28],	-	-	-	-	-	-
	athletic performance monitors	-	-	-	-	-	-

Here, icDT = inductively coupled data transfer; RFID = radio-frequency identification; icPT = inductively coupled power transfer: usPT = ultrasonic power transfer.

Figure 2.3: Summary of Implanted Medical Devices and related communication methods. [58]

Figure 2.3 divides the implant application into three categories: Diagnostics (for sensing and imagery), Therapeutic (for actuators and stimulators), and Assistive Technologies (for aiding with basic faculties). All IMDs have different constraints and requirements, creating the need for different IBC technologies. Ranges needed for proper implant functionality can go up to 7-10 *cm*, and size confinement can go lower than a *mm*. The required data rate is also an important parameter since a low rate can spoil implant efficiency. In contrast, the unnecessarily high data rate can cause higher power consumption, bigger size, or higher usage of safety limits for patients. The technologies mentioned above in the figure, namely radio frequency, inductive coupling, and ultrasonic, are essential for specific possible applications with diverse ranges, sizes, and power envelope demands. The system designer's task is to sort out the available power and data transfer methods and use the most rational choice. In the next subsection, the available IBC technologies will be discussed.

2.2.1. Communication & Power Transfer Technologies

As discussed in the last section, deciding between different IBC methods is key to having an efficient design. Thus, in the following paragraphs, an introduction to various communication and power transfer methods is discussed, and the gains and losses obtained by choosing a specific method are explored. A visual representation of different methods is shown below:

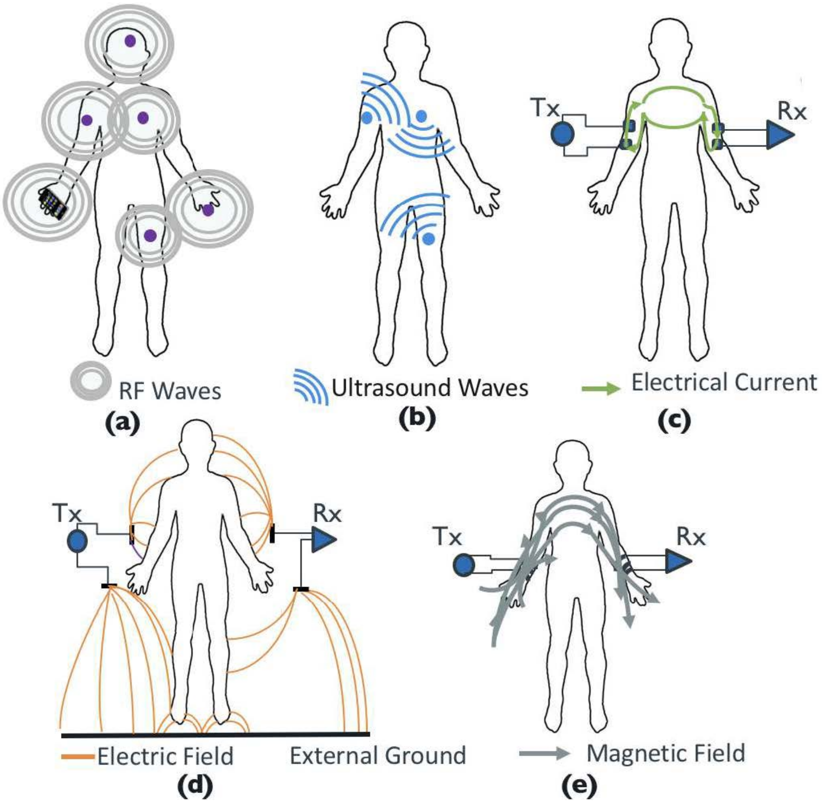

Figure 2.4: Visual schematics for available communication/power transfer technologies. [59]

(a) Radio Frequency (RF) Also known as Far-Field RF, this method uses electromagnetic waves in the radio frequency spectrum for data transfer (20 kHz to 300 GHz). Far-field RF can be used for only communication, power transfer is not possible. Radiofrequency is used for all kinds of communication technologies (e.g., AM/FM Radio, Television, Wi-fi), this communication technique is heavily studied and well-known. This results in an efficient and high-range data link, but RF can have adverse effects on human metabolism [59]. Electromagnetic radiation is measured in *Specific Absorption Rate (SAR)* values, and the implant design should be compliant with the country-specific SAR limits. For pregnancy and cancer patients, RF radiation is even more of an issue, limiting the use cases for implants that use this method for communication. With limited miniaturization possibilities, electromagnetic radiation is the biggest drawback of this type of technology.

(b) Ultrasound (US) Ultrasound refers to any sound wave that is beyond the audible sound range (> 20 kHz). This range can theoretically go up to infinity, while in reality, the maximum frequency is around a couple of GHz. US can be used for both data link and power transmission. The main benefit of the US for IBC is the fact that the safety limits for sound waves are fairly high, leading to a more widely applicable and secure IMD design. Another benefit of the US method is higher scalability for devices. Ultrasound as an intrabody communication method will be discussed further in the following subsection.

(c) Galvanic Coupling (GC) Galvanic coupling in intrabody communication (IBC) connects low-power and low-frequency voltages and currents into the human body, which serves as a transmission medium. This fact makes GC a fairly unique way to transfer data, which can act in a semi-wireless manner. Power transfer is not possible with this technology, for ensuring security of the anatomy [59]. While this method seems promising for far-away future applications, the safety and the maximum possible communication rate should be inspected fully.

(d) Capacitive Coupling (CC) This method uses a lower energy RF signal for transmission, but the difference is reception is done by a coil. Created electric field on the coil is thus coupled with the incoming electric field, imposed by transmitted RF signals. Capacitive coupling is a medium-range communication technology with reduced health risks. Still, since electromagnetic radiation is present, *Specific Absorption Rate (SAR)* levels should be confirmed in order to use on patients.

(e) Inductive Coupling (IC) Inductive coupling uses magnetic coupling between transmitter and receiver coils as a data and power transfer method. It is fundamentally similar to Qi charging, used as a modern way of wireless charging technology for a diverse set of handheld devices (e.g., smartphones, wireless headphones, smartwatches). Hence, inductive coupling as a technique for IBC is especially useful for a relatively safe power transfer, while its range is its biggest drawback. Magnetic field's attenuation on tissue is higher than acoustic pressure (US) or electric field (RF,GC,CC). This results in an abysmally small range for the distance between the external device and the implant, making possible data link applications for IC relatively limited.

(f) Optical: While not depicted in the figure above, an optical communication method is also possible, with a narrow number of operations feasible. Photon absorption, as expected, is very high on the skin; but optical data link is a promising part of bionic vision implants [54]. Using the exciting properties of the eye, the implant designer can create a high-bandwidth communication channel between the external device and the vision implant.

A trade-off chart, between the technologies depicted above, can be summarized accordingly:

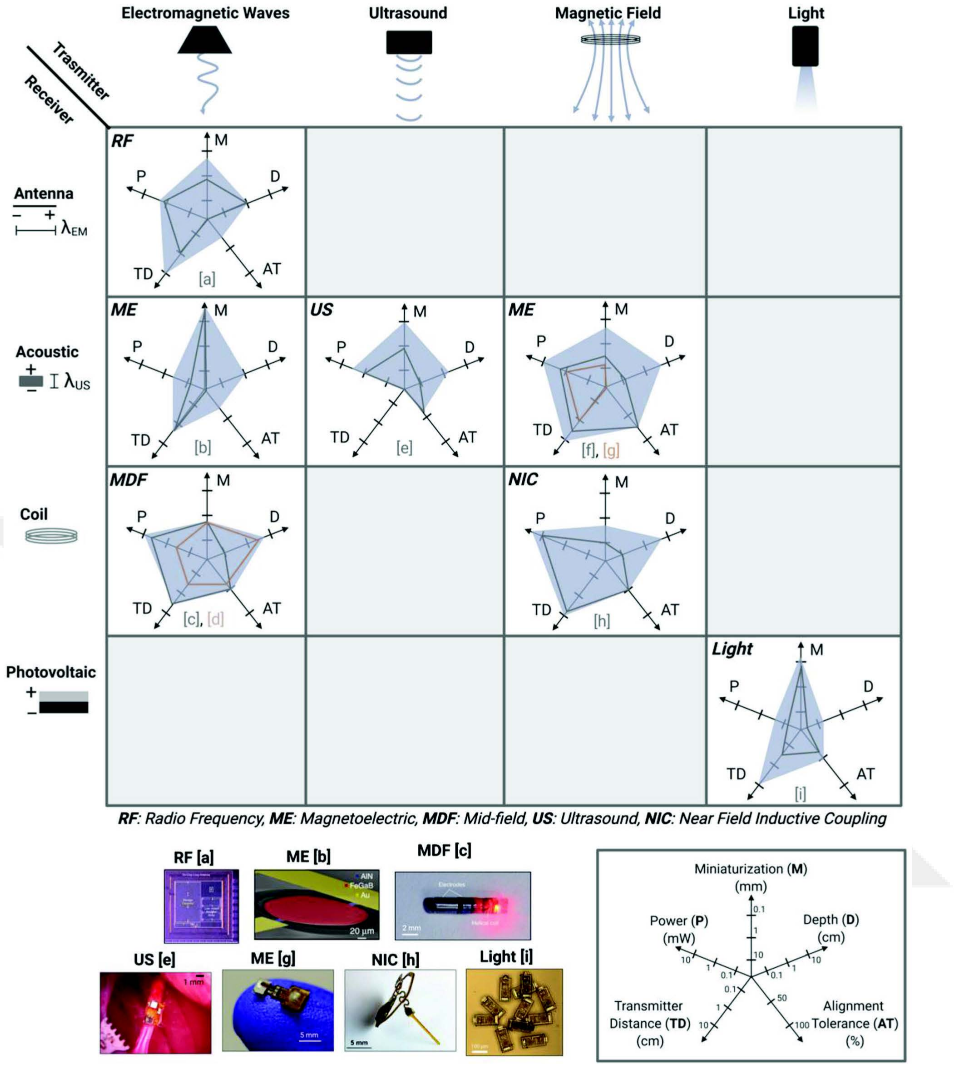

Figure 2.5: Trade-off chart between different communication and power transfer methods. [54]

2.2.2. Ultrasound in IMDs

Ultrasound usage in implanted medical device applications is a constantly evolving and promising research topic. Ultrasonic power delivery (usPT) and ultrasonic data link (US-IBC) usage in implants provide a safer and easily scalable way of providing a sufficient connection. The first biomedical ultrasound usage for a clinical diagnostic process was by Karl Dussik in 1942. Dussik was able to locate brain tumors using the attenuation variance between two local zones. In 1949, Ludwig created the first-ever ultrasound imaging device [35]. Since then, US imaging has become an integral part of life, especially for patients that may be adversely affected by electromagnetic radiation (e.g., pregnant women, and cancer patients). Modern studies for usPT and US-IBC are significant for the exact same reason: expanding the possible use cases and decreasing the population pool where implant application is not available for therapeutic or diagnostic means. In this subsection, a more in-depth look at the advantages and constraints of using ultrasound for IMD utilization will be discussed.

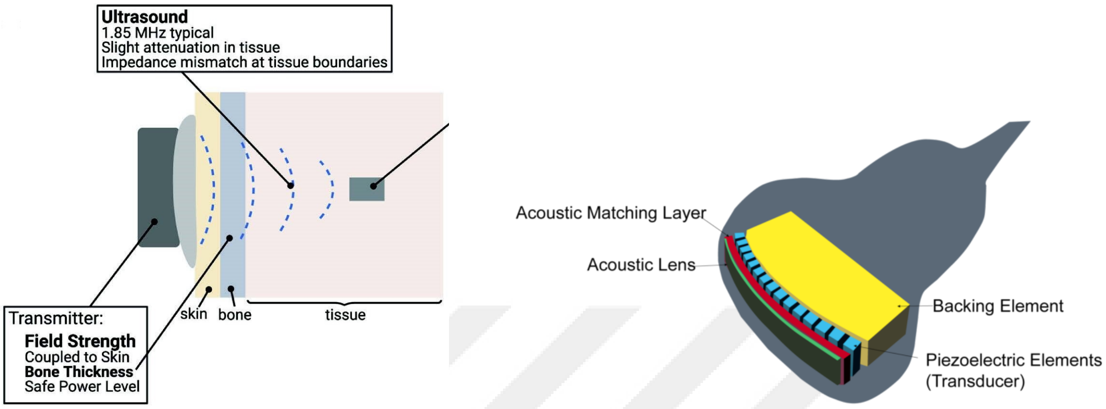

(a) Ultrasound in tissue

(b) A convex type commercial probe

Figure 2.6: (a) Schematic view and brief information for ultrasound propagation in tissue, between an implant and an external transducer. (b) The general structure of a commercial ultrasonic probe used for biomedical imaging. [54]

As explained in the previous subsection, ultrasound depicts a sound wave in the range of 20 kHz - 1 GHz. The availability of different frequencies means that higher frequencies can be used for power transmission, and the lowest possible one is for data link operations. For choosing the frequency, it is imperative to choose a value that corresponds to one of the eigenfrequencies of the mechanical system in use. This would ensure the operation at resonance, making the ultrasound generation for transmission as large of an amplitude output as possible.

Even though ultrasound is regarded as a safer alternative to RF devices, this does not mean that safety should not be taken into consideration while designing the device. As a higher frequency means a higher amount of energy supplied into the system, the safety of the implanted device should also be considered when choosing a frequency range [24]. Higher frequency devices theoretically have the ability to transfer higher data rates and higher power transmission, but regulatory safety limits should be taken into consideration. Another drawback of the high-frequency application is the heating it may cause on implants, which may result in an inoperative device, as well as safety problems for the patient.

The ability to properly miniaturize the ultrasonic implant can be counted as an advantage.

Disc-type bulk piezoelectric materials were used predominantly before 2016 [27]. These types of devices have a low level of scalability into micro, even mesoscale. Since then, a whole variety of MEMS ultrasonic transducers have become viable: among them are the PMUTs used for this thesis. The scalability of ultrasonic devices is essential to creating a minimally intrusive, secure, and low-cost IBC application. Power requirements are also lowered when a scale-down device can be incorporated, and constant development efforts towards US-IBC make higher data rates possible each year [27].

Two main hindrances to ultrasound communication are low maximum depth and poor alignment tolerances. The body consists of a diverse number of different bones, tissues, organs, and skin. The inherent heterogeneity of metabolism results in a wide range of acoustic impedance values. If the implant is located at a higher depth, undesirable scattering and reverberation inherent in the system make communication challenging. Plus, an acoustic propagation medium as dynamic as the human physique heightens the alignment problem. To overcome these problems, added redundancy in both transducers and data packages is proposed [24].

2.3. Neural Dust

The last decade saw several significant achievements in Brain-Machine Interfaces (BMI), which aim to reliably record neural signals and implement them into robotic appendages, and then also stimulate neurons from external sources. When this is possible, a treasure trove of possible new applications can become a reality: the most prominent one being complete neural control of prosthetic arms/legs for amputee patients [41]. Another exciting prospect is remote-controlled robots which may take over the assignments that are too hard to reach or too dangerous to done in person. Using a BMI, even a high-precision objective may be attainable, whereas modern robots fall short. These astonishing likelihoods are a great reason to research BMI, and a part of this future depends on neural dust.

Neural dust is a micro-scale implant tasked with reading and recording neural activity. This device can either be connected directly to the cerebral cortex (to record central nervous system/brain activities) or to a peripheral nerve (to report signals sent to arms/legs). An external transducer produces acoustic (more precisely, ultrasonic) waves that travel through skin and tissue, which in turn power the neural dust. A tiny transistor pressed up against the nerve receives power when the piezoelectric crystal in the implanted mote converts the mechanical energy of the vibrations from the sound waves into electricity [55]. The current flowing through the transistor changes in response to variations in the nerve's inherent electrical activity, serving as a read-out mechanism for the nerve's signal.

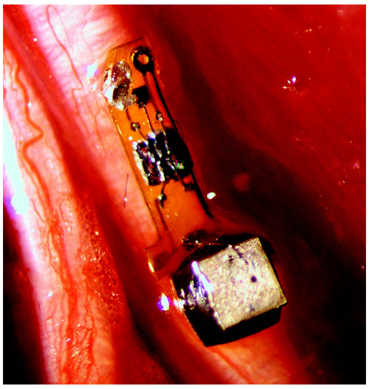

Figure 2.7: A Neural dust design surgically attached to a rat's nerve. [55]

2.3.1. State of the Art for Neural Dust

As discussed in the introductory paragraphs, most of the neural dust motes studied today directly respond to neural electrochemical processes. During the action, a cycle of depolarization and re-polarization occurs inside a neuron. This cycle is called the *action potential* and will be explored during the next subsection. This kind of "passive" approach, having the implant without any integrated circuitry (IC), enables the neural dust to require as little power as possible.

Seo et al. [34] [51] directly implanted the neural dust into the cortical tissue. The energy transfer and communication are proposed to both be done using ultrasound. The biggest challenge for ultrasound, acoustic propagation through the skull, is proposed to be mitigated using a sub-dural transceiver between neural dust and the external transceiver. This middling transducer is active, meaning battery-powered, with the mission of receiving the attenuated signal and amplifying it. The power requirement for the *passive* neural dust is supplied by this sub-dural implant. The mechanical aspect of the published two papers is very slim, while the data modulation, circuit design, and delivered power outputs are promising. Seo et al. [51] concluded in their work that a neural mote with a bulk piezoelectric cube $100\mu m$ is optimal for proper data link with a minimal power budget.

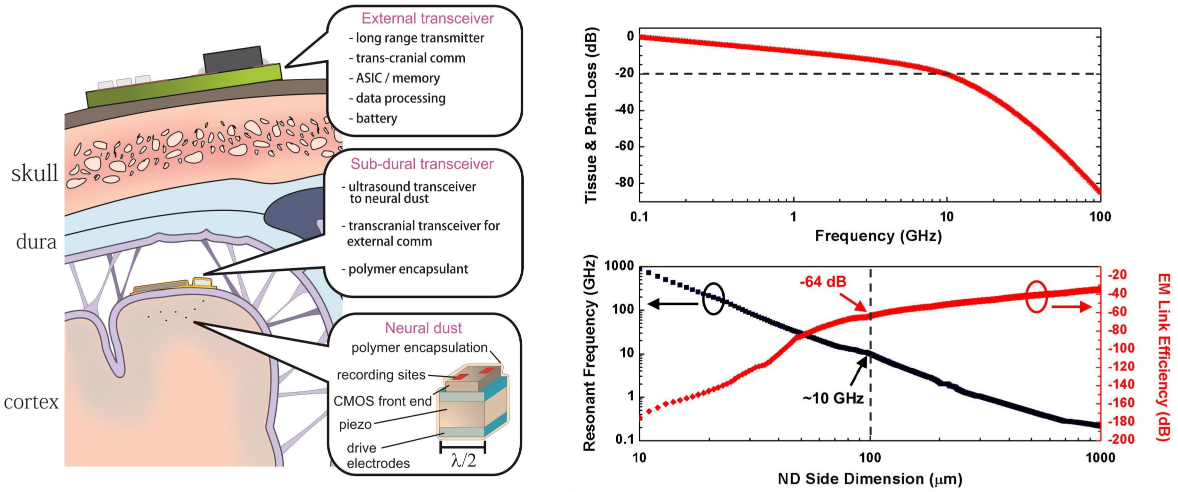

(a) (b)

Figure 2.8: (a) The proposed implant configuration in the cortex, by Seo et al. [34](b) Acoustic attenuation vs frequency on top, ultrasonic link efficiency vs neural dust side dimension on the bottom. The study concludes the dashed line is optimal. [51]

The research of Piech et al. [43] investigates a specific version of neural dust. Sometimes called *"stim dust"*, this type of neural dust contains a stimulator and a bidirectional channel for data. Intrabody communication and power delivery in the aforementioned work also use ultrasound. Stim dust technology is especially useful for the future therapeutic usage of neural dust. The data on both the external probe and the stim dust is modulated, then final backscattered data is used to reconstruct the digital bits sent to the implant. The frequency of the carrier is $1.5MHz$ and the uplink (from the external probe to implant) is continuous for power delivery, while acoustic excitation on the implant has an interval. In vivo tests show that a maximum depth of $70mm$ is viable for gel tissue phantoms. The work also discusses the transverse/longitudinal alignment and concludes a dramatic decrease (27% on 23 deg and 89% around 40 deg).

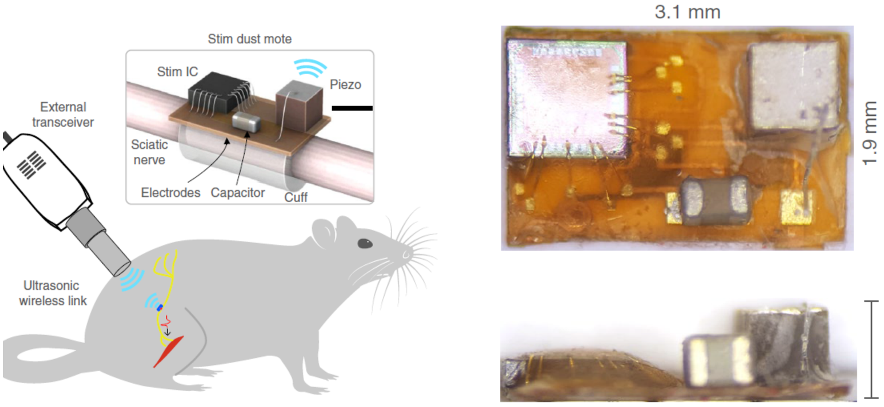

(a) (b)

Figure 2.9: (a) Schematics for the proposed stim dust by Piech et al. (b) Top and side view of the manufactured stim dust device. [43]

Body dust is another variant of neural dust (can collectively be called *smart dust*) that is tasked with body monitoring instead of neuron recording/stimulation. Using a micro-scale device for metabolic telemetry is not exactly new: a paper from 2004 discusses the possibility of the exact same concept [60]. This paper argues for a future where smart dust particles are designed to monitor blood cells. Recent technological advances in micro-manufacturing techniques and the approach of IBC methods make these types of devices more probable than ever [10].

Last but not least, the work of Seo et al [52] is the basic insight that was used during the writing of the thesis. A neural dust is attached to a peripheral nerve or a related muscle to record the neural activity, with ultrasound as the intrabody communication method. First, the external transducer sends six transmit pulses at $f_0 = 1.85MHz$ (which was referred to in this paper as *excitation cycle*) and receives the backscattered acoustic pressure at time-of-flight. These pulses are filtered, rectified, and reconstructed as digital waveforms (sampled every $100\mu s$). These waves are then integrated to approximate the action potential that occurred inside the nerve. The excitation signals are also tasked with delivering power. The manufactured mote is characterized, and in-vivo testing is done on adult Long-Evans rats. The Electromyography (EMG) readout shows compliance with a *correlation coefficient* of $R = 0.7975$, while the Electroneurography (ENG) readout of $R = 0.886$ between the reference action potential and the output one (labeled as dust on figure 2.10c and figure 2.10d). The paper concludes with the possibility of reducing the piezoelectric material profile even more to both boost the alignment tolerance and unlock the possibility of multiple neural dust motes.

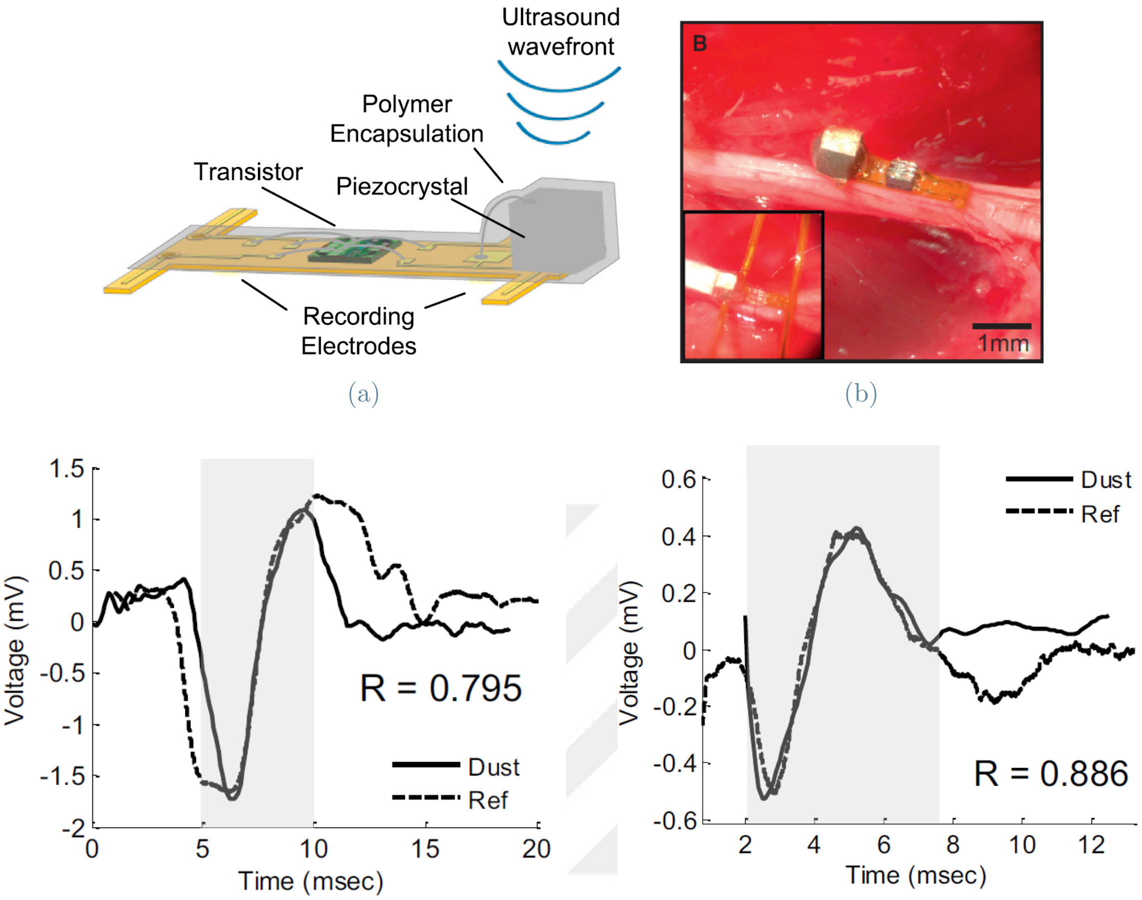

(a) (b)

(c) (d)

Figure 2.10: (a) Schematics for the proposed neural dust by Seo et al. (b) In vivo testing of manufactured neural dust. (c) EMG output of neural dust vs reference. (d) ENG output of neural dust vs reference. [52]

All research as shown above are without any sound wave propagation study. Most of the studies in the field of neural dust/intrabody communication abstain from providing any information regarding the acoustic backscattering process. While the in-vivo testings of papers [52] and [43] yield results, preliminary acoustic wave simulation would provide a cost-effective way to investigate. Thus, the objective of this thesis is to model and simulate an intrabody communication application based on PMUT arrays, while mostly focusing on the acoustics aspect of the ultrasonic backscattering effects.

2.3.2. Polarization of a Neuron

For a neuron to achieve its basic functions as an electrical transmitter and receiver, neural cells need to be polarized. This polarization leads to a resting potential of around `-70mV` and goes up to a maximum of around `+40mV` when the neuron is successfully excited. This event of polarization reversal is called the *action potential of a neuron*. Realistic and schematic graphs regarding one cycle of an action potential are on figure 2.11.

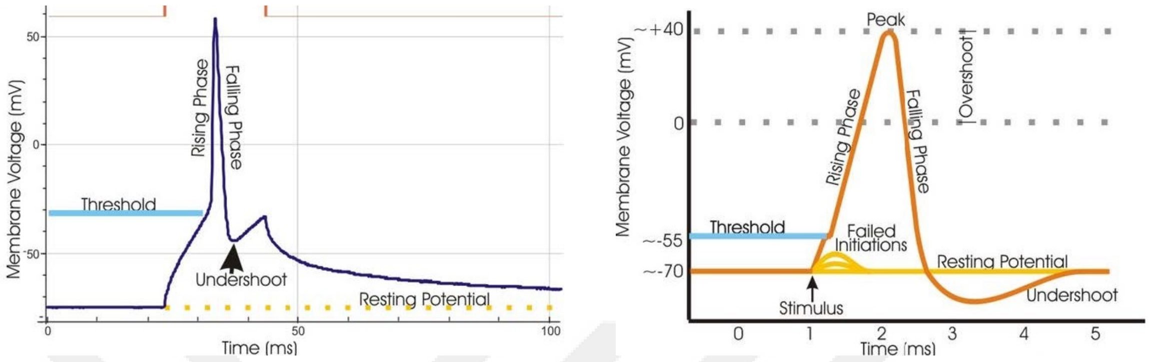

(a) Realistic Action Potential

(b) Schematic Action Potential

Figure 2.11: "Real" vs "Schematic" Action Potentials. All of the phases occurring during a cycle are shown. Resting potential and peak potential are conserved between the two graphs. [38]

Action potential has three main phases:

- *Rising phase (depolarization)* occurs when the stimulus is enough to overcome the threshold (around `-55 mV`) and the action potential is initiated. In this phase, the membrane potential is reversed from negative to positive. This is due to the saturation of $\mathtt{Na}^{+}$ atoms.
- *Falling phase (re-polarization)* is the closing stage for $\mathtt{Na}^{+}$ channels and introduction of the voltage-gated $\mathtt{K}^{+}$ channels, which causes lower sodium permeability in the membrane. In this phase, the membrane voltage is declining back to its resting levels.
- During *hyperpolarization (under-shoot)*, certain potassium channels remain open while sodium channels reset. Before the $\mathtt{K}^{+}$ channels close down, there is a period of enhanced $\mathtt{K}^{+}$ permeability, which causes an excessive discharge. This leads to hyperpolarization, which is evidenced by the drop that follows the spike.

In this thesis, the schematic action potential graph is further idealized into a perfect sinusoidal wave with similar resting and peak potentials. The voltage input graph used in the simulation is shown below:

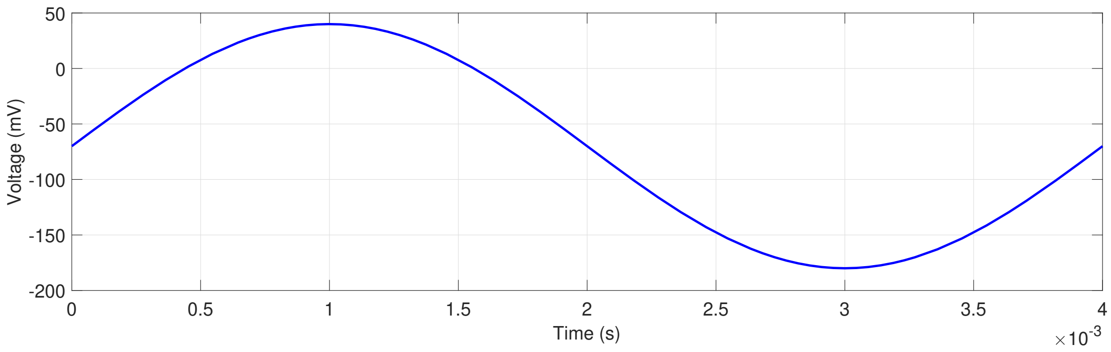

Figure 2.12: Idealized action potential graph with its key properties, used in COMSOL® simulation.

	Value	**Unit**	**Definition**
f_{neuron}	250	Hz	Neuron/Implant Frequency
T_0^{neuron}	4	ms	Period of Neuron/Implant
V_{rest}^{neuron}	-70	mV	DC Voltage of Neuron/Implant (Resting Potential)
V_{amp}^{neuron}	110	mV	Wave Amplitude for Neuron/Implant

Table 2.1: Main parameters of Implant Input Voltage

3 | Acoustic Scattering in Tissue

In this chapter, an introduction to linear acoustics used in the proposed model, as well as the basics of acoustic backscattering and time-of-flight studies, will be explored.

3.1. Introduction to linear acoustics model

A sound wave is produced by a time-varying perturbation of the dynamic and thermodynamic variables that characterize the medium. The total acoustic pressure can be mathematically expressed by the background pressure p_b and the acoustic pressure p as:

$$p_t = p_b + p. \tag{3.1}$$

The linearity of this acoustics model comes from the ability to superpose different acoustic pressure waves through the expression above. A complex sound field that is the result of multiple sources can be thought of as the sum of multiple fields, each of which is the result of a different source. Furthermore, the concept of frequency is extremely useful for linear systems. Since waves of each frequency propagate independently, it is possible to separately analyze each wave's generation and propagation as well as their frequencies and phase values before combining the results.

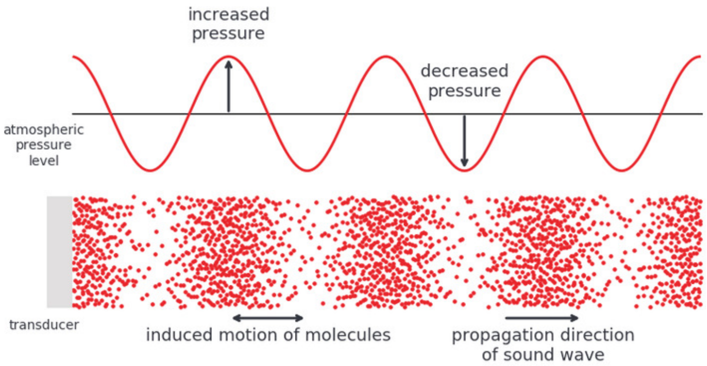

Figure 3.1: Acoustic wave propagation concerning the fluid particle oscillation. [50]

Shear acoustic waves can only occur at solid surfaces due to the impossibility of creating shear oscillations in a non-viscous fluid medium. Hence, only longitudinal waves apply to the proposed model. Longitudinal waves are acoustic waves, in which the particles of the medium oscillate along the direction of the wave propagation. Under the influence of the wave, the medium undergoes compression and tensile deformation. For liquids, this translates to various local pressure zones. This type of wave is also called *plane waves*, due to the parallel nature of propagation and oscillation directions.

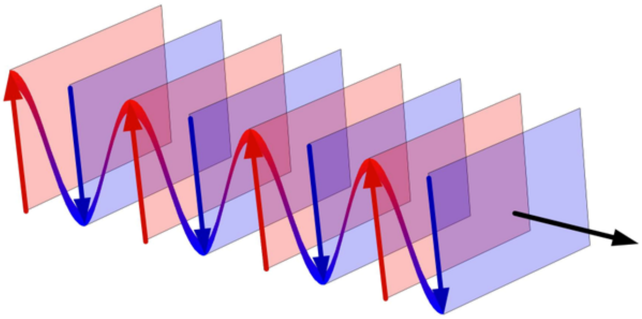

Figure 3.2: A figure depicting the nature of plane waves.

Linear acoustic waves in an inviscid medium are generally characterized by the solution of a PDE, named Helmholtz wave equation [44]:

$$\nabla \cdot (\frac{1}{\rho}\nabla p) - (\frac{1}{\rho c^2}\frac{\partial^2 p}{\partial t^2}) = 0 \tag{3.2}$$

where ρ is the density, c is the speed of sound in medium and p is the total acoustic pressure. If the density is constant throughout all acoustic propagation, the term ρ can be eliminated as:

$$\nabla^2 p - (\frac{1}{c^2}\frac{\partial^2 p}{\partial t^2}) = 0. \tag{3.3}$$

The solution of this wave equation gives the acoustic pressure profile for each point in the acoustic medium. This solution can be either a sinusoidal wave or can be represented as a superposition of sinusoidal waves:

$$p = A\cos(kx - \omega t + \phi) \tag{3.4}$$

where A denotes a constant amplitude value, k is the wave number, ω is the angular frequency and ϕ is the phase of the sinusoidal wave.

3.2. Acoustic Backscattering

The acoustic backscattering, as consistently named in this work, is the acoustic scattering phenomenon that occurred at a scattering angle of 180°. In other words, the propagation direction of the incident wave is reflected in reverse orientation, which causes the backscattered wave to travel to its source. Backscattering causes the ultrasonic pressure to travel back to the receiver, and the nature of this echo signal can then be exploited to gain insights into the metabolic events. The acoustic scattering phenomenon is observed when the acoustic wave comes across a medium that has a drastically different acoustic impedance than the current one. This results in a dispersion of acoustic pressure, either as redirected propagation or as an added phase. Separately, linear elastic and acoustic theories fail to fully define this interaction. The acoustic propagation phenomenon in both solid and fluid media, as well as the acoustic-solid boundary, needs to be taken into account.

Different acoustic regimes are also observed in different geometries:

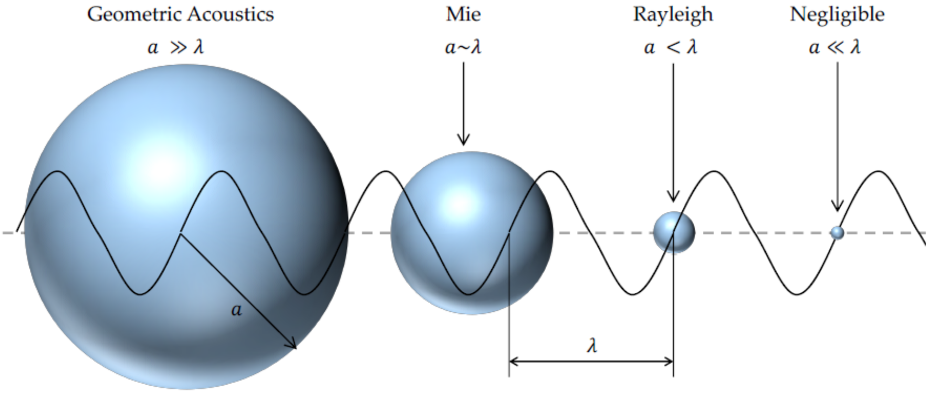

Figure 3.3: Various acoustic regimes. [49]

The defining factor between different required models comes from the relation between the dimension of the scatterer and the wavelength of the sound wave. This parameter is expressed through the dimensionless wave number ka:

$$ka = \frac{2\pi}{a}\lambda. \tag{3.5}$$

In the following work, neural dust is the object that the acoustic waves scatter. Using the parameters of the proposed model depicted in section 4.3.1, the following wave number is found to decide on the physics used in the system:

Name	**Value**
ka	8.94 >> 1

Table 3.1: Dimensionless wave number to assess acoustic regime

The acoustic regime that is therefore suitable is the *Geometric Acoustics*, and using a linear acoustics model is expected to fully capture the acoustic backscattering phenomenon that appears in the proposed simulation.

The sound wave scattering from an elastic solid in an inviscid fluid was first solved by Faran in 1951 [22], which still acts as the basis for recent mathematical studies done in this field. Faran's theory is used to describe the interaction between an elastic solid sphere, and a sound wave in a fluid medium. Allegra-Hawley [2] further developed the connection between the elastic conservation field equations and the partial elastic waves that correspond to translational, thermal, and viscous scattering responses. Then, the academic research from Hay [25] explores the viscous properties of the medium and the application of related boundary conditions needed to solve the defined boundary value problem. Hay obtained partial differential equations for viscous acoustic medium problems, and related boundary conditions that is needed to obtain the partial waves as a solution to specific wave equations.

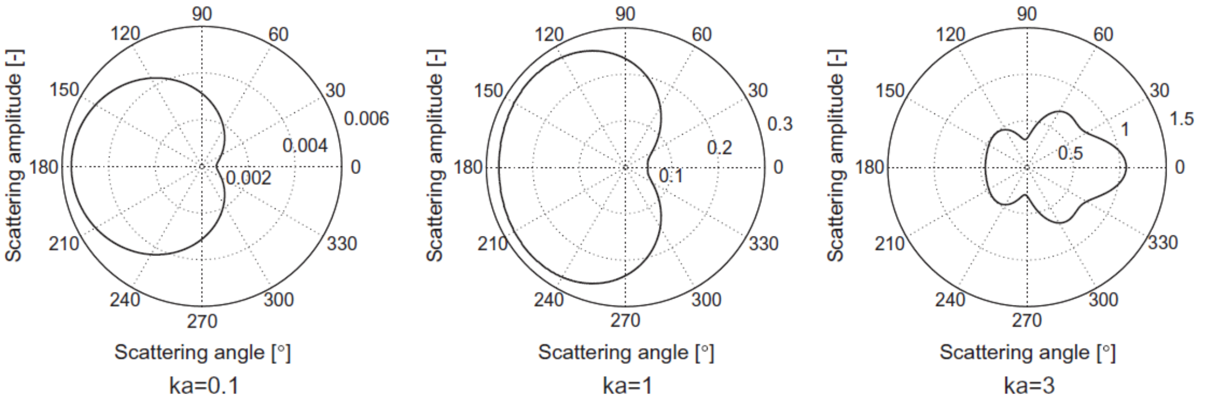

ka=0.1 ka=1 ka=3

Figure 3.4: A sound pressure level (SPL) solution of an acoustic scattering study [61]. Scattering angle 180°corresponds to the acoustic backscattering waves.

Based on the acoustic scattering exemplified by this section, a time-of-flight study is done. An acoustic perturbation is transmitted through the medium. As the concept of acoustic scattering implies, the sound wave will then propagate and scatter. Some of these scattered waves travel back (as backscattered echo) and can be collected. Assuming the medium parameters are known (i.e. speed of sound), the distance traveled by the echo can be calculated. This value is called the *time-of-flight* and is used extensively in industrial and medical applications. Flow meters, range finders, and various ultrasonic communication schemes use the concept of time-of-flight to gather data.

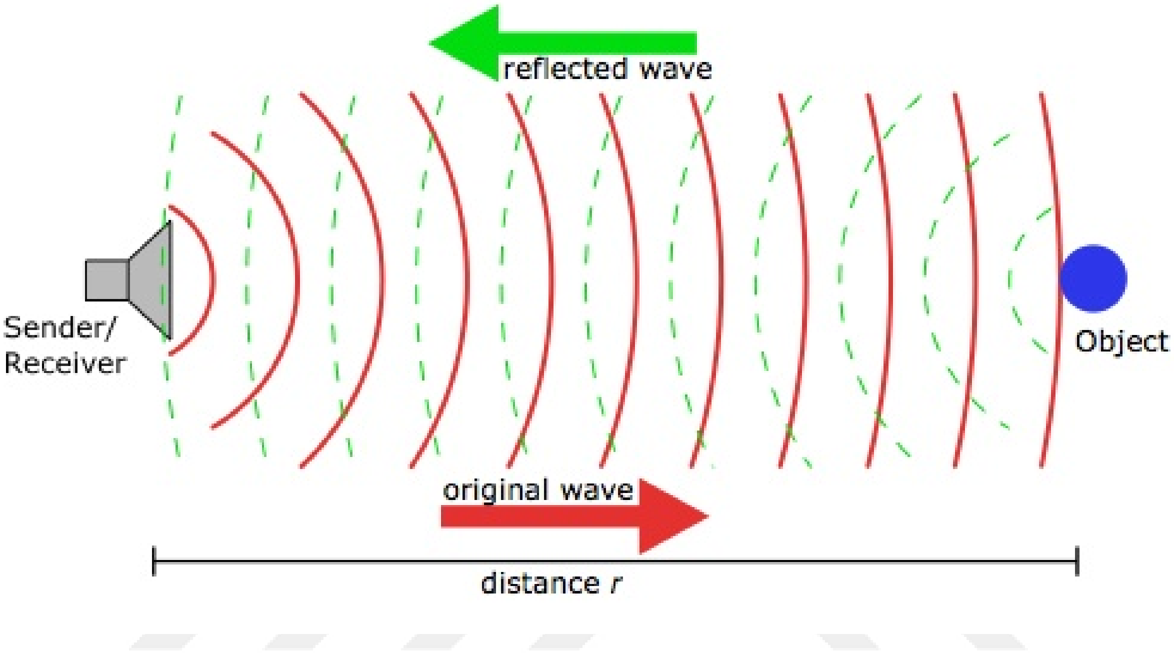

Figure 3.5: Schematics explaining the time-of-flight approach used in the study. [42]

4 | Modeling and Simulation

In this chapter, mathematical modeling, computational methods, and simulation parameters used during the *COMSOL Multiphysics* simulation are presented and discussed.

4.1. Introduction

The following proposed model has as its main undertaking the establishment of a unidirectional intrabody communication channel between the neural dust implant and the external PMUT array. This flow of data is proposed to be acquired using the theory of backscattering acoustic waves. COMSOL Multiphysics V6.0 is used for the creation and simulation of the subsequent model, while MATLAB R2021b is utilized for data processing and interpolation. A simplified neural dust communication module is considered, which consists of bulk PZT piezoelectric material and electrodes. The neural dust implant is theoretically connected to the peripheral nerve through a resistor. The implant voltage and action potential of the neuron are thus equivalent. To simulate the polarization of the neuron, a sinusoidal electric potential is applied to the neural dust bulk PZT domain, as discussed in section 2.3. Then, an external probe containing a PMUT array structure is adopted to serve two main functions: generation of the excitation waves (to incite acoustic propagation) and further collection of reflected sound waves. The basic properties of this backscattered echo, mainly phase, and time-of-flight values, are implemented to gain insight into the implant bulk PZT deformation under implant voltage. This mechanical displacement is coupled with the electric voltage due to the piezoelectric effect. The electric potential of the bulk PZT at the time of acoustic wave-implant interaction can then be calculated. It is to be noticed that only one data point is acquired during one PMUT array cycle of excitation and reception. Finally, data points are exported and gathered through multiple cycles using MATLAB and can be used to interpolate the final voltage profile output. The target solution output is expected to be as close to the action potential input as possible.

4.2. Model Definition and Governing Equations

As discussed in Chapter 3, acoustic waves tend to continue propagating forward until they encounter another body. Due to the impedance mismatch between two material mediums, a portion of the waves will be scattered around. This phenomenon is called acoustic backscattering, and the echo it creates is the basis of the subsequent model. The proposed model uses three different physics interfaces and two multi-physics coupling interfaces. *Pressure Acoustics, Transient* interface allows the study of acoustic propagation in the time domain and computes the variations of pressure under inconsistent time-dependent sources. These disturbances of pressure denote the sound waves, and it is possible to visualize the acoustic propagation in tissue medium for a specific time step. This unlocks the possibility to visualize, verify and integrate acoustic backscattering data in the proposed model. The interface is based on the discontinuous Galerkin method, which implies resource efficient time-explicit study. The pressure acoustics module is then coupled with the *Electrostatics* and *Solid Mechanics* interfaces to capture proper acoustic-solid interaction.

Governing equations: Pressure Acoustics, Transient

Pressure Acoustics, Transient interface solves the following wave equation for linear systems [7]:

$$\frac{1}{\rho c^2}\frac{\partial^2 p}{\partial t^2} + \nabla \cdot (-\frac{1}{\rho}(\nabla_p - \boldsymbol{q_d})) = Q_m \tag{4.1}$$

where $\boldsymbol{p}$ is the acoustic pressure, c is the speed of sound in medium and ρ is the equilibrium density. This wave equation is an amalgamation of the first-order hyperbolic set of linearized continuity and linearized momentum equations, expressed below:

$$\begin{cases} \frac{1}{\rho c^2}\frac{\partial p_t}{\partial t} + \nabla \boldsymbol{u_t} = Q_m & \text{(4.2a)} \\ \rho\frac{\partial \boldsymbol{u_t}}{\partial t} + \nabla \cdot (p_t \boldsymbol{I}) = \boldsymbol{q_d}. & \text{(4.2b)} \end{cases}$$

$\boldsymbol{u_t}$ represents the total acoustic pressure. Sources are noted in these equations as $\boldsymbol{q_d}$ for dipole and $\boldsymbol{Q_m}$ for monopole sources. Monopole sources are an acoustic source which acts as a radially oscillating sphere. In the *Pressure Acoustics, Transient* interface, monopole sources are available in the form of a mass source $\boldsymbol{Q_m}$. The added mass source domain configures the right-hand side of both the continuity equation and the unified wave equation, as:

$$Q_m = \frac{1}{\rho}M \tag{4.3}$$

where the M denotes the massive rate of change $[kg/(m^3 * s)]$. Dipole domain sources, on the other hand, refers to a domain volumetric force that is typically stronger in two opposite directions. This results in an acoustic source that acts as a translational oscillating sphere, defined by the volumetric force $\mathbf{F}$ $[N/m^2]$:

$$\boldsymbol{q_d} = \boldsymbol{F}. \tag{4.4}$$

The parameters used to configure the interface are summarized below:

Name	**Configuration**
Reference pressure for the sound pressure level	Use reference pressure for water: $p_{ref,SPL} = 1\mu Pa$
Typical Wave Speed for Perfectly Matched Layers	For tissue phantom: $c_{tissue} = 1568 m/s$ [21]
Maximum frequency to resolve	$f_{max,sol} = 3 * f_0^{array}$

Table 4.1: Configuration parameters for the *Acoustic Pressure, Transient* interface.

Governing equations: Solid mechanics

The Lagrangian equation of motion may be given by [23]:

$$\rho_0 \frac{\partial^2 \boldsymbol{u}}{\partial t^2} = \nabla_x(\boldsymbol{FS}) + \boldsymbol{F_v} \tag{4.5}$$

where $\boldsymbol{F}$ is the deformation gradient, $\boldsymbol{S}$ is the second *Piola-Kirchhoff* stress tensor, ρ_0 is the initial density. $\boldsymbol{F_v}$ denotes a volume body force, and applied to the current (Eulerian) geometry but expressed in Lagrangian configuration, is enumerated for various boundary conditions. Displacement field vector $\boldsymbol{u}$ can be computed using this equation of motion, however, the COMSOL interface utilizes a derivation of this equation, the *principle of virtual work*, instead. Virtual work is an energy equilibrium equation that states the variation in strain energy (internal work) should be equivalent to the work done by the sum of all external forces (external work). It is decidedly beneficial to utilize the conservation of energy when imposing thermal and electrical coupling, as well as applying most boundary conditions inherent in *Solid Mechanics* module. In a dynamic analysis like the proposed simulation, the virtual work is expressed as:

$$\begin{gathered}\delta\boldsymbol{W} = \int_V (-\delta\varepsilon : \sigma + \delta\boldsymbol{u} \cdot \boldsymbol{F_V} - \rho\delta\boldsymbol{u} \cdot \boldsymbol{u_{tt}}\ dv\ + \\ \int_S (\delta\boldsymbol{u} \cdot \boldsymbol{F_s})\ ds\ + \int_L (\delta\boldsymbol{u} \cdot \boldsymbol{F_L})\ dl\ + \sum_p (\delta\boldsymbol{u} \cdot \boldsymbol{F_p}).\end{gathered} \tag{4.6}$$

This equation formulates the Newton's second law in another way using d'Alambert principle. The subscripts V, S, L and p denotes domains, boundaries, edges, and points respectively. $\boldsymbol{F_V}$, $\boldsymbol{F_S}$, $\boldsymbol{F_L}$ and $\boldsymbol{F_p}$ represent various forces appearing in the system, and all integrals refer to the undeformed geometry. For linear geometries, ε is the engineering strain. The following contribution is then added to represent Rayleigh damping phenomenon for PMUT array:

$$\delta\boldsymbol{W} = \int_V (-\delta(\nabla\boldsymbol{u}) : \beta_{dK}\frac{\partial P}{\partial t} - \alpha dM\rho\delta\boldsymbol{u} \cdot \frac{\partial\boldsymbol{u}}{\partial t} \tag{4.7}$$

where $\boldsymbol{P}$ is the *Piola-Kirchhoff* stress tensor.

Governing equations: Electrostatics
This interface applies the following conditions for a static system [28]:

$$\begin{cases} \boldsymbol{E} = -\nabla V & \text{(4.8a)} \\ \boldsymbol{D} = \varepsilon_0\boldsymbol{E} + \boldsymbol{P} & \text{(4.8b)} \end{cases}$$

where $\boldsymbol{E}$ denotes the electric field, D is the electric displacement, P is the spontaneous polarization and ε_0 is the permittivity in vacuum. These two expressions can be collected to represent the Gauss's Law:

$$-\nabla \cdot (\varepsilon_0\nabla V - \boldsymbol{P}) = \rho \tag{4.9}$$

where ρ connotes the space charge density or electric flux. The dependent variable V can therefore be computed through this equation for all variations of variables ε_0, P and ρ.

Dependent Variables and Initial Conditions
There are three dependent variables related to this system: the acoustic pressure p, the displacement field vector $\boldsymbol{u}$ and the electric potential V. The initial conditions are as

following:

$$\begin{cases} p(0) = 0 & (4.10a) \\ \dfrac{\partial p}{\partial t}(0) = 0 & (4.10b) \\ \boldsymbol{u}(0) = 0 & (4.10c) \\ \dfrac{\partial \boldsymbol{u}}{\partial t}(0) = 0 & (4.10d) \\ V(0) = 0. & (4.10e) \end{cases}$$

The expressions (4.10a) and (4.10b) are used as initial conditions for *Pressure Acoustics, Transient* interface, equations (4.10c) and (4.10d) are used in *Solid Mechanics* while (4.10e) is applied on *Electrostatics* module.

4.3. Computational Model

In the following, a simulation model to record neural activity using acoustic backscattering will be proposed. The objective is to be able to read out the peripheral neuron activity gathered by the neural dust mote and collect this data using an external ultrasonic probe.

4.3.1. Neural Dust Design

First, a neural dust mote needs to be constructed. The geometry present in the proposed implant provides a unidirectional communication channel for the external probe. Piezoelectric materials in this data link module provide a strain change occurrence directly correlated with the voltage change in the resistor. The resistor is directly connected to a peripheral nerve, directly mediating the neural signal and the displacement field in the piezoelectric material.

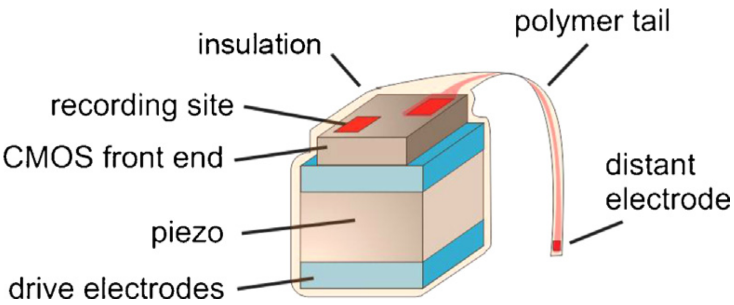

Figure 4.1: Example of a fully developed neural dust mote [51].

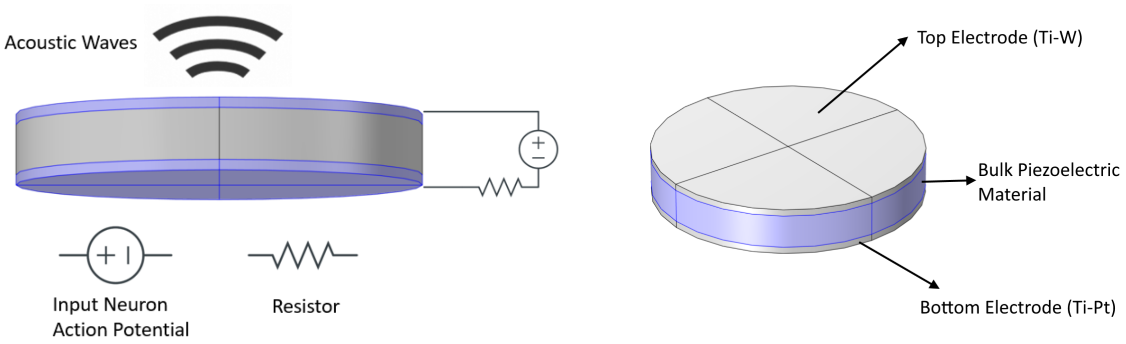

(a) Proposed neural dust implant (b) Proposed geometry structure

Figure 4.2: A schematic of the suggested neural dust design and its components.

Since the goal of the proposed model is to act as a proof-of-concept of a PMUT array in IBC, only the input voltage and the piezoelectric response of the neural dust are essential. Hence, the resistor in the neural dust to read out the action potential is absent in this model. Instead, an idealized implant voltage is directly applied to the piezoelectric material. The whole communication module is a cylinder with radius $R = 0.8\ mm$ and total thickness $H_{Total} = 0.28\ mm$. The piezoelectric material has a thickness of $H_{PZT} = 0.2\ mm$, and each of the top and bottom electrodes are $H_{electrode} = 0.04\ mm$. The proposed module design is significantly smaller than its peers, which usually contain a piezoelectric module that is a cubic design with a side of $a = 1\ mm$ [41, 51]. The volume of the suggested design is thus significantly smaller: $0.56297\ mm^3$ instead of $1\ mm^3$. This is highly beneficial for reducing the invasive nature of neural dust. As discussed in Chapter 2, neural dust motes are studied to be used as a network instead of a singular dust mote application. The reduction of spatial usage inside the body is intended to provide safer and less invasive biomedical utilization.

The input of this module, alongside with methodology used for approximation, is discussed in section 2.3.2, and more precisely the figure 2.12 and related table 2.1. Boundary conditions *Electric Potential* is used to implement the implant voltage into the simulation.

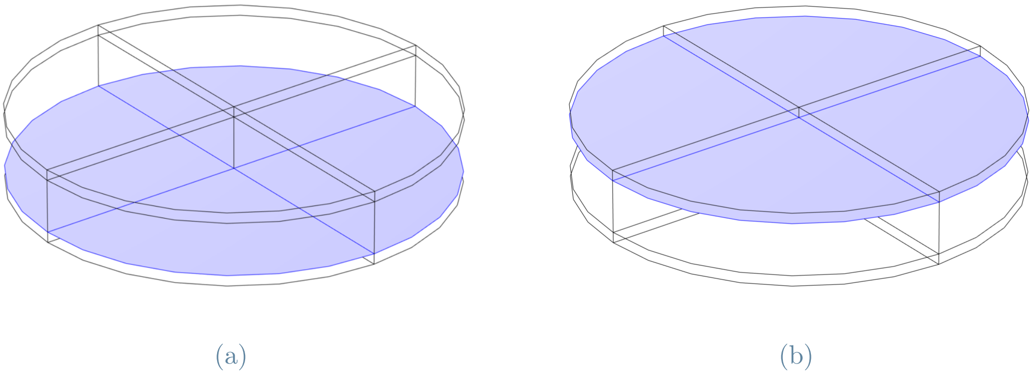
(a) (b)

Figure 4.3: (a) Boundaries on the implant communication module where the Electric Potential node is applied. (b) Boundaries on the implant where the Ground node is applied.

4.3.2. External Probe / PMUT Array Design

PMUT modules and related array configurations used in the model are based on a custom design by STMicroelectronics. In order to reduce degrees of freedom and increase resource efficiency, only a simplified layout of the PMUT is modeled.

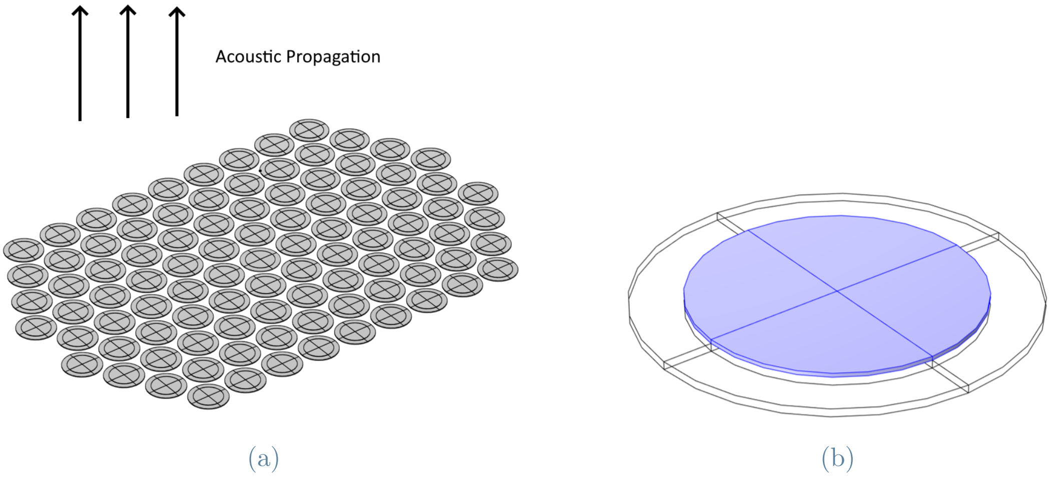

(a) (b)

Figure 4.4: (a) Proposed external PMUT array and the direction of acoustic propagation during the excitation cycle. (b) Wire-frame orthogonal view of a singular PMUT. The blue colored domain indicates the piezoelectric material layer.

An external PMUT array is used to send an excitation signal that provokes a backscattering signal and then turns into receiver mode to collect the echo. This ensures that all

PMUTs act as both a transmitter (during the excitation phase) and a receiver (in the receiver phase). The excitation phase graph and related parameters are summarized in figure 4.5 and table 4.2.

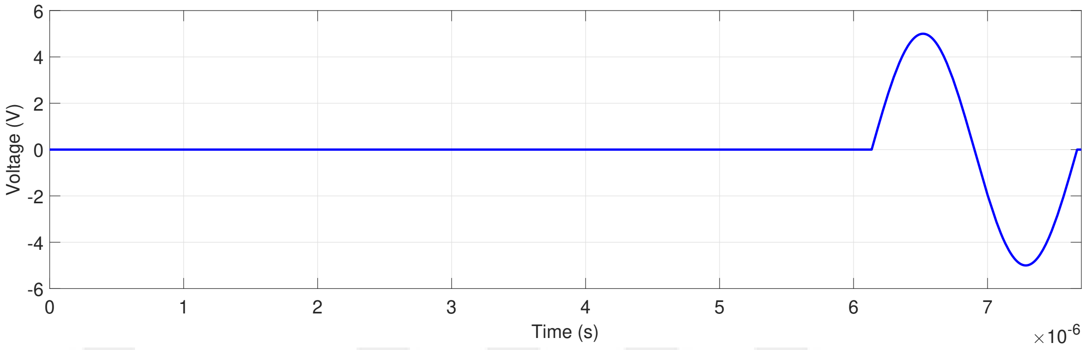

Figure 4.5: Input voltage applied on external the PMUT array during transmission/excitation phase.

	Value	**Unit**	**Definiton**
V_{DC}^{array}	5	V	DC Voltage
f_0^{array}	652	kHz	Performing frequency
T_0^{array}	1.5337e-6	s	Period
ω_0	4.1	MHz	Angular velocity
t_{delay}	6.135e-6	s	Time delay before excitation
$t_{transmit}$	7.6687e-6	s	Total time for transmission/excitation phase

Table 4.2: Main parameters for input voltage applied on PMUT array

Please note that the delay time t_{delay} is added to counteract the acoustic waves generated from the imposed non-zero implant voltage. During t_{delay}, these waves are scheduled to develop, propagate, and eventually be absorbed by the perfectly matched layer. After $t_{transmit}$, the PMUT array starts the receiving phase. The *Electrostatic* interface used in the model for managing piezoelectric properties is equipped with such physics tasks. Boundary condition applied in figure 4.6a switches from *Electric Potential* to *Floating Potential*. This is achieved by creating distinct cascading study steps for both the transmission and reception phase. The output values for the transmission step are stored and used as initial values for the reception step.

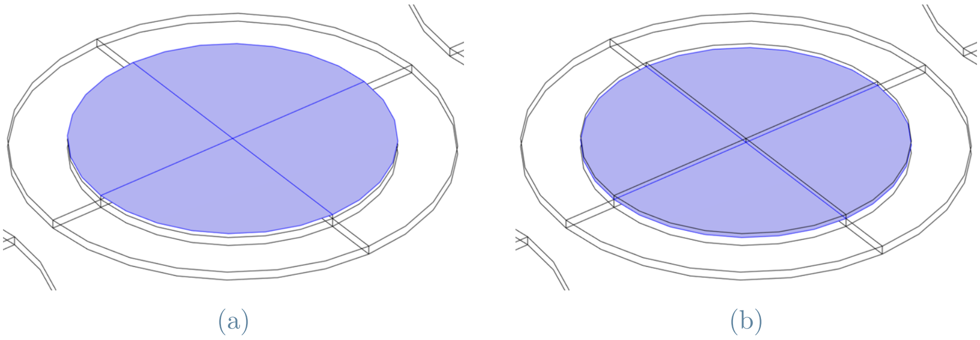
(a) (b)

Figure 4.6: (a) Boundaries on PMUT array where Electric Potential condition is applied on transmission phase and Floating Potential condition is applied on receiver phase. (b) Boundaries on PMUT array where the Ground node is applied.

Boundary condition nodes used in *Electrostatics* physics interface are [13]:

- *Electric Potential node* forces the following condition throughout the selected boundaries:

  $$V = V_0. \tag{4.11}$$

  In the studied model, a mathematical function of figure 4.5 is applied as time-dependent input, $V_0(t)$.

- *Floating Potential* is used to signify an unknown potential through a metallic electrode boundary. When the flux is zero ($Q_0 = 0$), it acts as an unbiased, perfect electric conductor. Floating potential as a boundary condition applies a constant voltage to establish the equilibrium condition depicted in equation (4.12b).

  $$\begin{cases} V = V_0 & (4.12a) \\ \int_{\partial\Omega} (\boldsymbol{D} \cdot \boldsymbol{n})\, dS = Q_0 & (4.12b) \\ -\nabla_t V = \boldsymbol{E_t} = 0 & (4.12c) \\ \boldsymbol{n} \times \boldsymbol{E} = 0. & (4.12d) \end{cases}$$

  $\partial\Omega$ represents the selected boundary and $\boldsymbol{D}$ embodies the electric displacement field. Hence, the equilibrium mentioned in equation (4.12b) is achieved by equating the incoming electric flux with the normal component of the electric displacement field. Then, the floating potential for the current PDE and time-step is found and fixed to the boundary using the boundary condition equation (4.12a). A constant electric potential means no tangential electric field should be present in the system. This condition is met using equations (4.12c) and (4.12d). Please note that the subscript t in the aforementioned equations denote *tangential.*

- *Ground node* applies ground as the boundary condition:

$$V = 0. \tag{4.13}$$

- *Zero Charge node* ensures added boundaries has the condition:

$$\boldsymbol{n} \cdot \boldsymbol{D} = 0 \tag{4.14}$$

  where $\boldsymbol{n}$ is the vector normal to the selected boundary and $\boldsymbol{D}$ is the electric displacement field. This implies zero charge on the added boundaries. Zero charge is the default boundary condition for every external boundary surface in the model.

- *Charge Conservation, Piezoelectric node*, when coupled with the 'Piezoelectric Effect' multi-physics coupling interface, imposes piezoelectric coupling into its default node. Please note that the piezoelectric relations are not directly integrated into the equation system, and without the coupling interface, imposed domain condition for this node is the same as the default *Charge conservation.*

- *Symmetry plane node* manages the boundary condition to establish symmetry or anti-symmetry in the electric field:

$$\begin{cases} \boldsymbol{n} \cdot \boldsymbol{E} = 0 \quad \text{for symmetry,} & (4.15a) \\ \boldsymbol{n} \times \boldsymbol{E} = 0 \quad \text{for anti-symmetry.} & (4.15b) \end{cases}$$

4.3.3. Complete Model Geometry

The final 3-dimensional model geometry utilizes symmetry conditions in both the xz-plane and the yz-plane. This is an integral part of the reduction of mesh elements and degrees of freedom. Further explanation will be given during the segment titled *Symmetry.* A visual breakdown of the whole model is supplied in figure 4.7:

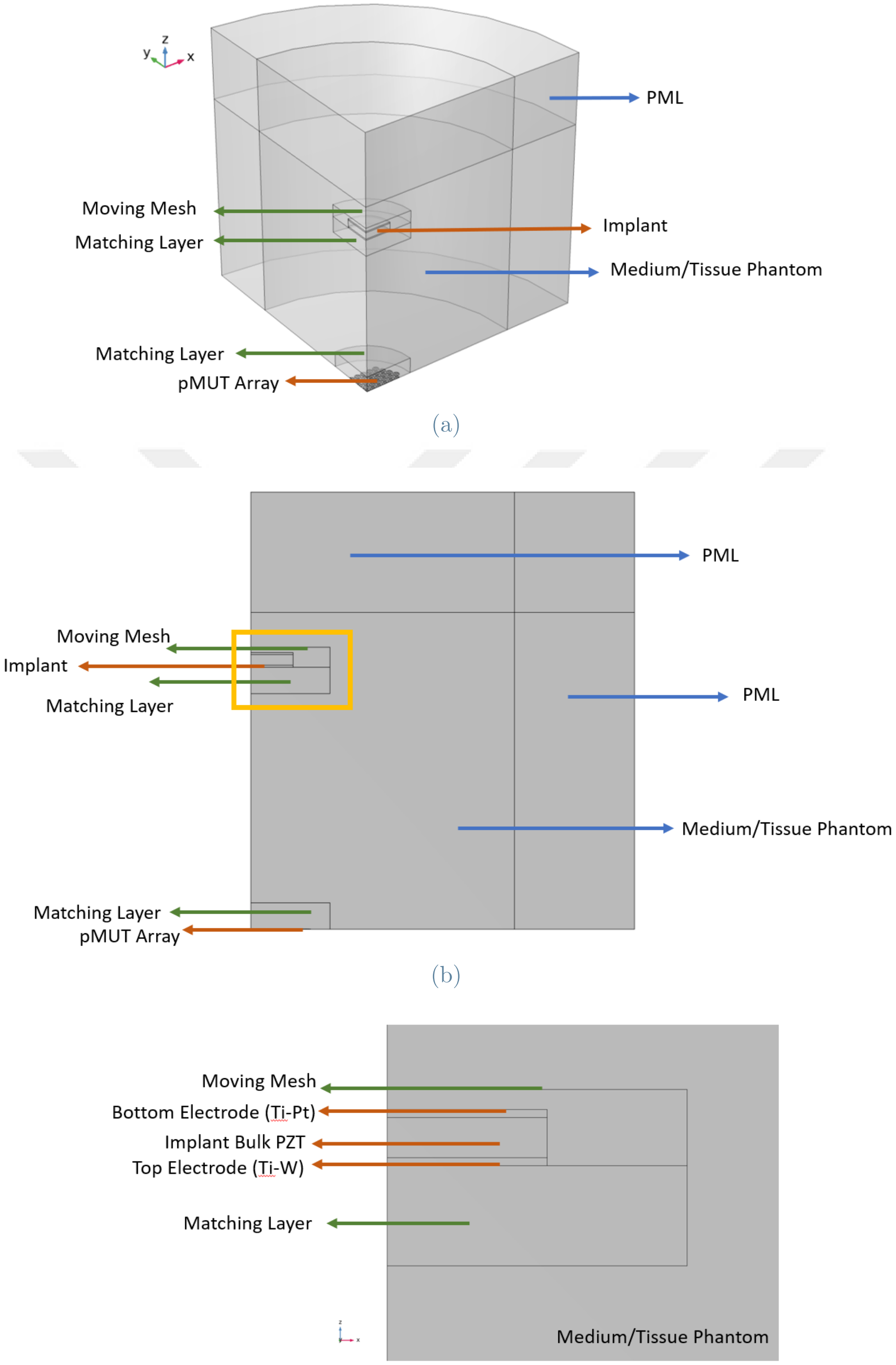

Figure 4.7: (a) 3D orthographic transparent view of the model, with descriptions. Distance between neural dust and PMUT array is 5 mm. (b) xz-plane view of the model, with descriptions. (c) Close-up of the implant in xz-plane view.

	Value	Unit	Definition
r_{tissue}	5	mm	Radius of tissue medium
H_{tissue}	6	mm	Height of tissue medium
t_{PML}	2.2761	mm	Thickness of the perfectly matched layer
r_{ML}	1.5	mm	Radius of the matching layer
H_{ML}	0.5	mm	Height of the matching layer
r_{MM}	1.5	mm	Radius of the moving mesh
H_{MM}	8.8	mm	Height of the moving mesh

Table 4.3: Dimensions of the model

Please note that the perfectly matched layer thickness is fixed to the wavelength of acoustic propagation. This parameter can be found with the formula:

$$\lambda_{tissue} = c_{tissue}/f_0. \tag{4.16}$$

where c_{tissue} represents the speed of sound in tissue phantom and f_0 connotes input excitation voltage frequency on the PMUT array.

Acoustic Propagation Medium: Tissue Phantom

In the work of Diaz et. al [21], the study involves nonlinear acoustic propagation through the thermoviscous tissue phantom media. Even though the current study can be expressed by a linear acoustic model without any thermal effects, the tissue phantom properties used in this work can effortlessly be applied to the proposed simulation model. Hence, the simplified version of the tissue phantom medium for acoustic propagation is summarized in table 4.4.

	Value	Unit	Definition
ρ_{tissue}	1044	kg/m^3	Density
c_{tissue}	1568	m/s	Speed of sound
δ_{tissue}	0.0039281	m^2/s	Sound diffusivity

Table 4.4: Main parameters of Tissue Phantom [21]

Acoustic Impedance Matching

Due to the discrepancy in the acoustic characteristics of materials, coupling waves between piezoelectric transducers, receptors, and the propagating medium becomes challenging. This mismatch can cause inefficient or sometimes even perilous data/power transfer between the implant and the external probe. As a result, the system may suffer signal distortion, a low signal-to-noise ratio, heating, and transducer wave reverberation. The coupling between different impedance values may be alleviated using a matching layer. The purpose of this matching layer is to provide an intermediary solid material step between the tissue phantom and the piezoelectric materials. A solid material suitable for matching layers needs to have similar impedance levels to the fluid propagation medium. Characteristic acoustic impedance, which is a material property, can easily be calculated using the formula:

$$z_0 = c_0 \times \rho_0 \tag{4.17}$$

where ρ_0 is the material density and c_0 is the speed of sound inside the unperturbed material medium. If we use equation (4.17) to calculate the impedance for the model, we can obtain the following table:

	Material	**Value**	**Unit in MKS***
z_{tissue}	Tissue phantom	1.637	$MRayl$
z_{PZT}	PZT	23.2	$MRayl$
z_{polySi}	Poly-silicon	22.4	$MRayl$

Table 4.5: Acoustic Impedance for materials used in the model

Please note that the unit *Rayl* here corresponds to $kg/(s \cdot m^2)$. Both the external PMUT array and neural dust module need a matching layer between them and the tissue medium. Polymers are commonly used as acoustic matching layers, with *PDMS* being one of the more common ones. PDMS is also exceptionally useful for acting as a bio-compatible encapsulating material for the implant. To observe the acoustic propagation improvements between having a matching layer or not, both studies have been run and solutions have been compared, which can be found in chapter 5. For the matching layer properties, a polymer called 'PDMS - Polydimethylsiloxane' is used [31]. The main parameters of this material, alongside matching layer geometry in the model can be examined in figure 4.8 and table 4.6.

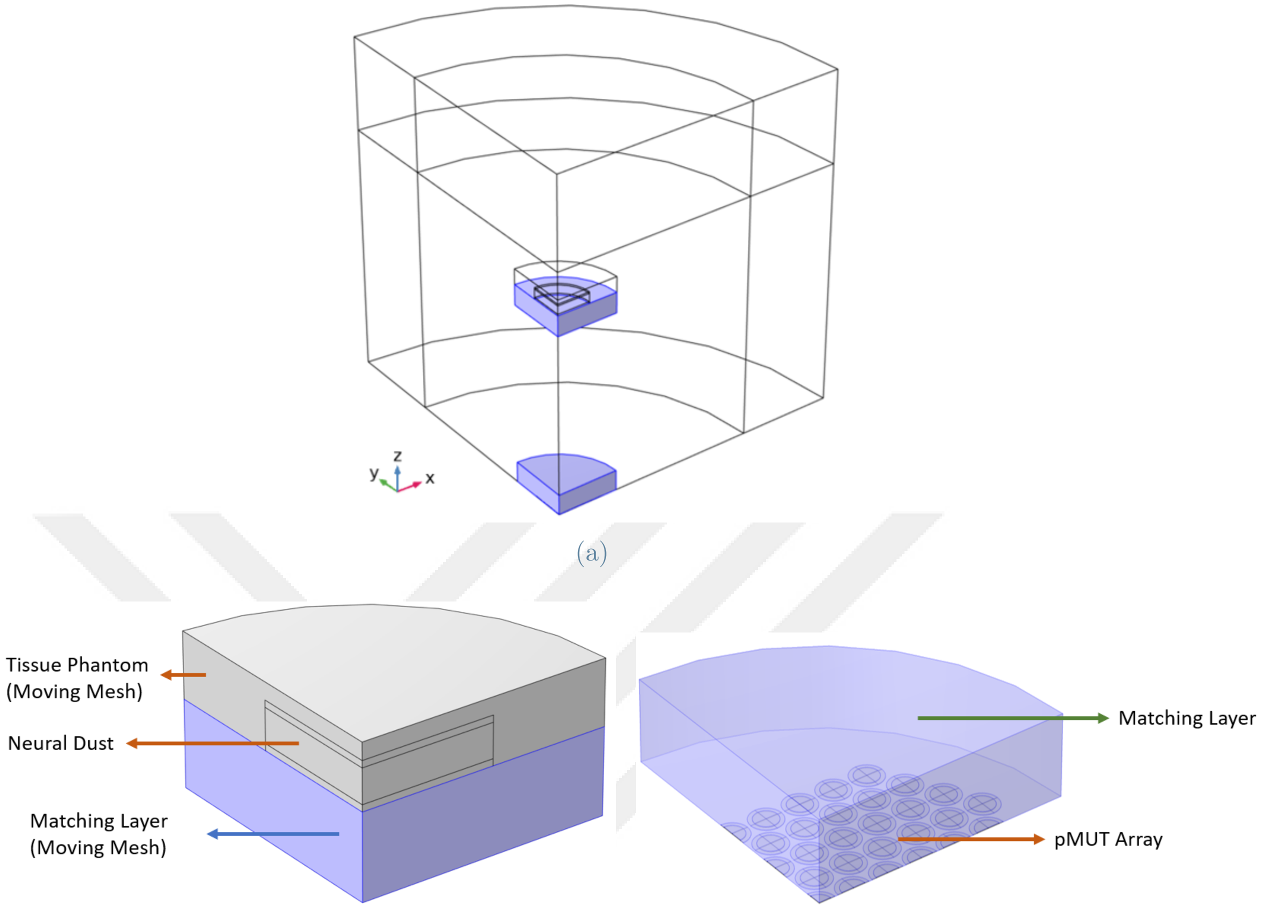

(a)

(b)

(c)

Figure 4.8: (a) Matching Layer domains in orthogonal complete model view. (b) Magnified view of the matching layer located near the neural dust implant, with descriptions. (c) Close-up transparent view of the matching layer located near the external probe/PMUT array, with descriptions.

	Value	**Unit**	**Definiton**
ρ_{PDMS}	970	kg/m^3	Density
E_{PDMS}	750	kPa	Young's Modulus
δ_{PDMS}	3.9281e-3	m^2/s	Sound Diffusivity
c_{PDMS}	1568	m/s	Speed of Sound
Z_0^{PDMS}	1.52	$MRayl$	Characteristic impedance
r_{ML}	1.5	mm	Radius
H_{ML}	0.5	mm	Height/thickness

Table 4.6: Main material parameters of PDMS [31]

Simulation of Infinite Domains: Perfectly Matched Layer

As revealed in figure 4.7, the travel distance between the external probe and the neural dust implant is 5 *mm*. The relative immense nature of this distance concerning the minimum wavelength of the traveling acoustic waves facilitates the truncation of the medium. The whole discretization model of the finite element method and its related PDEs are unable to completely simulate an infinite body. Properly truncating the domain outside of the model's *region of interest* is usually done by either artificial domains or applied boundary conditions on some physics interfaces. For this model, *Pressure Acoustics, Transient* interface provides all of these nodes, collectively called Absorbing Boundary Conditions (ABCs). None of the ABCs perfectly simulate the case of infinite domains, therefore finding the condition that best suits the needs of simulation is an integral part of the FEA process. Appropriate absorbing configuration for the model is achieved using both PMLs and the Plane Wave Radiation node.

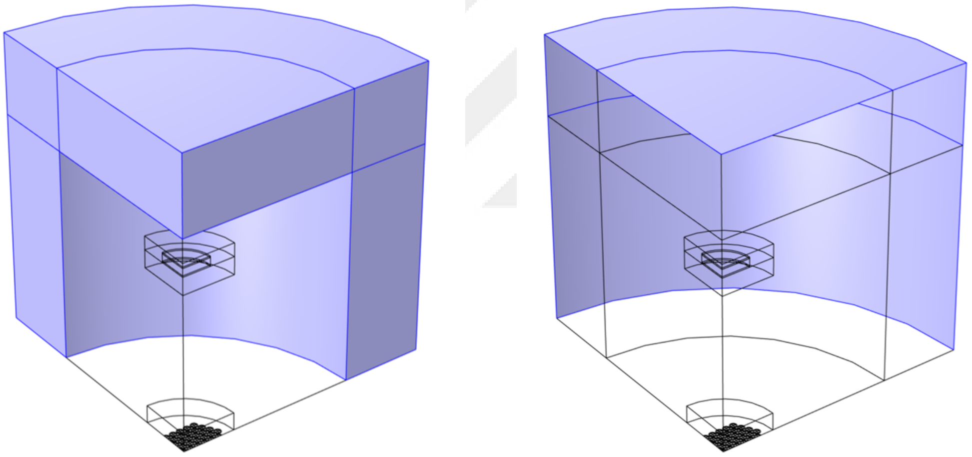
(a) (b)

Figure 4.9: (a) Selected domains for Perfectly Matched Layer node. (b) Selected boundaries for Plane Wave Radiation node. Please note that the external PMUT array is completely devoid of any ABCs, to simulate the external surface. This is a proper approximation since the possible simulation of air on this boundary would yield a condition that is similar to a sound-hard boundary.

- ***Perfectly Matched Layers (PMLs):*** PML is a type of Perfectly Matched Layer that employs a coordinate scaling technique to the virtual domains added into the node. This effectively stretches specified virtual domains towards infinity, which results in a model that converges into *infinite elements*. The difference of PML from *Perfectly Matched Layer* that can also be found as a virtual domain is the difference of domain. PML specifically scales virtual domains into the complex plane in the frequency domain, but it does not mean that PML is solely useful for frequency domain studies. The physics interface *Pressure Acoustics, Transient* is able to utilize PMLs, where the frequency variable ξ is transformed to time variable t and curvature parameter p using the formulation [6]:

$$i\omega p \Rightarrow \partial p/\partial t. \tag{4.18}$$

Due to the nature of model geometry, cylindrical-type coordinate stretching is used to provide more accurate domain scaling. This coordinate type is coupled with a polynomial stretching function, which is defined as:

$$f_p(\xi) = s\xi^p(1 - i) \tag{4.19}$$

where ξ is a dimensionless coordinate over PML layer where $0 < \xi < 1$ and s is a scaling factor. This function returns a fresh set of stretched complex coordinates over the whole virtual domain selected. Then, the complex displacements for every single direction can be calculated by:

$$\Delta\boldsymbol{x} = \lambda f_p(\xi) - \Delta_w \xi. \tag{4.20}$$

In equation (4.20), λ is a typical wavelength and Δ_w is the original thickness of the PML domain.
Artificial domains selected for PML can be viewed in figure 4.9a.

- ***Plane Wave Radiation:*** As part of the *Acoustics Module*, this node provides a set of boundary conditions to incite non-reflectance for incoming plane waves on selected boundaries. The boundary conditions applied are created to ensure minimal acoustic reflection when the incoming wave takes the form of a plane wave, which should be simply in the form of $\phi_0 e^{-ikr}$. This ABC is mainly used to further absorb any wave that practically reaches the outer shell of the PML domain. The supplementary addition of plane wave radiation ensures that any acoustic propagation entered into PML will continue propagating into infinite elements, approaching more and more the desired goal of an infinite tissue medium.

Boundary Conditions

The proposed model contains three physics interfaces, namely, *Pressure Acoustics, Transient*, *Solid Mechanics* and *Electrostatics*; and two multi-physics interfaces: *Acoustic-*

Structure Boundary and *Piezoelectric Effect*. The purpose of the following segment briefly explains the conditions applied and visualizes the boundaries where these conditions are applied.

For *Electrostatics* interface, the boundary conditions can be found in section 4.3.2.

For *Pressure Acoustics, Transient* interface, the following nodes are utilized [5, 7]:

- *Sound Hard Boundary (Wall) node* adds a boundary condition to assign the selected boundary as a wall or sound hard boundary. This creates a perfectly reflective boundary, where every acoustic wave interaction results in zero transmission beyond the added boundary. The conditions applied to every boundary are written below:

$$\begin{cases} -\boldsymbol{n} \cdot (-\frac{1}{\rho_c}(\nabla p_t - \boldsymbol{q_d})) = 0 & \text{(4.21a)} \\ \frac{\partial p_t}{\partial \boldsymbol{n}} = 0 & \text{(4.21b)} \end{cases}$$

  where $\boldsymbol{n}$ is the normal vector, ρ_c is the fluid density and p_t is the total acoustic pressure. Since any dipole source is absent in our model ($\boldsymbol{q_d} = 0$), equation (4.21a) reduces to equation (4.21b). This condition forces the normal derivative of acoustic pressure at the boundary to be zero, adequately eliminating acoustic transmission beyond.

  This node is the default for every exterior boundary in the model and is effectively used in our model on the external surface near the PMUT array. Since the acoustic impedance mismatch of air and tissue phantom medium is extremely high, a sound hard wall is a good approximation for the PMUT array boundary. A visual representation can be seen in figure 4.10a

- *Symmetry node* is used for dividing the model into four symmetrical parts, dramatically reducing the element size and degrees of freedom of the final study. The boundary conditions for this node are mathematically a carbon-copy of the *Sound Hard Boundary (Wall) node*. Boundaries added to this node are featured on the following figure 4.10b:

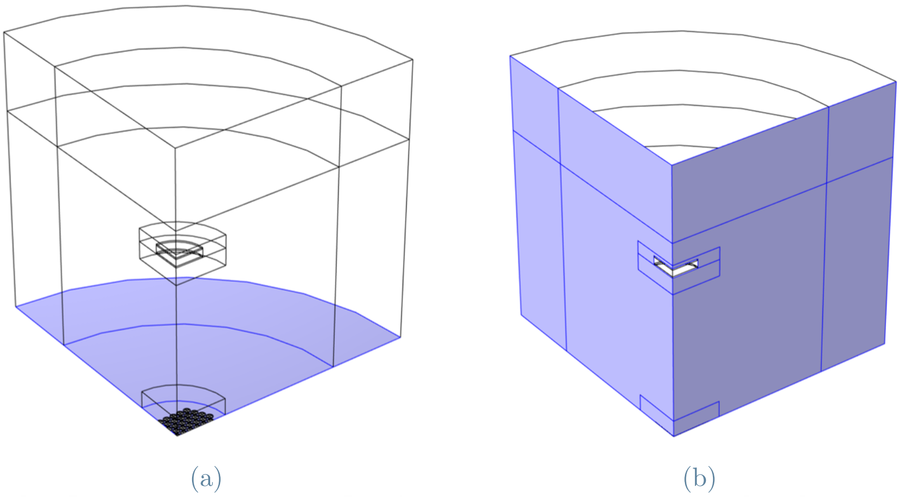
(a) (b)

Figure 4.10: Boundaries with added conditions for (a) Sound Hard Boundary (Wall), (b) Symmetry.

- *Plane Wave Radiation:* This node is discussed in depth in previous paragraphs, i.e., here in section 4.3.3.

In terms of the *Solid Mechanics* module, the boundary conditions are [15, 23]:

- *Fixed Constraint node* sets all possible displacements and rotations of the boundary to zero. The boundary conditions set for this node are fairly trivial:

$$\delta_{ij} = 0 \quad \forall \quad \{i, j\} = 1, 2, 3 \tag{4.22}$$

  where δ_{ij} denotes the mechanical displacement. This boundary condition is used to fix the implant and PMUT array without obstructing the usability of the devices. For implant, a fixed boundary is located at the bottom of the bottom electrode, since realistically *the printed circuit board (PCB)* would be located there for the whole neural dust package. For PMUTs, the fixed constraint node is applied around the periphery of the device, to mimic the membrane structure usually found in PMUT devices. These boundaries can be viewed in figure 4.11a.

- *Roller node* adds a condition to the boundary similar to fixed constraint: the selection is fixed in displacements that is normal to the boundary, while completely free for displacements on any tangential directions. This condition gives a piston-like quality to our neural dust communication module. Roller condition applied to peripheral areas of bulk PZT, top electrode and bottom electrode stabilizes the piezoelectric response and ensures the piezoelectric material is operating at 3-3 mode.

Comprehensive information for different piezoelectric modes can be found in section 1.2, while the boundaries can be viewed in figure 4.11b.

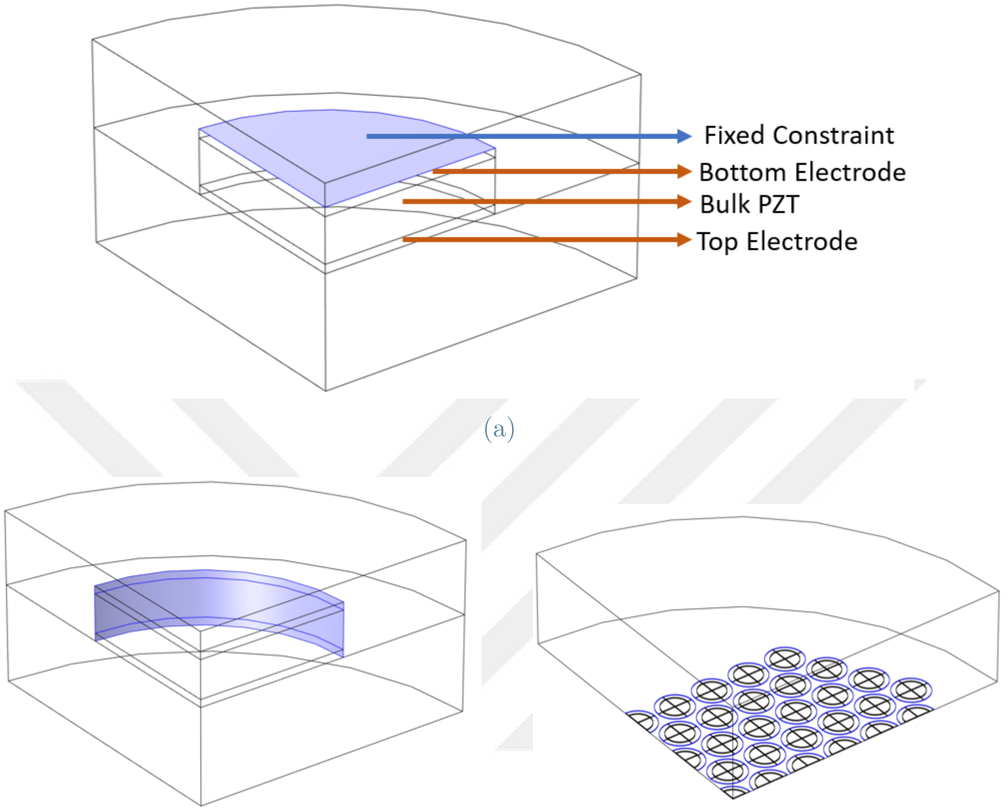

(a)

(b)

(c)

Figure 4.11: Close-up orthographic view of neural dust implant, with (a) fixed constraint, with descriptions and (b) roller condition boundaries. (c) Close-up orthographic view of external PMUT array, with the fixed condition, highlighted. Roller BC is not used in the PMUT array.

- *Damping in PMUT Array:* Damping models are implemented for modeling the intrinsic frictional damping present in solid domains. The following equation of motion describes a general solid body with damping [33]:

$$m\frac{d^2\boldsymbol{u}}{dt^2} + c\frac{d\boldsymbol{u}}{dt} + ku = f(t) \tag{4.23}$$

where $\boldsymbol{u}$ denotes the displacement vector, m is the mass of the solid body, c is the damping parameter and k is the stiffness parameter of the system. Rayleigh damping defines the c variable using the mass damping parameter α_{dm} [1/s] and stiffness damping parameter β_{dK}[s]:

$$c = \alpha_{dm} m + \beta_{dK} k. \tag{4.24}$$

Parameters used in Rayleigh Damping are also equivalent to the damping ratio through equation (4.25):

$$\xi = \frac{1}{2}(\frac{\alpha_{dm}}{\omega_0} + \beta_{dK}\omega_0) \tag{4.25}$$

where ω_0 refers to the angular velocity of the system while ξ has the following conditions:

$$\begin{cases} \xi = 0 \quad \textit{undamped} & (4.26) \\ \xi < 1 \quad \textit{underdamped} & (4.27) \\ \xi = 1 \quad \textit{critically damped} & (4.28) \\ \xi > 1 \quad \textit{overdamped} & (4.29) \end{cases}$$

Rayleigh Damping is applied on both the Poly-Si backing and PZT material domains. Without proper damping, prolonged residue oscillations are likely to occur after the excitation phase. This greatly hinders the floating potential obtained from acoustic back-scattered echo. In order to simulate a proper receiving phase for the PMUT array, relieved from signal interference, damping is imperative. A low quality-factor Q_{dm} is thus essential for fast dampening, in order to minimize the interference from the ring-down oscillations. To apply Rayleigh damping parameters into the model, a new *Linear Elastic Material* domain node is created for Poly-Si domains. For PZT, the already developed *Piezoelectric Material* domain node is used to integrate damping into the system. Please be reminded that the bulk PZT present in the neural dust communication module is free from damping. Parameters used for Rayleigh Damping integration are summarized in the following table 4.7:

	Value	**Unit**	**Definiton**
α_{dm}	9.4248	MHz	Mass Damping Parameter
β_{dm}	0	s	Stiffness Damping Parameter
Q_{dm}	1	$-$	Quality Factor

Table 4.7: Rayleigh Damping parameters applied on PMUT Array

4.3.4. Meshing

Meshing is an integral part of any FEA application. Since the Finite Element Method reduces infinite degrees-of-freedom partial differential equations into two or three spatial variables and applies them over a finite number of elements, proper meshing is crucial for accurate simulation results. This is more true than ever for the proposed model, where the voltage difference for the action potential is minimal and the accuracy of every data point is significant for error reduction. Improper meshing may lead to insensitive output, which can increase the error in the results drastically. Thus, the following meshing methodology is adopted to reduce inaccuracies. All mediums present in the model are meshed using free tetrahedral type mesh, with the size of the elements related to the wavelength of sound waves in the medium. This value can be calculated with the formula:

$$\lambda_{medium} = \frac{c_{medium}}{f_0} \tag{4.30}$$

where c_{medium} is the speed of sound value for the medium and f_0 is the fundamental frequency of the propagating acoustic waves in a medium. In the proposed model, f_0 value can be estimated as the frequency of PMUT excitation. When used, the equation 4.30 delivers the wavelength values of $\lambda_{tissue} = 2.4049\ mm$ for tissue phantom and $\lambda_{ML} = 1.65\ mm$ for matching layer (PDMS). For perfectly matched layers (PMLs), the suggested mesh elements size associated with λ tends to be around 2-4 elements per wavelength. PML virtual domain thickness is adopted as being exactly equal to one wavelength in a tissue phantom, as discussed in the last section 4.3. A proper maximum element size is thus to be selected as half the wavelength to ensure at least 2 mesh elements are present all through the Perfectly Matched Layer domain. For the solid materials, namely, piezoelectric, electrode, and poly-silicon domains; a different procedure is desired. For cylindrical miniature devices like the PMUT array and the neural dust, the available three-dimensional free tetrahedral mesh type is insufficient for proper meshing. Conforming tetrahedron elements into a cylinder would require either erroneous meshing or an inordinate amount of elements. This in turn creates a resource-hungry simulation, which is to be avoided. For this reason, two-dimensional free triangular meshes are created and extended into the three-dimensional body using the swept function. This combination is called the *wedge elements*. The maximum mesh element size is related to the device geometry in order to provide a sufficient number of elements throughout the thickness of the implant and the external probe. The final maximum mesh element sizes used in the model are summarized in table 4.8.

Domain	Max. Element Size	Mesh Type
Tissue Phantom (Medium)	0.20041 *mm*	Free Tetrahedral
PDMS (Matching Layer)	0.12025 *mm*	Free Tetrahedral
Neural Dust (Implant)	0.10308 *mm*	Wedge Elements
PZT on PMUT Array	0.01725 *mm*	Wedge Elements
Poly-Si on PMUT Array	0.0125 *mm*	Wedge Elements
Perfectly Matched Layer (PML)	1.2025 *mm*	Free Tetrahedral

Table 4.8: Mesh properties for different model domains

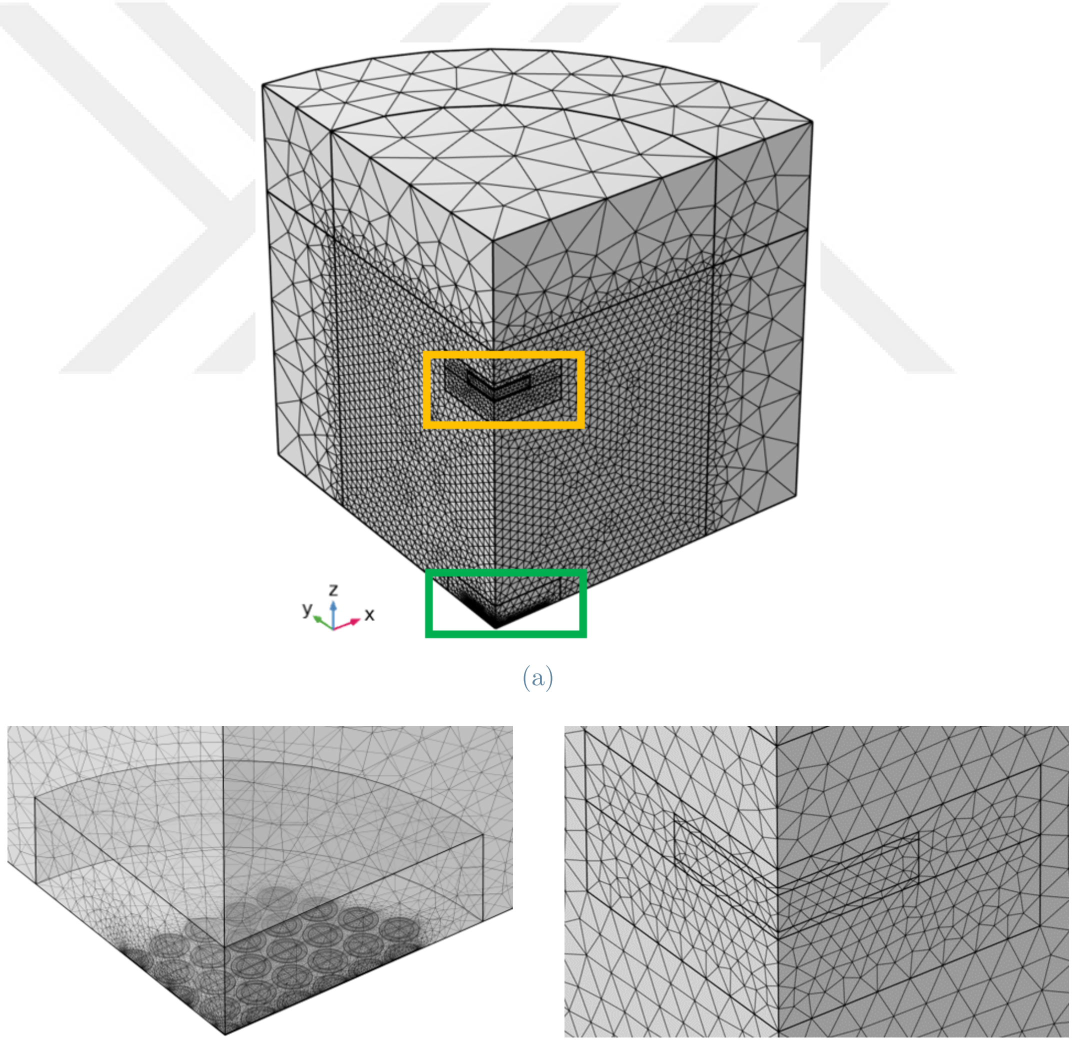

(a)

(b)

(c)

Figure 4.12: (a) Extended orthographic view of the complete meshed model. (b) Transparent magnified view of the PMUT array, shown as the green rectangle. (c) Magnified view of the neural dust implant, shown as the orange rectangle.

Moving Mesh

Pressure Acoustics, Transient interface assumes that the solid domain deformations as perturbations of pressure, and the computational domain is rigid in time. For preliminary acoustic time-of-flight studies, this assumption is satisfactory; but the deformed acoustic-structure boundary is an essential part to discern any change between different data points. The boundary between the neural dust implant and the tissue phantom needs to be deformed in regard to the piezoelectric material response. If not, all excitation waves are expected to back-scatter from the same boundary, thus returning nearly the same results. The proposed model avoids this oversight using a deformed geometry feature called "Moving Mesh". This function is used to study moving boundary problems, especially useful for models with solid deformed domains immersed in a fluid that reacts to said deformation. More specifically, the moving mesh node deforms the spatial (Eulerian) frame into the material (Langrangian) frame. The spatial frame refers to the current (deformed) configuration of the system, with coordinates represented as equation 4.31a as vector. On the other hand, the material frame relates to the reference (undeformed) configuration with vector notation of equation 4.31b.

$$\begin{cases} \boldsymbol{x} = [x, y, z] & (4.31a) \\ \boldsymbol{X} = [X, Y, Z] & (4.31b) \end{cases}$$

The mesh deformation can mathematically be explained as [16]:

$$\boldsymbol{x} = \boldsymbol{f}(\boldsymbol{g}(\boldsymbol{h}^{-1}(\boldsymbol{X_m}, i), p), t). \tag{4.32}$$

In this scenario, f corresponds to a unit map for the spatial and material frames coincide, g relates to a unit map for the material and geometry frames coincide, and the inverse mapping of $\boldsymbol{h}^{-1}(\boldsymbol{X_m}, i)$ is initially a unit map and but updated after each remeshing operation by interpolation. This infers that the spatial frame coordinates are updated after every automatic remeshing operation and are deformed relating to the reference/material frame.

The moving mesh is incorporated into the system using the following nodes/boundary conditions (BCs):

- *Deforming Domain node* defines the domains that the deformed mesh geometry is applied. Exterior mesh element nodes are controlled by either deformed mesh boundary conditions or implicit continuity constraints. Deformed mesh BC takes precedence. Interior element nodes are controlled by the Laplace smoothing equations on equation 4.33a for static and equation 4.33b for a transient case.

$$\begin{cases} \dfrac{\partial^2 \boldsymbol{x}}{\partial \boldsymbol{X^2}} + \dfrac{\partial^2 \boldsymbol{x}}{\partial \boldsymbol{Y^2}} = 0 & \text{(4.33a)} \\ \dfrac{\partial^2}{\partial \boldsymbol{X^2}} \dfrac{\partial \boldsymbol{x}}{\partial \boldsymbol{t}} + \dfrac{\partial^2}{\partial \boldsymbol{Y^2}} \dfrac{\partial \boldsymbol{x}}{\partial \boldsymbol{t}} = 0 & \text{(4.33b)} \end{cases}$$

Domains that adhere to the deforming domain node can be seen in figure 4.13a.

- *Prescribed Mesh Displacement node* allows prescriptive mesh movement on selected boundaries. When the mechanics of the system are perfectly linear (e.g., a structure with imposed rotation), this BC can be used to manipulate the elements in a way that the deformed mesh moves perfectly in line with the arbitrary mechanical movement. In the proposed model, output displacement variables of the *Solid Mechanics* interface is used to create a fluid response alongside the solid domain. For each time step, the input voltage for neural dust creates revised displacement coordinate values for solid mechanics deformation (u, v, w). These results are then used as displacement prescriptions for this node. Applied boundaries are shown in figure 4.13b.

- *Symmetry/Roller node* is used on flat symmetry boundaries to prevent out-of-bounds mesh displacement. Similar to a roller condition on solid mechanics module, the mesh is allowed to move tangentially but not normally to the boundary surface. Symmetry/roller configuration is visualized in figure 4.13c.

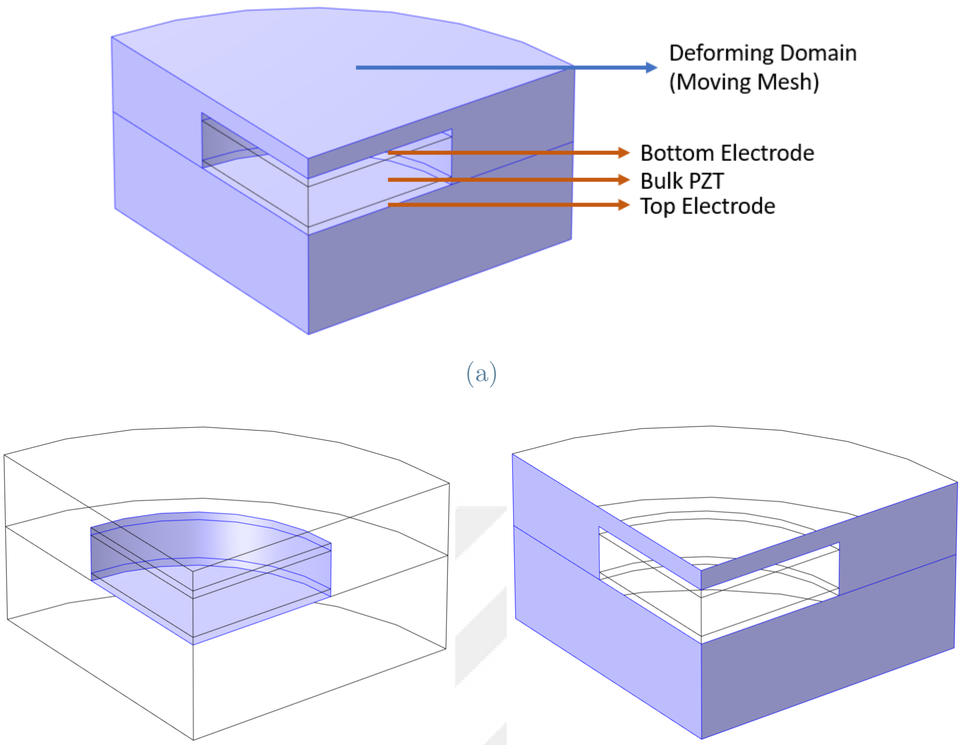

(a)

(b)

(c)

Figure 4.13: Close-up orthographic view of neural dust implant, with (a) deforming domains, with descriptions, (b) prescribed mesh displacement boundaries and (c) symmetry/roller boundaries.

4.3.5. Study Parameters and Solver Settings

The proposed study is run with three distinct cascading steps:

- *Step 1: Initialization (Stationary)* step is used to reduce the acoustic disturbance caused by the non-zero DC Voltage of the neural dust. As explained in chapter 2.3, the resting potential for the action potential is $-70mV$, effectively acting as a step function between $0V$ and $-70mV$ at $t = 0$. This causes some minute disturbances to occur, hence a stationary step to initialize the model is required. The Newton Raphson method is used to solve this stationary step. Time-dependent variables, such as neural dust and PMUT array input voltage, as well as Automatic Remeshing, are absent in this step. Instead, a constant initiating voltage is applied to the implant.
- *Step 2: Transmission/Excitation Phase (Time-dependent):* This phase imposes the excitation setup explained in table 4.2. The PMUT array acts as a transmitter in this step, generating an excitation signal to cause acoustic interaction at the

implant boundary. The excitation signal is imposed as *Electric Potential* BC with the input as figure 4.5, while the time-dependent implant input voltage is applied as figure 2.12. The automatic Remeshing function is also enabled in steps 2 and 3.

- *Step 3: Reception Phase (Time-dependent):* The PMUT array acts as a receiver during this step. *Electric Potential* node is deactivated and replaced with the *Floating Potential*, as explained on chapter 4.3.2. Any other configuration is exactly sustained from step 2, such as the *Electric Potential* node used on the implant.

Step Name	**Time Range in T_0^{array}**	**Time Range in T_0^{neuron}**	**Time Range (in μs)**
Excitation	0 - 5	0 - 1.917e-3	0 - 7.6687
Reception	5 - 20	1.92e-3 - 7.67e-3	7.6687 - 30.675
Time Step	1/8	1/20864	0.19172

Table 4.9: Time ranges for different study steps, and time step value used for all steps

Instead of storing times as the interpolation of steps taken, all steps calculated by the solver are stored. Even though it drastically increases the model file size, getting data points as accurately as possible is vital for this model. The PMUT array is designed for high data rate acquisition, making higher resolution of the time step solution a requirement. As discussed in the previous sections, the phase and amplitude differences between different back-scattered acoustic echos are minuscule. Interpolating the solution in any way adds to the final output error, and hence should be avoided. For **the time stepping method**, generalized-α is used to eliminate damping effects that appear on the low order BDE method. Generalized-α method is preferred to get more accurate results especially for pressure acoustic simulations where the frequency is relatively high. The biggest drawback of generalized-α method is the lower stability [14]. Steps taken by this method are furthermore fixed related to the performing frequency of the PMUT array:

$$dt_{solver} = \frac{1}{64 \cdot f_0}. \tag{4.34}$$

Attaching the time step to the acoustic excitation frequency provides a smoother convergence plot with a fixed reciprocal step size. This ensures a divergent and stable output.

Automatic Remeshing is a study solver attribute that remeshes between solver time steps when the mesh quality is unsatisfactory and the remeshing condition is met. This attribute is used in conjunction with the *Moving Mesh* to provide competent mesh quality. The triggering condition used for automatic remeshing is called *Distortion condition*.

For small distortions, such as the neural dust piezoelectric displacement, the following approximation condition is used [16]:

$$\boldsymbol{I_1}(\boldsymbol{E_{iso}}) \simeq \sum_{i<j} \frac{1}{n}(\varepsilon_i - \varepsilon_j)^2 + 2\varepsilon_i j^2 > c \tag{4.35}$$

where $\boldsymbol{I_1}(\boldsymbol{E_{iso}})$ is the first invariant of the isochoric (preserved volume) Green-Lagrange strain tensor, n is the space dimension and c is the remeshing condition limit. For the proposed model, a default value of two is used for this attribute ($c = 2$) When this limit is exceeded, the solution is stopped before the next time step calculation start, and the whole geometry is remeshed. At the end of the simulation, a *Remeshed Solution* is added for every study step that utilizes automatic remeshing.

5 | Computation of Action Potential Through the Backscattered Echo

5.1. Methodology

The following complete procedure is used to process the ultrasonic backscattering data:

1. Excitation signal generation
2. Reception of the acoustic echo on external pMUT Array
3. Calculation of times and voltage values for ultrasound-neural dust interaction
4. Verification of time-of-flight and genuineness of the echo
5. Verification of the neural dust piezoelectric response
6. Isolation of the echo and extracting the electric potential data table
7. Fast Fourier Transform (FFT) and fundamental frequency detection
8. Computation of phase difference and the time delay between the data point and the resting implant potential V_{rest}^{neuron}
9. Calculation of final voltage data point results using the time delays and the piezoelectric response (using either mathematical estimation or calibration)
10. Interpolation of data points and error calculation

The first two steps are discussed comprehensively in Chapter 4. In this chapter, the obtained results and the approach used to transform and process the acquired data are explained. Section 5.2 has the goal of analyzing steps (3-4), while section 5.3 is for step (5). All the other steps used in the method are demonstrated in section 5.4.

5.2. Electric Potential Output

The following output of electric potential values for the external pMUT array is obtained from a point evaluation of (V). The restitution of the result was increased by the number of points solved for in the time domain. All time steps stored by the solver are included as is in the output. Voltage data extraction is done on the middle PMUT, which is visualized in figure 5.1a.

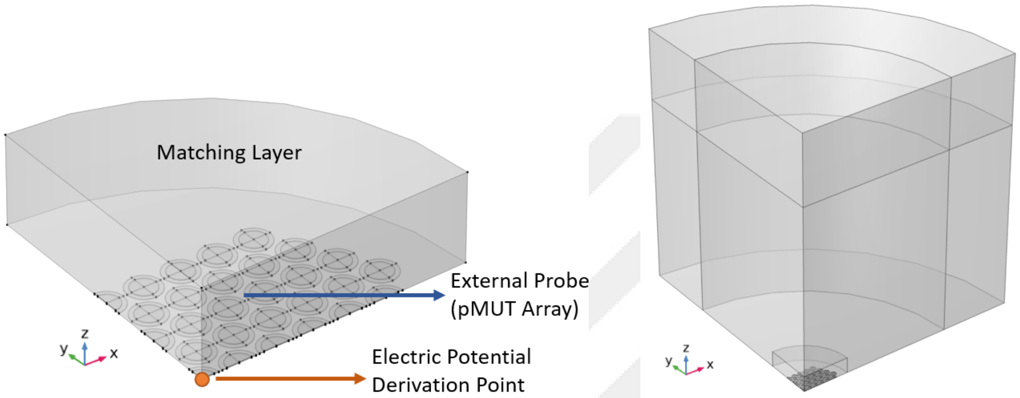

(a) (b)

Figure 5.1: (a) Electric Potential data collection point expressed by the orange dot, with descriptions. (b) Proposed reference model.

The data collection point can be justified by assuming a parallel voltage configuration, which results in an equivalent floating potential output for every singular PMUT device in the external array. This equivalency determines a simplification of result calculation where only the midpoint of the middle PMUT can represent the whole voltage output received by the whole PMUT array.

A reference model devoid of neural dust is created to verify the presence of the acoustic backscattering phenomenon. Without the implant, the backscattering echo is expected to be zero. Then, the floating potential obtained when the neural dust is at resting potential $V_{rest}^{neuron} = -70mV$ is compared with the reference values on plot 5.2.

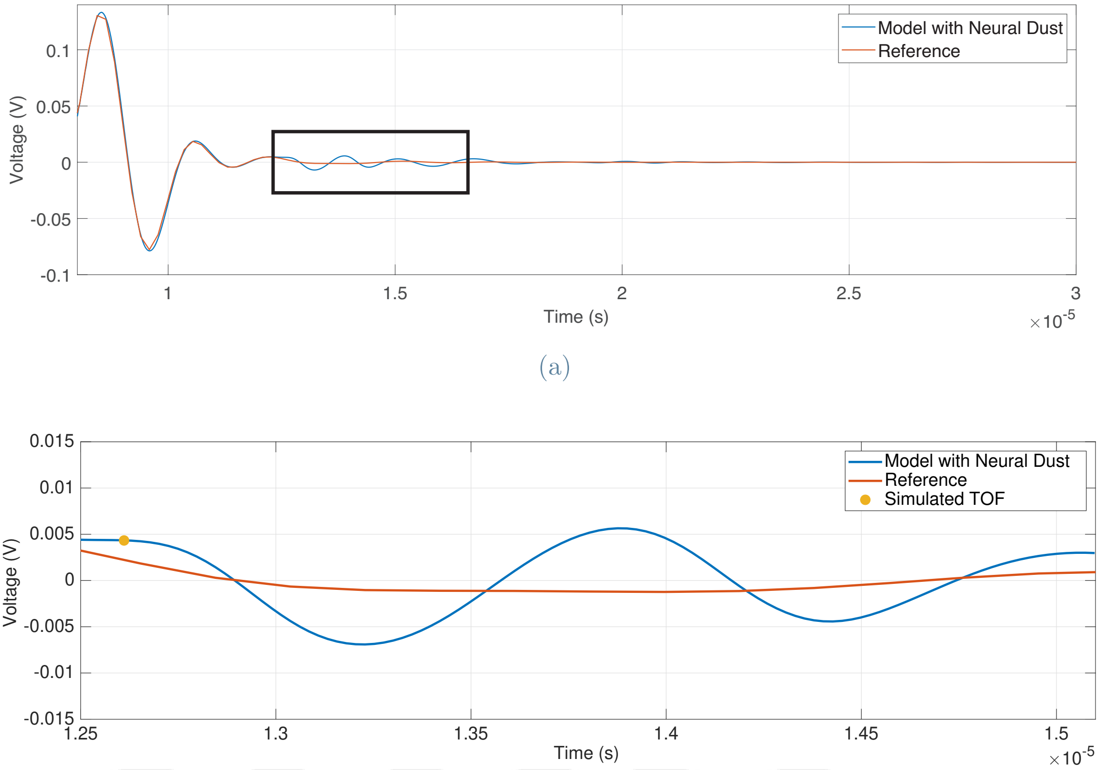

(a)

(b)

Figure 5.2: (a) Electric potential output from the PMUT array of the reference model and the resting potential model $V_{rest}^{neuron} = -70mV$. The black rectangle denotes the echo region. (b) Electric potential output magnified around the echo region. Simulated time-of-flight is expressed as an orange point.

The complete data collection graph in figure 5.2a consists of two distinct sections. An initial damped oscillation is present due to the excitation wave generation, which takes place just before the reception phase. This residual mechanical response relationship is confirmed by comparing the reference and neural dust responses. Since this section follows the exact same path for both of the models, this section can be assumed to be the non-reactive part. The second section that differentiates the neural dust study from reference one, is regarded as the ultrasonic backscattering echo as a result of acoustic-implant interaction. This time span is tentatively referred as the *"echo region"* and plotted on figure 5.2b. After the visual confirmation for the echo has been made, the verification of simulated time-of-flight values is done using the electric potential data difference between the reference model and the neural dust model. The reference model is expected to contain zero scattering acoustic waves so that the data deviation between models is expected to refer to the echo. The theoretical values for the time-of-flight, on the other hand, are calculated using the following formula:

$$t_{TOF} = 2 * d/c_0 \tag{5.1}$$

where d is the penetration depth (distance between the neural dust and PMUT array) and c_0 is the speed of sound in the tissue medium. Final results for theoretical and simulation time-of-flight values are given in table 5.1.

Theoretical TOF	**Simulated TOF**	**Error Rate**
1.2454e-5 s	1.2611e-5 s	1.26%

Table 5.1: Theoretical vs Simulated Time-of-flight values and the Error Rate

The confirmation that the echo is only present in the model with neural dust, and accurate time-of-flight simulation results verifies that the echo is formed through the acoustic backscattering phenomenon. This affirmation was possible by running both simulations based on three cascading studies, as explored in section 4.3.5. However, in these studies, the load on the implant is nearly fixed on $V_{segment} = V^{neuron}_{rest} = -70mV$ and assumed as unchanging with time. The resulting time-of-flight values of the scattered ultrasonic waves are a crucial part of constructing the data points in the proposed model. From this point on, the echo shown in figure 5.2b is assumed to be credible, and authentically the result of the acoustic interaction between the neural dust and the ultrasonic excitation waves.

Study segments and their related voltage values

Every transmission/reception cycle demonstrated in figure 4.5 and table 4.2 is capable of collecting only one data point. Multiple study cycles are needed to accurately depict the action potential of a neuron. There is a big disparity between the wave periods of the neural dust input voltage ($T^{neuron}_0 = 4ms$) and the PMUT array input voltage ($T^{array}_0 = 1.5337\mu s$). Given that the total study time for all three cascading study steps is $t_{final} = 20 * T^{array}_0 = 30.675\mu s$ as depicted in table 4.9, a maximum total of *130* studies are possible in the span of one action potential cycle. However, not all of the studies are essential to the final reconstruction of the action potential; only a handful of studies are necessary to gather enough data points. This also results in a ramp-like action potential voltage behavior during the whole time span of every study. Each of these studies, tentatively referred to as *study segments*, are relating to a starting voltage $V_{segment}$ and a corresponding starting time value $t_{segment}$. These voltage and time values are related to the implant input voltage points V^{neuron} at the beginning of each study segment, which can be mathematically expressed as:

$$V^{neuron}(t_{segment}) = V_{segment}. \tag{5.2}$$

As an example of a study segment, the previously discussed resting potential study for $V_{segment} = V_{rest}^{neuron} = -70mV$ can be characterized as in figure 5.3.

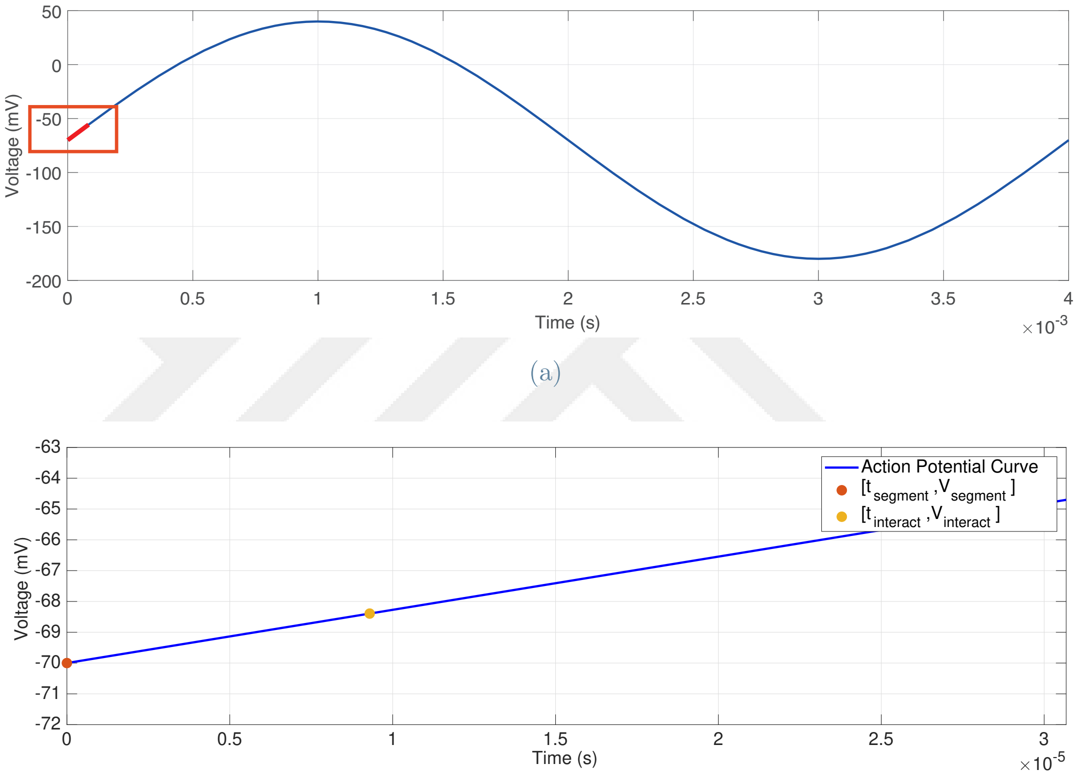

(a)

(b)

Figure 5.3: (a) The whole span of the study segment for $V_{segment} = -70mV$, shown as a red line, with respect to the total cycle of action potential. (b) The close-up of the implant input voltage for the complete study segment ($t = [0, t_{final}]$). The data points discussed are also represented: $[t_{segment}, V_{segment}]$ as the red point and $[t_{interact}, V_{interact}]$ as the orange point.

Furthermore, the interaction time $t_{interact}$ and their related implant voltage points $V_{interact}$ are defined as the exact time and implant voltage values at interaction between the ultrasonic wave and the neural dust. These values are intended to embody the values at the beginning of the scattering phenomenon. The interaction time for acoustic backscattering can trivially be calculated using the time-of-flight t_{TOF} and the time of the transmission study step $t_{transmit}$ as:

$$t_{interact} = t_{segment} + t_{transmit} + t_{TOF}, \tag{5.3}$$

$$V^{neuron}(t_{interact}) = V_{interact}. \tag{5.4}$$

$V_{interact}$ is suitable for calculating the error between the input implant voltage and the obtained data points. Voltage error results are only useful as a validation point for the effectiveness of the proposed simulation. Since it is impossible to gather the value of $V_{interact}$ in a real-world application, this error calculation method is purely based on the numerical computation. However, $t_{interact}$ is a fundamental value for all study segments, where it corresponds to the time variable for every output data point. To gather different data points, implant voltage is shifted as presented in figure 5.4 and the simulation is run starting from the time stamp $t = 0$ using different study segments. This shifting imposes the electric potential boundary condition on the neural dust as $V = V_{interact}$ but transforms the starting time of the study to $t = 0$. As a result, every simulated segment and their corresponding values may be summarized as in table 5.2.

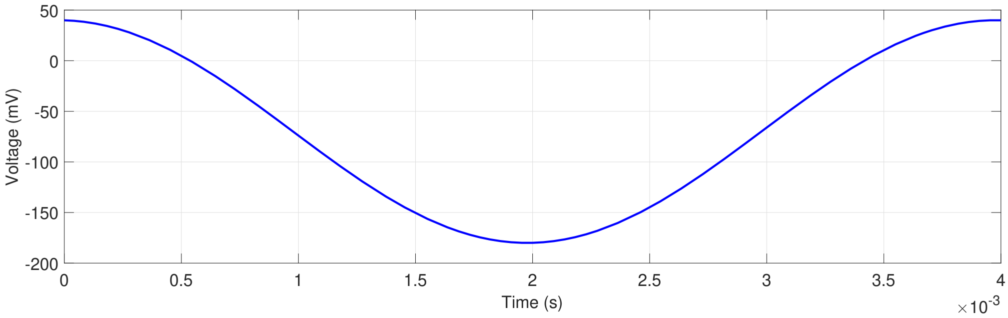

Figure 5.4: Shifted implant voltage for ($t_{segment} = 1.0123ms$, $V_{segment} = 40mV$).

$V_{segment}$	$V_{interact}[mV]$	$t_{interact}$[s]
$-70mV$	-68.394	9.2944e-6
$+40mV$	39.937	1.0216e-3
$-180mV$	-179.97	3.0154e-3
$-15mV$	-13.01	3.4672e-4
$-125mV$	-126.08	2.3406e-3

Table 5.2: Real implant voltage points and time stamps for acoustic-implant interaction

Acoustic backscattering echo results for different study segments

Different prescribed implant voltage values $V_{interact}$ create diverse echo outcomes as previously anticipated. Different segment studies are simulated for various implant voltage functions $V^{neuron}(t = 0) = V_{segment}$. The variation in TOF values is then collected and used as discrete data points. Final voltage output results for different $V_{segment}$ studies that span the whole wavelength of the implant input function are plotted in figure 5.5.

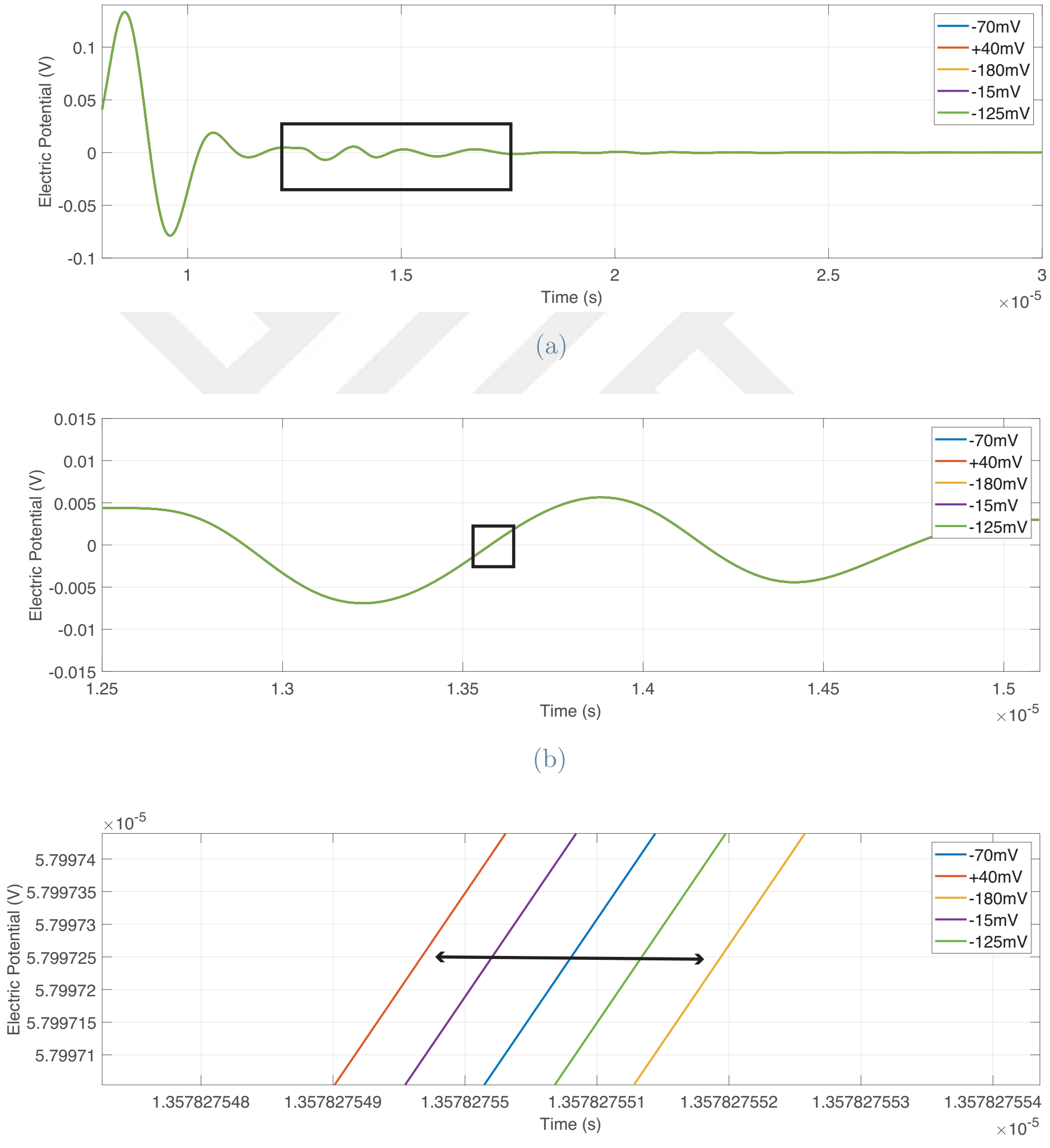

(a)

(b)

(c)

Figure 5.5: (a) Full range of the voltage output graph, collected by the external PMUT Array. (b) Backscattered echo portion of the voltage output graph. (c) Magnified plot near the midpoint of the echo. The arrow represents the equidistant spreading of different segments in terms of time of flight values.

The mechanical displacement observed due to the piezoelectric effect changes the distance between the neural dust and the external PMUT array. This in turn creates variance in TOF values between different study segments. Thus, the TOF and the implant input voltage are directly related through the mechanical deformation of the piezoelectric material. The piezoelectric coupling suggests that the positive implant voltages (like $V_{segment} = +40mV$) need to create tensile deformation of PZT, while negative values should enforce compressive response, as discussed in section 1.2. This response is higher concerning the voltage value, hence the maximum and minimum time-of-flight values must correspond to the peak values of the action potential curve, which are $V_{segment} = +40mV$ and $V_{segment} = -180mV$. All the intermediary data point segments, namely, $(V_{segment} = -15mV, -70mV, -125mV)$ are expected to respond linearly in between these peak studies, in terms of both the neural dust implant response and the time of flight difference. Preliminary observation suggests that all of the above criteria are met, and the proposed simulation is anticipated to return proper output data point results.

5.3. Implant Piezoelectric Response Verification

The piezoelectric response of neural dust bulk PZT is studied to verify the stability and linear mechanical response of the neural dust module. An accurate response is needed to have distinct time-of-flight differences in the output backscattering echo. For the neural dust mechanical deformation output, the following data derivation point is used:

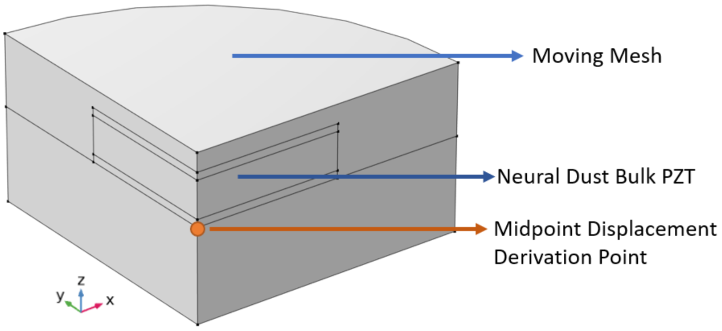

Figure 5.6: Implant deformation data collection point shown as an orange dot, with descriptions.

The selected point is the midpoint in the interface surface of the top electrode with the tissue phantom, where the interaction between the ultrasonic wave and the neural dust occurs. This derivation point is utilized to acquire the implant deformation values in the z-direction, tentatively referred to in this thesis as the *implant midpoint displacement*. Displacement for each $V_{segment}$ study is visualized on figure 5.7.

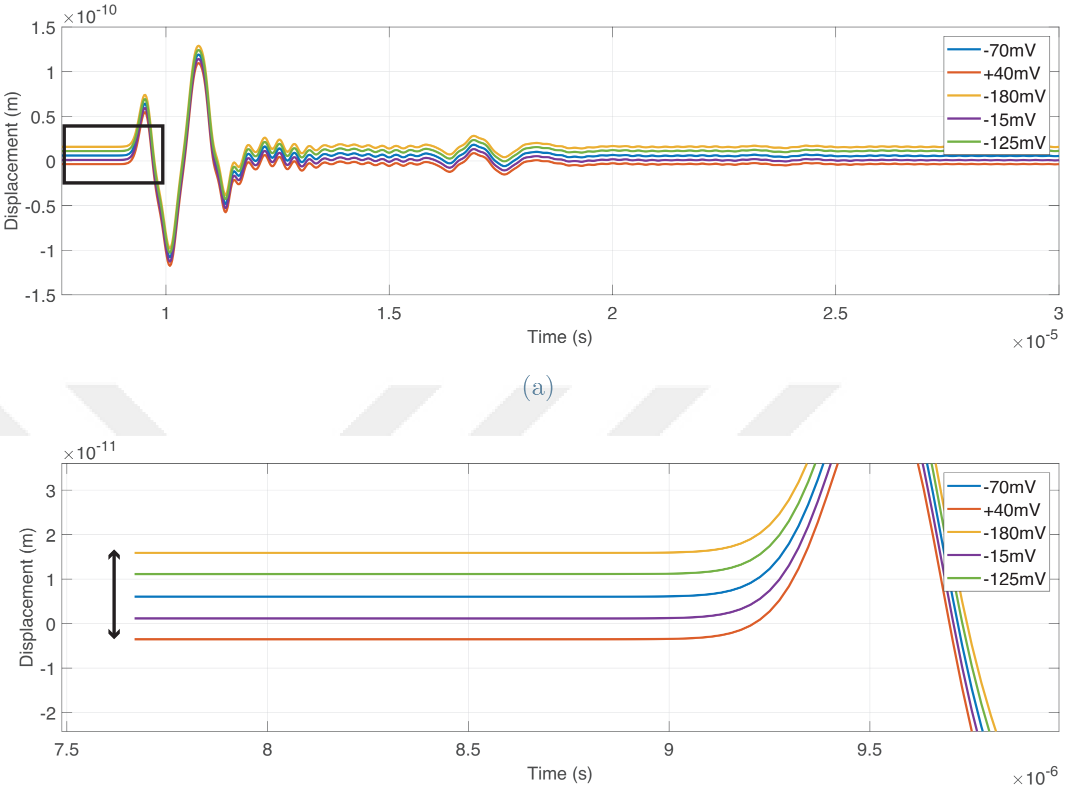

(a)

(b)

Figure 5.7: (a) Transversal implant midpoint displacement plot for different data point segments. (b) Magnified view of the black rectangle from *fig. (a)*, representing data collection origin values. The arrow shows the equidistant spreading of different segments in terms of static transversal displacement values. This equivalency confirms linear electromechanical response.

In figure 5.7a, the neural dust bulk PZT exhibits a proportionate response to the acoustic interaction and settles back linearly to its expected value. This proportionality is required for a precise time-of-flight readout and is an essential part of this study's premise. Before the intercommunication between the neural dust and the acoustic wave, the midpoint deformation has a static-like behavior due to the negligible voltage differences during the study period. In this region, observed mechanical response values (presented by the transversal midpoint displacement in figure 5.7a) are only due to the implant input voltage, moving freely under a single driving force. Whereas after this zone (after around $t = 9e - 6s$), the displacement is influenced by the arriving acoustic wave. The static region observed in figure 5.7b shows a linear electromechanical pattern, which is the predicted outcome. During the sound wave interaction period ($t > 9e-6s$), applied pressure on the acoustic-structure boundary creates a responsive damped oscillation on the neural dust. A sinusoidal displacement can be observed at $t = [8 - 13\ \mu s]$, and an echo at $t = 3 * t_{TOF}$ or $t = [16 - 18\ \mu s]$. This echo represents an ultrasonic wave that scattered twice, both on neural dust and the PMUT array, and finally propagated back to the neural dust. Both of these signals also exhibit linear piezoelectric behavior in terms of different $V_{segment}$ values. During the following calculations of this work, the transversal midpoint displacement at the end of the first static zone is used for the computation of the TOF values, as it represents the genuine displacement that is related to the action potential of the nerve.

The neural dust module is immersed in various matching layer materials throughout the research, and the midpoint displacement of each of them gives us insight into the piezoelectric response under different medium conditions during the same implant voltage value $V_{segment}$. This output is plotted in figure 5.8. Here, neural dust exhibits completely different responses to the acoustic wave interaction as expected, while settling back to an equivalent quasi-equilibrium (static) value on each medium. This equivalency may be regarded as proof of the stability of the model.

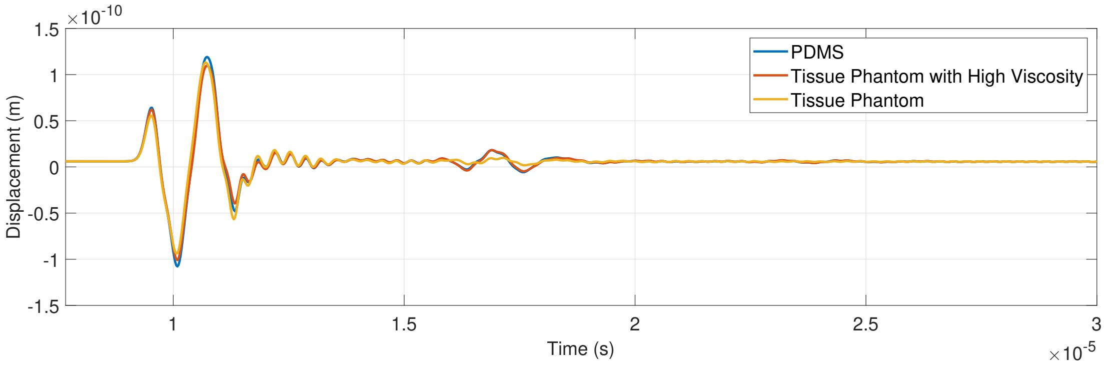

Figure 5.8: Transversal implant displacement plot where neural dust is immersed into different materials, with implant resting voltage of $V_{segment} = -70mV$.

Due to its confirmed stability and piezoelectric response linearity, this neural dust module can be safely used in the proposed model. The heterogeneous nature of the metabolism demands a stable displacement output in every type of medium, and the equivalent static value means only a singular piezoelectric material study is needed to ascertain the piezoelectric coupling between the mechanical displacement and electrical voltage. Since the quasi-equilibrium values mentioned above are exactly the same, the mechanical piezoelectric material response to any input voltage can be estimated by doing proper characterization before device usage. This characterization may either be done experimentally or as a computational simulation. An example of a required mechanical response graph is studied by Mao et al [36]. This study focuses on both a numerical and a computational characterization method for piezoelectric ceramics, which can easily be adapted to the bulk PZT material used on neural dust in the proposed model.

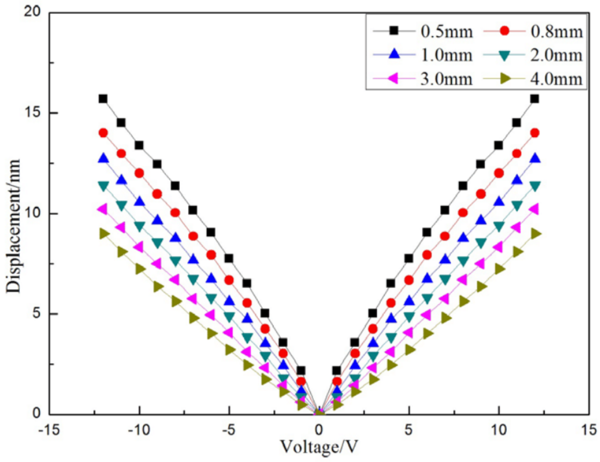

Figure 5.9: An example characterization study plot for piezoelectric ceramic transducers. [36]

5.4. Post-processing Method and Final Output

In this section, the methods used to process the acquired echo signals are discussed. Interpolated final graphs and error rates are also reviewed.

Fast Fourier Transform (FFT)

FFT is a signal processing tool that is used to describe the relationship between the time domain and frequency domain of a discrete waveform. It is a computationally faster Discrete Fourier Transform method. The main goal of FFT is identifying and separating the sinusoidal wave content (their amplitudes and phases) from any arbitrary waveform. This correlation can mathematically be described as:

$$S(f) = \int_{-\inf}^{\inf} s(t)e^{-i2\pi ft}\,dt \tag{5.5}$$

where $s(t)$ is the signal in time domain, i is the imaginary number and $S(f)$ is the transformed signal in frequency domain[9]. In MATLAB, Fast Fourier Transform results in a one-dimensional array of complex numbers. As these numbers act as vectors in the complex space, each complex number contains the magnitude and phase angle of its specific frequency. As an example, the graphs regarding the magnitude content and phase content of collected backscattering echo with input neural dust potential $V_{segment} = -70mV$ are shown in figure 5.10.

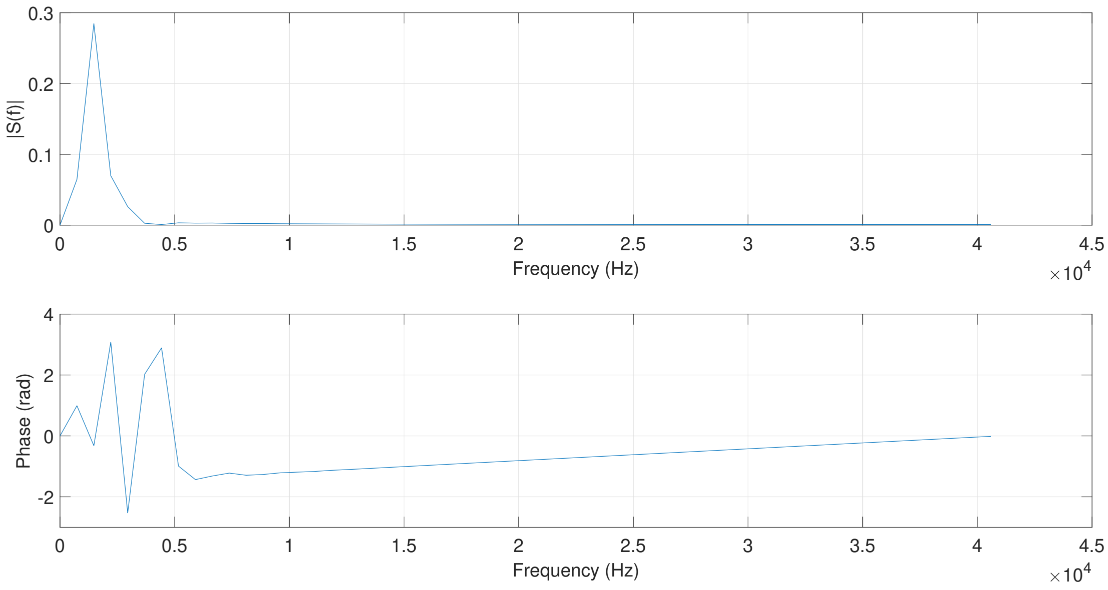

Figure 5.10: Magnitude (top) and phase (bottom) content of each sinusoidal frequency, for echo output in the resting potential study $V_{segment} = -70mV$.

In the proposed methodology, the Fourier Transform is applied in order to compute phase lag. The frequency with the maximum magnitude response is designated as the *fundamental frequency* for the echo. The phase angle difference between two output echo signals at this fundamental frequency is then subtracted to find the phase difference/lag for each data point study:

$$\Delta\theta = \theta_i(max|S_i(f)|) - \theta_j(max|S_j(f)|) \tag{5.6}$$

where $\Delta\theta$ is the phase lag and θ is the phase angle for two echo outputs i and j. The *reference echo* model is appointed to be the resting potential one ($V_{segment} = -70mV$). Every other data segment is compared with this reference echo model to acquire phase lag results. These results are summarized in table 5.3.

Time-of-flight difference and final data point calculations

The difference in time-of-flight values, represented in figure 5.5c, is directly linked to the phase lag through the following formula:

$$\Delta t_{TOF}[s] = \frac{\Delta\theta[Rad]}{2 * \pi * f_0[s^{-1}]}. \tag{5.7}$$

As discussed in section 5.3, a characterization of piezoelectric material is needed to relate the time-of-flight difference to a voltage value. This can normally be done using experimental methods and is only related to the device geometry and some material properties (like piezoelectric coupling parameters discussed in section 1.2). For the sake of this thesis, the linearity in electromechanical response between the input voltage and mechanical displacement is assumed through the equidistant spreading shown in figure 5.7b. This piezoelectric response value is represented by a characteristic value for neural dust δ_{neural}, and characterized as the amount of transversal implant displacement per input implant voltage $[m/mV]$. Since t_{TOF} may directly be correlated with the neural dust transversal displacement, and piezoelectric response in known through the sensitivity $\delta_{neural}[m/mV]$, the output voltage values V_{output} can be computed and summarized as in figure 5.11 and table 5.3.

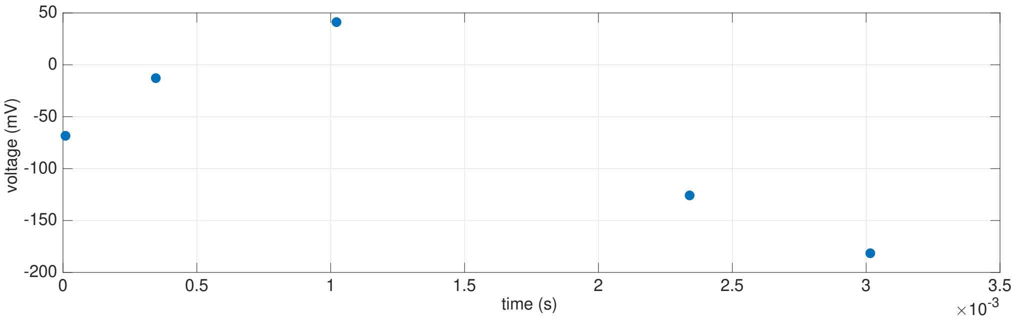

Figure 5.11: Final output data points for all simulated study segments.

$V_{segment}$	$\Delta\theta[Rad]$	$\Delta t_{TOF}[s]$	$V_{output}[mV]$
$-70mV$	-	-	-68.394
$+40mV$	4.838e-08	1.2184e-14	41.1657
$-180mV$	-4.997e-08	-1.2584e-14	-181.5494
$-15mV$	2.454e-08	6.1819e-15	-12.8079
$-125mV$	-2.536e-08	-6.3878e-15	-125.8318

Table 5.3: Phase lag, time-of-flight difference and final output voltage values

Symmetry Data Points

Sinusoidal approximation of neuron action potential has a natural outcome of data points that share the same input $V_{interact}$ and a related equal V^{output}. These equivalent data points, which can be called symmetry data points, are used to extend the simulation. Simulated data points and their respective symmetry points are plotted in figure 5.12.

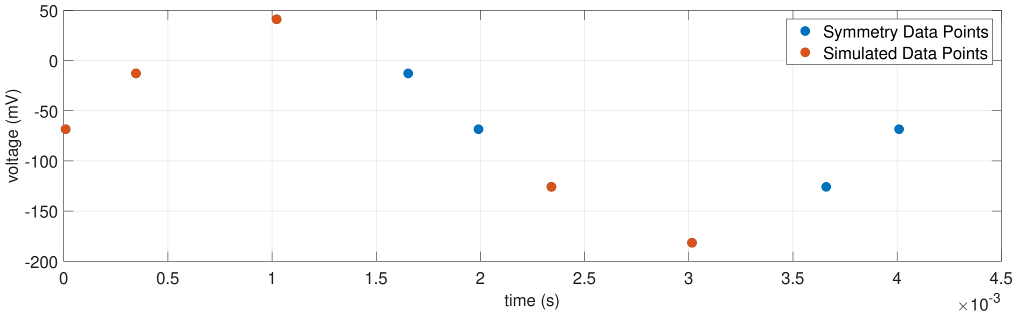

Figure 5.12: Final data points and their symmetry pairs.

The timestamp for the symmetry data is found using a geometrical symmetry method, which can mathematically be summarized by the following notation (5.8):

$$\begin{cases} t = t_{interact} \implies t = \dfrac{T_0^{neuron}}{2} - t_{interact} \quad , for\ t_{interact} < \dfrac{T_0^{neuron}}{2} & \text{(5.8a)} \\ t = t_{interact} \implies t = \dfrac{3 * T_0^{neuron}}{2} - t_{interact} \quad , for\ t_{interact} > \dfrac{T_0^{neuron}}{2}. & \text{(5.8b)} \end{cases}$$

Using the aforementioned procedure, symmetry data points are calculated and the final nine-point output data is collected in table 5.4.

$V_{segment}$	$V_{interact}[mV]$	$V_{output}[mV]$	Error Rate [%]	$t_{interact}[s]$
$-70mV$	-68.394	-	0	9.2944e-6, 1.99e-3, 4.009e-3
$+40mV$	39.937	41.1657	3.08	1.0216e-3
$-180mV$	-179.97	-181.5494	0.88	3.0154e-3
$-15mV$	-13.01	-12.8079	1.55	3.4672e-4, 1.6533e-3
$-125mV$	-126.08	-125.8318	0.2	2.3406e-3, 3.6594e-3

Table 5.4: Interaction and output voltages, the error rates and interaction times.

The error rates for each segment are highly satisfactory as all of them are below 5% mark. For the overall measurement of the action potential, two data points can be marked as the most significant output: two peaks at maxima $V_{segment} = +40mV$ and minima $V_{segment} = -180mV$. These results are decidedly unique by not having any symmetry data points. Hence, the action potential behavior can immediately be recognized when these voltages V_{output} are present as a result of a study segment. After enough data pairs $[t_{interact}, V_{output}]$ are gathered, a nonlinear interpolation scheme, namely the *cubic spline method* is chosen to finalize the output. Interpolated results are given as figure 5.13.

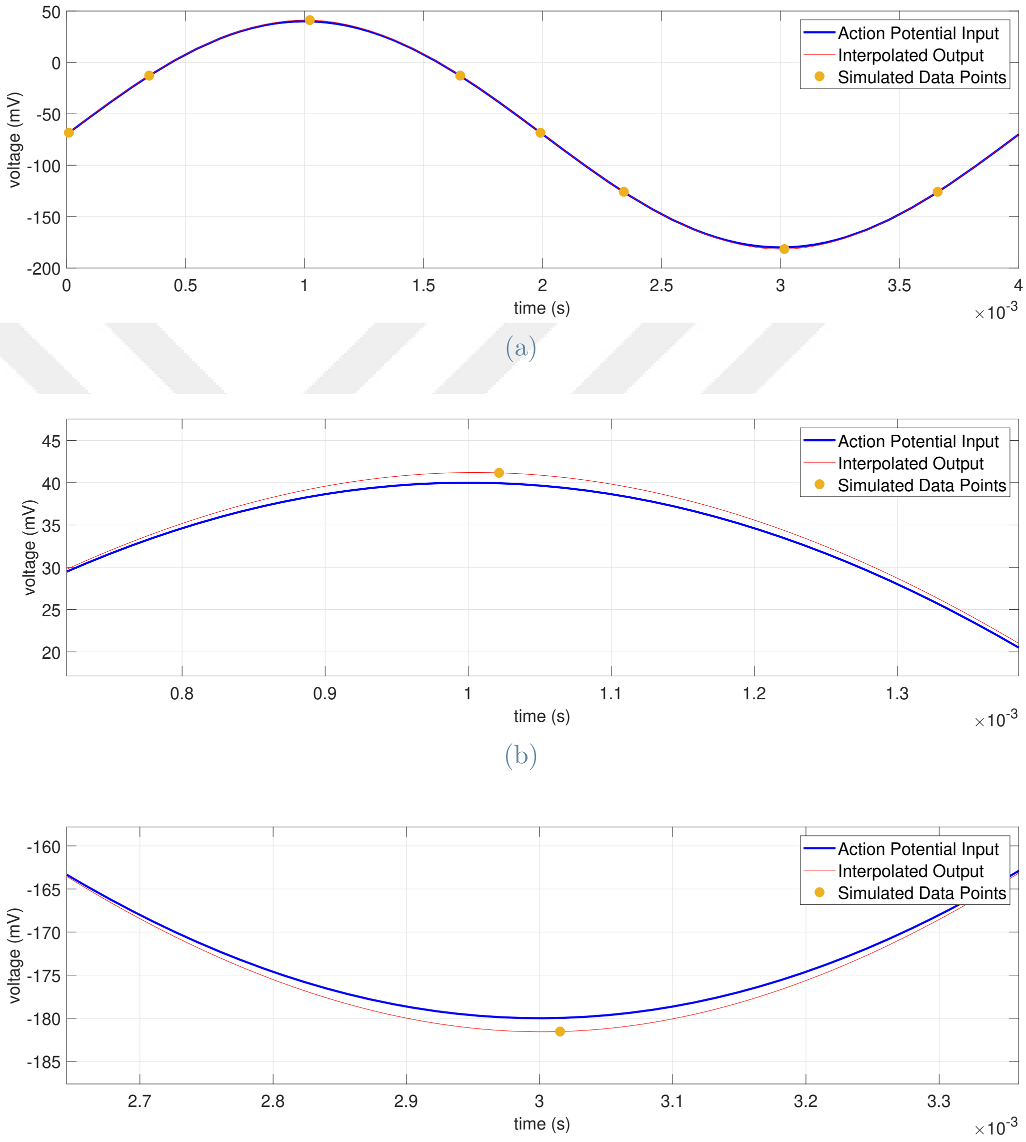

(a)

(b)

(c)

Figure 5.13: (a) Graph containing the action potential input, output data points, and interpolated final output. (b) Magnified graph with the focus around ($V^{neuron} = 40mV$). (c) Magnified graph with the focus around ($V^{neuron} = -180mV$).

6 | Conclusions and future developments

This study proposed an approach to unidirectional communication from an implant to an external probe. The communication data is selected to be the recordings of a nerve. Hence, the main goal was to recreate this neural voltage plot from the data points extracted by the acoustic backscattering phenomenon. A COMSOL Multiphysics model is then suggested to achieve this flow of data, containing three main components: an IMD, an external PMUT array, and the tissue medium. The implant, more specifically a neural dust mote, is designed and immersed in a tissue phantom. The communication module in IMD is created as bulk PZT material sandwiched between two electrodes, where the neuron is directly connected. The voltage difference between these two electrodes is expected to change when the neural electrochemical data delivery process called an *action potential* occurs. This action potential voltage values are approximated as a sinusoidal wave with amplitude $V_{amp}^{neuron} = -110mV$ and frequency $f_{neuron} = 250Hz$, and then applied to the PZT material electrode boundaries. This results in mechanical deformation of PZT, due to the electromechanical coupling provided by the piezoelectric effect.

The external probe is therefore formed as a PMUT array to both create a transmission ultrasonic wave and reception of backscattering echo. A custom PMUT array design provided by STMicroelectronics is used with a proprietary PZT material. This piezoelectric configuration is then supplied with a sinusoidal voltage excitation cycle, with amplitude $V_{AC}^{array} = 5V$ and frequency $f_0^{array} = 652kHz$. The generated acoustic wave is expected to travel through the medium and scatter around when it interacts with the implant. Some of these scattered waves are thus anticipated to return to the external PMUT array. The duration between the excitation and recollection of the echo is called the time of flight (TOF). This TOF value is used to gain insight into the piezoelectric material deformation occurring in the implant. The compressive and tensile mechanical strains are predicted to appear linearly in relation to the voltage supplied by the neuron. The implant deformation changes the distance between the PMUT array and the neural dust, thus different TOF values are expected. These TOF values are then studied between different implant input voltages and transformed into final data points. Interpolation of these final data points is expected to create a solution that is similar to the neural voltage plot.

First, a reference model is created that is devoid of any implant and compared with the reference echo model with an input neural dust voltage of $V^{neuron} = -70mV$. The purpose of this comparison was to assess the genuineness of the echo, and whether or not this echo is truly observed through the acoustic backscattering. The legitimacy of the observed acoustic wave is confirmed by the absence of an acoustic echo in the reference model. The simulated TOF value is also calculated as $1.2611e - 5s$ by subtracting the reference model values from the reference echo.

Second of all, the mechanical deformation of the implant is studied. It is seen that when the IMD module is immersed in various mediums, the displacement of the bulk PZT is exactly the same until acoustic-implant interaction occurs. This confirmed the stability of the neural dust module. The neural dust response is then analyzed between different data point segments, and the electromechanical linearity of the bulk PZT material response is established.

Consequently, studies between different data points that span the whole neural dust implant response are made. The acoustic echoes and their related phase values are computed. The phase lag between the reference echo for $V^{neuron} = -70mV$ and the studied echo is calculated and the time of flight differences are derived. These TOF differences are then transformed into data point voltage values using the material response characterization data. Time-steps of the data points are gathered through a mathematical estimation of the scattering interaction between the implant and the ultrasonic wave. Finally, all of the collected data points are interpolated using the cubic spline interpolation method. The final output data is plotted and compared with the input action potential of a neuron. It is concluded that the error for simulated data points has an error rate of less than 4% and the output interpolated plot is strikingly similar to the input sinusoidal wave.

The presented ultrasonic backscattering method for intrabody communications shows promising results that can prompt future work to further realize the usage of ultrasound for IMDs. Possible experimentation and in vivo testing may invigorate the development of this technology. However, two main drawbacks need to be addressed before the proper implementation of this method:

- *Implant-PMUT array alignment angle:* In the proposed simulation model, the implant and the external PMUT array are perfectly aligned (alignment angle: 180°). Complex systems like the human metabolism inherently cause misaligned systems, which may cause a further increase in error.

- *Penetration Depth:* Ultrasound attenuation is innately high in tissues. The distance between the neural dust and PMUT array in the model is fixed at $5mm$. Implementing this method in a deeper communication length that also changes values between data points may cause the whole system to malfunction. Further development in the electronic integrated circuit design is needed to properly modulate and post-process the backscattering data.

Changing the industrial field that this communication method focuses on may also alleviate some of these problems. Due to its fixed penetration depth and the possibility of better alignment, this technique may also be used as a range finder application.

Bibliography

[1] T. Agarwal. Piezoelectric effect: Inverse Piezoelectric-Effect and its applications, Mar. 2019.

[2] J. R. Allegra and S. A. Hawley. Attenuation of sound in suspensions and emulsions: Theory and experiments. *J. Acoust. Soc. Am.*, 51(5B):1545–1564, May 1972.

[3] O. H. Ando Junior, M. A. Coelho, C. F. Malfatti, and V. J. Brusamarello. Proposal of a micro generator piezoelectric for portable devices from the energy harvesting. *Renew. Energy Power Qual. J.*, pages 656–660, Apr. 2014.

[4] Balmes, Bianchi, V. des Roches, and Martin. Basics of piezoelectricity, 2018. Accessed: 2022-11-7.

[5] A. Bayliss, M. Gunzburger, and E. Turkel. Boundary conditions for the numerical solution of elliptic equations in exterior regions. *SIAM J. Appl. Math.*, 42(2):430–451, Apr. 1982.

[6] J.-P. Berenger. A perfectly matched layer for the absorption of electromagnetic waves. *J. Comput. Phys.*, 114(2):185–200, Oct. 1994.

[7] D. T. Blackstock. Fundamentals of physical acoustics. *J. Acoust. Soc. Am.*, 109(4): 1274–1276, Apr. 2001.

[8] R. Bogue. MEMS sensors: past, present and future. *Sens. Rev.*, 27(1):7–13, Jan. 2007.

[9] E. O. Brigham and R. E. Morrow. The fast fourier transform. *IEEE Spectrum*, 4 (12):63–70, Dec. 1967.

[10] S. Carrara. Body dust: Well beyond wearable and implantable sensors. *IEEE Sens. J.*, 21(11):12398–12406, June 2021.

[11] M. Casini. Advanced materials for architecture. In *Smart Buildings*, pages 55–104. Elsevier, 2016.

[12] Y.-Q. Chen, Y.-X. Li, Y. Chen, Z.-Y. Ju, L.-Q. Tao, Y. Pang, Y. Yang, and T.-L. Ren. Large-Scale and High-Density pMUT array based on isolated Sol-Gel PZT membranes for fingerprint imaging. *J. Electrochem. Soc.*, 164(7):B377, May 2017.

[13] D. K. Cheng and D. K. Cheng. *Field and Wave Electromagnetics*. Addison-Wesley Pub., 1989.

[14] J. Chung and G. M. Hulbert. A time integration algorithm for structural dynamics with improved numerical dissipation: The Generalized-α method, 1993.

[15] M. Cohen. Silent boundary for transient analysis. *Computational Methods for Transient Analysis*, pages 301–360, 1983.

[16] S. COMSOL AB Stockholm. Comsol multiphysics reference manual: Version 6.0, 2021.

[17] G. Cronin. MEMS sensors are coming to industrial applications. `https://blog.st.com/mems-sensors-are-coming-to-industrial-applications/`, Nov. 2018. Accessed: 2022-11-24.

[18] R. S. Dahiya and M. Valle. *Robotic Tactile Sensing*. Springer Netherlands, 2013.

[19] S. Datta. Piezoelectric materials: Crystal orientation and poling direction, Feb. 2014. Accessed: 2022-11-8.

[20] A. De Ninno, A. Gerardino, B. Girarda, G. Grenci, and L. Businaro. Top-Down approach to nanotechnology for cell-on-chip applications. *CIS-BBL*, 3(2), Aug. 2010.

[21] M. A. Diaz, M. A. Solovchuk, and T. W. H. Sheu. A conservative numerical scheme for modeling nonlinear acoustic propagation in thermoviscous homogeneous media. *J. Comput. Phys.*, 363:200–230, June 2018.

[22] J. J. Faran. Sound scattering by solid cylinders and spheres. *J. Acoust. Soc. Am.*, 23(4):405–418, July 1951.

[23] Y.-C. Fung. *Foundations of Solid Mechanics*. Prentice-Hall, 1965.

[24] L. Galluccio, T. Melodia, S. Palazzo, and G. E. Santagati. Challenges and implications of using ultrasonic communications in intra-body area networks. In *2012 9th Annual Conference on Wireless On-Demand Network Systems and Services (WONS)*, pages 182–189, Jan. 2012.

[25] A. E. Hay and D. G. Mercer. On the theory of sound scattering and viscous absorption in aqueous suspensions at medium and short wavelengths. *J. Acoust. Soc. Am.*, 78 (5):1761–1771, Nov. 1985.

[26] T. Ikeda. *Fundamentals of Piezoelectricity.* Oxford University Press, 1996.

[27] B. Jaafar, J. A. Neasham, and P. Degenaar. What is ultrasound can and cannot do in the communication of biomedical implanted medical devices. *IEEE Rev. Biomed. Eng.*, PP, May 2021.

[28] J.-M. Jin. *The Finite Element Method in Electromagnetics.* John Wiley & Sons, Feb. 2015.

[29] Y.-H. Joung. Development of implantable medical devices: from an engineering perspective. *Int. Neurourol. J.*, 17(3):98–106, Sept. 2013.

[30] L. Li, J. Xu, J. Liu, and F. Gao. Recent progress on piezoelectric energy harvesting: structures and materials. *Advanced Composites and Hybrid Materials*, 1(3):478–505, Sept. 2018.

[31] D. R. Lide. *CRC Handbook of Chemistry and Physics, 85th Edition.* CRC Press, June 2004.

[32] H. Liu, J. Geng, Q. Zhu, L. Zhang, F. Wang, T. Chen, and L. Sun. Flexible ultrasonic transducer array with bulk PZT for adjuvant treatment of bone injury. *Sensors*, 20 (1), Dec. 2019.

[33] M. Liu and D. G. Gorman. Formulation of rayleigh damping and its extensions. *Comput. Struct.*, 57(2):277–285, Oct. 1995.

[34] M. M. Maharbiz, D. Seo, J. M. Carmena, J. M. Rabaey, and E. Alon. Neural dust: An untethered approach to chronic Brain-Machine interfaces, 2015.

[35] A. Manbachi and R. S. C. Cobbold. Development and application of piezoelectric materials for ultrasound generation and detection. *Ultrasound*, 19(4):187–196, Nov. 2011.

[36] Y. Mao, J. Yang, H. Liu, Y. Liu, and W. Xu. Study on radial vibration of circular piezoelectric ceramic. *J. Phys. Conf. Ser.*, 1187(2):022045, Apr. 2019.

[37] W. P. Mason. Piezoelectricity, its history and applications, 1980.

[38] Medicine LibreTexts. 10.5e: The action potential and propagation. `https://med.libretexts.org/@go/page/7594`, July 2018.

[39] M. Mezher and A. R. AlAbbas. Performance analysis of hard decision and soft decision algorithms over in vivo radio channel, 2022.

[40] K. Nunez. Cochlear implant: Cost, pros, cons, risks, how it works. `https://www.healthline.com/health/cochlear-implant`, Feb. 2022. Accessed: 2022-11-23.

[41] M. Ortiz-Catalan. Ultrasound-powered tiny neural stimulators. *Nat Biomed Eng*, 4 (2):144–145, Feb. 2020.

[42] M. G. Papoutsidakis, C. S. Psomopoulos, G. C. Ioannidis, and D. I. Tseles. Motion sensors and transducers to navigate an intelligent mechatronic platform for outdoor applications. *Sensors & Transducers*, 198(3):16, 2016.

[43] D. K. Piech, B. C. Johnson, K. Shen, M. M. Ghanbari, K. Y. Li, R. M. Neely, J. E. Kay, J. M. Carmena, M. M. Maharbiz, and R. Muller. A wireless millimetre-scale implantable neural stimulator with ultrasonically powered bidirectional communication. *Nat Biomed Eng*, 4(2):207–222, Feb. 2020.

[44] A. D. Pierce. Basic linear acoustics, 2007.

[45] F. Pop, B. Herrera, and M. Rinaldi. Lithium niobate piezoelectric micromachined ultrasonic transducers for high data-rate intrabody communication. *Nat. Commun.*, 13(1):1782, Apr. 2022.

[46] Precedence Research. Implantable medical devices market size, report 2022 to 2030. `https://www.precedenceresearch.com/implantable-medical-devices-market`, 2020.

[47] A. B. Rapeaux and T. G. Constandinou. Implantable brain machine interfaces: first-in-human studies, technology challenges and trends. *Curr. Opin. Biotechnol.*, 72: 102–111, Dec. 2021.

[48] B. M. G. Rosa and G.-Z. Yang. Ultrasound powered implants: Design, performance considerations and simulation results. *Sci. Rep.*, 10(1):6537, Apr. 2020.

[49] D. Rubinetti, D. A. Weiss, E. Weingartner, and M. Lenner. Ultrasound scattering from a rigid sphere using the discontinuous galerkin method in the Time-Explicit domain. *Evaluation*, 1(234):6, 2019.

[50] N. Seckel and A. Singh. Physics of 3d ultrasonic sensors. *Toposens GmbH, Tech. Rep.*, 2019.

[51] D. Seo, J. M. Carmena, J. M. Rabaey, M. M. Maharbiz, and E. Alon. Model validation of untethered, ultrasonic neural dust motes for cortical recording. *J. Neurosci. Methods*, 244:114–122, Apr. 2015.

[52] D. Seo, R. M. Neely, K. Shen, U. Singhal, E. Alon, J. M. Rabaey, J. M. Carmena, and

M. M. Maharbiz. Wireless recording in the peripheral nervous system with ultrasonic neural dust. *Neuron*, 91(3):529–539, Aug. 2016.

[53] Siemens. A lifesaver in a plastic cup: A history of pacemakers at siemens. *International journal of heritage studies*, Oct. 2017.

[54] A. Singer and J. T. Robinson. Wireless power delivery techniques for miniature implantable bioelectronics. *Adv. Healthc. Mater.*, 10(17):e2100664, Sept. 2021.

[55] E. Strickland. 4 steps to dust-size neural implants [news]. *IEEE Spectrum*, 53(11): 14–15, Nov. 2016.

[56] S. Tadigadapa and K. Mateti. Piezoelectric MEMS sensors: state-of-the-art and perspectives. *Meas. Sci. Technol.*, 20(9):092001, July 2009.

[57] R. M. Tayade, B. Doloi, B. R. Sarkar, and B. Bhattacharyya. A state of the art on sequential Micro-Machining. *IOP Conf. Ser.: Mater. Sci. Eng.*, 653(1):012026, Nov. 2019.

[58] A. K. Teshome, B. Kibret, and D. T. H. Lai. A review of implant communication technology in WBAN: Progress and challenges. *IEEE Rev. Biomed. Eng.*, 12:88–99, 2019.

[59] W. J. Tomlinson, S. Banou, C. Yu, M. Stojanovic, and K. R. Chowdhury. Comprehensive survey of galvanic coupling and alternative Intra-Body communication technologies. *IEEE Communications Surveys & Tutorials*, 21(2):1145–1164, 2019.

[60] B. A. Warneke and K. S. J. Pister. An ultra-low energy microcontroller for smart dust wireless sensor networks. In *2004 IEEE International Solid-State Circuits Conference (IEEE Cat. No.04CH37519)*, pages 316–317 Vol.1, Feb. 2004.

[61] R. Weser, S. Wöckel, B. Wessely, and U. Hempel. Particle characterisation in highly concentrated dispersions using ultrasonic backscattering method. *Ultrasonics*, 53(3): 706–716, Mar. 2013.

A | Matlab Code for Interpolation and Acoustic Echo Output Calculations

```
% This MATLAB code is used to compute the output data points using FFT,
% with the calculation methodology explained in Chapter 5 of the thesis.
%
% Created by: Kubilay Kaan Bahceci
% Politecnico di Milano, 24.11.2022
% Clears the previous commands and variables.
clear all
clc
% Loads the acoustic echo outpus one-by-one and calculates data points.
for i=3:6
% Loads model tables and assigns them to a temporary table.
tempmodel1=load('FinalModel_PDMS_echo_V.txt'); % Inputs the file name.
t = tempmodel1(:,1); % First row is always the time variable.
x = tempmodel1(:,2); % Second row is the reference echo voltage (-70mV)
y = tempmodel1(:,i); % Electric potential for the compared segment.
% Removes bias (mean voltage amplitude variations for the two echo).
f0 = 652000; % Sets performing frequency of the PMUT array.
x = x - mean(x); % Eliminates the DC voltage for reference echo.
y = y - mean(y); % Eliminates the DC voltage for compared echo.
% Utilizes Fast Fourier Transform (FFT).
X=fft(x);
Y=fft(y);
% Determines the frequency value for maximum magnitude response.
[mag_x, idx_x] = max(abs(X)); % This frequency value is often called
[mag_y, idx_y] = max(abs(Y)); % the fundamental frequency.
% Computes time-of-flight difference between the two echoes.
px = angle(X(idx_x)); % Phase angle of reference and compared echo
py = angle(Y(idx_y)); % output for fundamental frequency.
phase_lag(i) = py - px; % Phase lag is the difference of phase angles.
```

```
tof_diff(i) = phase_lag(i)/(2*pi*f0); % TOF difference is calculated.
% Determines the amplitude ratio at fundamental frequency.
amplitude_ratio = mag_y/mag_x;
% Displays the phase lag and TOF difference on command window
disp(['Phase lag Y->(-70mV) = ' num2str(phase_lag) ' rad'])
disp(['TOF difference Y->(-70mV) = ' num2str(tof_diff) ' s'])
% Final output data calculation
perMV = 1.1121357*10^-16; % TOF sensitivity of the material [s/mV].
diffMV(i) = tof_diff(i)/perMV; % The output voltage difference with
finalMV(i) = diffMV(i) - 68.394; % (-70mV) and final voltage output.
% Displays the voltage difference and output voltage on command window.
disp(['Voltage difference Y->X = ' num2str(diffMV) ' mV'])
disp(['Calculated Voltage Y->X = ' num2str(finalMV) ' mV'])
end
% Error calculation
finalMV(2) = -68.394; % Real neuron voltage value for reference echo and
realMV = [0 -68.394 39.937 -179.97 -13.01 -126.08]; % all simulations.
error = [finalMV; realMV];
for j=2:6 % Calculates the error as difference between output and ...
    real V.
error(3,j) = (error(1,j)-error(2,j))/error(2,j);
end
% Displays the real action potential (input), output voltage and the ...
    error.
disp('The Output V, Input V and Error Rates Are:')
disp(error)
% Adds the symmetry data points and concatanates all points as [t,V]
interaction_times = [0 9.2944e-6 1.0216e-3 3.0154e-3 3.4672e-4 2.3406e-3
(2e-3-9.2944e-6) (4e-3+9.2944e-6) (2e-3-3.4672e-4) (6e-3-2.3406e-3)];
finalMV = [finalMV finalMV(2) finalMV(2) finalMV(5) finalMV(6)];
totalsol = [interaction_times; finalMV];
totalsol(:,1) = [];
% Implant voltage (action potential of a neuron) plot generation.
syms t; % Adds time as a variable.
VIMP =(110*sin(500*pi*t))-70; % Creates implant voltage function.
fplot(VIMP,[0 0.004],'b','LineWidth',2); % Plots the neuron voltage func.
axis([0 0.004 -200 50]) % Fixes the axes to the expected values.
hold on;
% Computes 9 data point Cubic Spline interpolation.
[xData, yData] = prepareCurveData(totalsol(1,:), totalsol(2,:));
% Sets up fittype and options.
ft = 'splineinterp';
% Fits model to data.
[fitresult, gof] = fit( xData, yData, ft );
```

```
% Plots interpolation fit, with data and the input neuron voltage ...
    function.
h = plot(fitresult);
hold on;
plot(xData,yData,'.','MarkerSize',30)
title(['Action Potential Input vs Interpolated Output Voltage [mV] vs ...
    ' ...
'Time [s] (Cubic Spline Interpolation)'])
% Labels axes
xlabel( 'time (s)', 'Interpreter', 'none' );
ylabel( 'voltage (mV)', 'Interpreter', 'none' );
grid on
legend('Action Potential Input','Interpolated Output','Output Data ...
    Points')
hold off;
```

List of Figures

List of Tables

List of Symbols

Variable	**Description**	**SI unit**
V	voltage	V
f	frequency	Hz
T_0	period	s
ω_0	angular velocity	Hz
t	time	s
$\boldsymbol{p}$	acoustic pressure	Pa
c	speed of sound	m/s
λ	sound diffusivity	m^2/s
z	characteristic acoustic impedance	$Rayl$
λ	wavelength	m
ρ	density	$kg \cdot m^3/s$
M	massive rate of change	$kg/(m^3 \cdot s)$
$\boldsymbol{F}$	volumetric force	N/m^2
$\boldsymbol{E}$	electric field	N/C
$\boldsymbol{D}$	electric displacement	C/m^2
ε_0	permittivity	F/m
$\boldsymbol{P}$	polarization	C/m^2
α_{dm}	mass damping parameter	Hz
β_{dm}	stiffness damping parameter	s
β_{dm}	stiffness damping parameter	s
Q_{dm}	quality factor	$-$
ξ	damping ratio	$-$
θ	phase angle	Rad
λ_{PZT}	piezoelectric material sensitivity	m/V
$\boldsymbol{T}$	mechanical stress	Pa
$\boldsymbol{S}$	strain	$-$

Acknowledgements

I would first want to offer my sincere gratitude towards my advisor *Professor Alberto Corigliano*, for the continuous support and extensive knowledge he provided throughout this thesis. His guidance and enthusiasm extensively help me to improve both the research and my skills as an engineer.

I would also like to acknowledge the immense cooperation I received from *Omer Osman Mohammad Abdalla*. His uninterrupted mentorship aided me exceedingly during the writing of this thesis and over the course of the entire study.

I am also grateful for the vast assistance and encouragement provided by *Dr. Gianluca Massimino*, where his guidance helped me navigate the difficulties I encountered in the course of this work.

Finally, I would like to thank *STMicroelectronics* for providing the custom PMUT device design that is the basis of this research.